R-06-79

Discrete fracture network for the Forsmark site

C Darcel, Itasca Consultants SA

P Davy, O Bour, J-R De Dreuzy
Géosciences Rennes

August 2006

Svensk Kärnbränslehantering AB
Swedish Nuclear Fuel
and Waste Management Co
Box 5864
SE-102 40 Stockholm Sweden
Tel 08-459 84 00
+46 8 459 84 00
Fax 08-661 57 19
+46 8 661 57 19

ISSN 1402-3091
SKB Rapport R-06-79

Discrete fracture network for the Forsmark site

C Darcel, Itasca Consultants SA

P Davy, O Bour, J-R De Dreuzy
Géosciences Rennes

August 2006

Abstract

In this report, we aim at defining a self-consistent method for analyzing the fracture patterns from boreholes, outcrops and lineaments. The objective was both to point out some variations in the fracture network parameters, and to define the global scaling fracture models that can encompass all the constraints brought by the different datasets. Although a full description of the DFN model variability is obviously fundamental for the future, we have put emphasis on the determination of mean parameters.

The main parameters of the disc-shaped DFN model are the fracture size, orientations and spatial density distribution. The scaling model is defined as an extrapolation of existing i) observations at specific scales and ii) local fitting models to the whole range of scales. The range of possible models is restricted to the power-law scaling models formalized in /Davy et al. 1990/, and later further elaborated in /Bour et al. 2002/. During the project we have put emphasize on the definition of the theory and methodology necessary to assess a sound comparison between data taken at different scales, with different techniques.

Both "local" and "global" models have been investigated. Local models are linked exactly to the dataset they represent. Then, the global DFN models arise from the association of local models, different scales and different sample support shapes. Discrepancies between local and global model illustrate the variability associated to the DFN models.

We define two possible Global Scaling Models (GSM). The first one is consistent with the scaling measured in the outcrops (Model A). Its scaling exponent is a_{3d}=3.5 (eq. to k_r=2.5); it overestimates the fracture densities observed in the lineament maps. The second one assumes that both lineaments and outcrops belong to the same distribution model (Model B), which entails a scaling exponent a_{3d}=3.9 (eq. to k_r=2.9).

Both models have been tested by looking for the best consistency in the fracture density-dip relationships, between boreholes data at depth (based on boreholes KFM02A, KFM05A, HFM04 and HFM05) and outcrop DFN models. The main conclusions drawn from the consistency analysis are the following:

- There exists an important subhorizontal fracturing that occurs close to surface, which makes outcrop fracturing different, in term of density, from the fracturing observed in deep geological units from boreholes. The difference between surface and deep units does not exist for fractures dipping more than 30–40°.
- The rock units are remarkably consistent with outcrops for dips larger than 30–40°, and for Model A (a_{3d}=3.5, Figure 7-14). Model B tends to predict larger fracture densities in outcrops than in rock units defined in boreholes (in the dip range of 30–40°).
- There is no equivalence, in the outcrops, of the Deformation Zones, identified at depth.
- The best-fitting model is defined for l_{min} (the smallest fracture diameter consistent with the power law model; $l_{min}=2r_0$ with r_0 the location parameter) smaller than the borehole diameter. With this method, it is not possible to say more about l_{min}. Models that consider larger values of l_{min} do not ensure the consistency between outcrops and boreholes.
- The shear zones, as well as the lineaments, may belong to a different global scaling model than rock units. Further investigations and more data are necessary to characterize this additional GSM.

Along the project, the issue of DFN model and of the fracture definition consistency across scales is often raised. It should be further investigated, together with a more complete description of the model variability.

Contents

1 Introduction

In this report, we aim at defining a DFN scaling model that is consistent with the available dataset of the Forsmark area: several boreholes along which fractures have been recorded, the 5 outcrops where fracture traces have been mapped, and the map of possible deformation zones.

The DFN model is then based on the fracture traces sampled on cores (fracture traces of 0.08 m), outcrops (0.5 m to ~10 m) and lineaments (above 100 m). It aims at filling the gap between observations by assuming that the different scales of the fracture system are linked by a genetic relationship. This is a very strong assumption that cannot be really tested in this project with the available dataset due to the large range of missing scales. For the same reason, we cannot really discuss the generic shape of the scaling relationship since a large number of fitting functions (power law, lognormal function, Weibull functions, …) could match the data.

We thus decided to restrict the range of possible models to the power-law scaling models formalized in /Davy et al. 1990/, and later further elaborated in /Bour et al. 2002/. This is a model that can encompass all the observations from the borehole scale to the lineament scale /see Darcel et al. 2004/. This is also a true "scaling" model in the sense that it only uses scaling relationships that do not contain any characteristic length scale (the power law is the only mathematical function that has this characteristic[1]). The scaling model is thus basically defined by an exponent, which has the same meaning as a physical dimension. The quality of the scaling interpolation (for instance predicting lineament density from core-scale fits) is almost entirely defined by the confidence that one has about this exponent. The ability of the power-law scaling model to apply to fracturing was argued in the review by /Bonnet et al. 2001/. The main assumptions of the model are described in detail in the Sections 3 and 4. All the conclusions derived from this report are dependent on their validity.

This model, as well as any DFN model, raises several issues that are described in the following Section 3, which concerns the mathematical framework of the DFN, the difference between outcrop fractures and lineaments, the range of validity of the scaling model and the issue of l_{min}, and the way to decrease uncertainties and handle variability.

The DFN scaling model is characterised by two scaling exponents a_{3d} and D_{3d}[2], and by a density term α_{3d}, which depends on fracture dip and strike. In the present case, where the fractal nature of the fracture system is weak (D_{3d} close to 3, Sections 6.2.4 and 6.4.3), the power-law exponent a_{3d} mainly contains the scaling information. It is critical because fracture densities extrapolated from one scale to the other are highly sensitive to it. The density term $\alpha_{3d}(\theta, \varphi)$ is the fracture density for a fracture diameter l of 1 (Equation 4-1). It is fundamentally related to the scaling exponent a_{3d} (see its unit dimension for instance), so that it is meaningless to compare two different values of α_{3d} if they have been calculated for two different scaling exponents. On the other hand, $\alpha_{3d}(\theta, \varphi)$ is the only information that can be used for really comparing the consistency of a DFN model with data taken on different places, at different scales. In a sense the fracture network orientation density is used as the "DNA" of a DFN model, and the consistency analysis consists in comparing the DNA of the different datasets.

We cannot be sure that the best-fitting model deduced from this analysis is unique since it is almost impossible to explore the range of all possible models, because of the large natural variability, and because of the critical undersampling of the geological formations with respect to the observed variability of geological formations and deformations. However we think that the conclusions derived from this analysis are very informative on the fracture patterns, and that the model concept retained here, together with the corresponding parameters determination, can be used as a reasonable conceptualization of the DFN at the Forsmark site.

---

[1] See also Appendix 2.

[2] A recap of the model parameters and mathematical concepts is provided in Section 4.

2 Index of notations

α	Density term that fixes the density at a given scale of observation.
(θ, φ)	Trend and plunge of a fracture pole.
2D	Two dimensional (fracture appear as traces *'t'*).
2d	Subscript notation for 2D.
3D	Three dimensional (disc-shape fractures of radius '*r*' or diameter '*l*').
3d	Subscript notation for 3D.
a	Exponent of the power-law size distribution also called "length exponent", ($k_t = a_{2d} - 1$; $k_r = a_{3d} - 1$).
b_{min}, b_{max}	Boundary distances.
C_{shape}	Coefficient related to the fracture shape, equal to $\pi/4$ if fractures are assumed to be discs.
d	Euclidean dimension (1 for a line, 2 for a plane, 3 for a cubic volume).
D_{1d}, D_{2d}, D_{3d}	Same as D_c, subscript refers to a dimension precisely measured over a one-dimensional, two-dimensional or three-dimensional support.
D_c	Fractal dimension (correlation dimension) associated to a DFN.
DFN	Discrete fracture network.
DZ	Deformation Zone.
GSM	Global Scaling Model.
k	Shape parameter associated to the probability density function of a power-law distribution.
k_r	Shape parameter associated to the probability density function of a power-law distribution of fracture radi.
k_t	Shape parameter associated to the probability density function of a power-law distribution of fracture traces.
L	Typical size of a system (ex: side L of a cube).
l	Fracture diameter for a disc-shaped fracture (l=2*r).
l_c	Arbitrary cutoff diameter in a DFN model ($l_c \geq l_{min}$).
l_{min}	Minimum fracture diameter consistent with the DFN model.
P_{32}	Fracture area by unit of volume.
P_{21}	Fracture length by unit of area.
P_{10}	Number of fracture intersections by unit of length.
r	Radius of a disc-shape fracture.

r_0	Location parameter associated to the probability density function of a power-law distribution. It represents the minimum radius consistent with the DFN model.
r_c	Arbitrary cutoff radius in a DFN model ($r_c \geq r_0$).
s	Distance.
RD	Rock Domain.
RU	Rock Unit.
t	Fracture trace length.

3 Scientific framework

The scaling model is defined as the extrapolation of i) existing observations at specific scales and ii) local fitting models to the whole range of scales and parameters. It aims at filling the gap between these observations by assuming that the different scales of the fracture system are linked by a genetic relationship. This is a very strong assumption that cannot be really tested in this project with the available dataset due to the large range of missing scales. For the same reason, we cannot really discuss the generic shape of the scaling relationship since a large number of fitting functions (power law, lognormal function, Weibull functions, …) could match the data.

We thus restrict the range of possible models to the power-law scaling models formalized in /Davy et al. 1990/, and later further elaborated in /Bour et al. 2002/. This is a model that can encompass all the observations from the borehole scale to the lineament scale /see Darcel et al. 2004/. This is also a true "scaling" model in the sense that it only uses scaling relationships that do not contain any characteristic length scale (the power law is the only mathematical function that has this characteristic[3]). Its applicability to fracturing was argued in the review by /Bonnet et al. 2001/.

This model, as well as any DFN model, raises several issues – some of them are linked – that we try not to escape, if possible, in the analysis:

1. We think that a basic definition of what a DFN model is has yet to be assessed properly. The DFN model is obviously an incomplete mathematical representation of the reality. It is a makeshift model between several issues: the underlying physics and geology, the purposes for which it is to be used, the way it will be used, the mathematics, the availability of data, … These concerns should be raised to define the basic constituents of the DFN model that are: the object on which the model applies (fractures, fracture clusters, lineaments, …), the mathematical framework (1st-order DFN model, 2nd-order statistics, etc), and the range of validity. This discussion is fundamental but beyond the purpose of this report. We recommend that it could be developed in a further work with the experience collected in the different sites.
2. The definition of the fracture "object" belongs to the previous discussion. Lineaments and outcrop fractures are clearly two different objects in the sense that a lineament is a cluster of several individual fractures whose length is smaller than the lineament scale. Whether or not these objects share the same scaling logic is a key issue, and a strong assumption that cannot be checked with the available dataset[4]. The problem is that we need this assumption to define the DFN model, but we don't know if the so-defined scaling model is still valid when comparing boreholes and outcrops. On the other hand, we are quite confident that boreholes and outcrops map the same objects. We thus put a strong emphasis on the comparison between borehole and outcrop data, and we discuss if the lineaments could belong to the same statistical framework.
3. The range of validity of a scaling model is obviously a key issue for modelling flow or mechanical properties. As for the difference between lineaments and fracture outcrops discussed above, we raise the issue of knowing the lower limit of the scaling law, that is the smallest fracture that belongs to the scaling DFN model. The difficulty is that we are not looking for the smallest fracture, but for the smallest fracture *consistent with* the DFN model.

[3] See also Appendix 2.

[4] To tackle this issue a higher resolution lineament map or larger size trace maps would be required.

4. The DFN model has an “average” definition, in the sense that it smoothes out the natural variability. The DFN model does not reproduce nature, but predicts some average density values of fracture networks. This means that the DFN model owns an intrinsic uncertainty related to the natural variability. Conversely, natural variability is not the only source of uncertainty. The goal of the DFN modeller is to reduce the uncertainty by looking for some geological controls of the DFN models. The method consists in incorporating information on the relationship between fracturing style, fracturing intensity and geology, lithology, etc. If the methodology is potentially praiseworthy, we would like to stress two potential concerns:
   – Implicitly this comes to postulate that there exists a kind of DFN-model homogeneity in geological formations, which is trivial in some situations but worth being assessed in others.
   – The DFN uncertainty results from both some intrinsic variability and statistical effects. Since increasing the number of DFN models comes to decrease the number of constraints, there is a balance to find between the decrease of variability and the increase of statistical uncertainty.

4 DFN model framework

4.1 Fracture parameters

A fracture is defined by its size, orientation and position. In the absence of information about fracture shape, a disk shape is assumed. Note that any polygonal or elliptic shape would give similar results, as long as the anisotropy in the fracture-plane shape remains small. The fracture parameters are constrained by the DFN model described below.

Length and orientation are assumed to be independent parameters, meaning that small and large fractures should have similar orientation distributions. Testing this assumption requires a large number of data. The simplest method would consist in dividing the orientations into several classes, and in analysing the length distribution for each class. However the small number of points within each class, as well as the natural variability, make the calculation of a scaling length exponent per class questionable. We thus make the following analysis in the framework of this assumption. We will discuss some elements of consistency when comparing boreholes and outcrops. However we recommend to consider the independence assumption as a potential source of uncertainty when using the DFN model.

4.2 DFN model formalism

The DFN model provides the number of fractures in any given volume with given lengths and orientations.

4.2.1 Parent DFN model

The 3D fracture distribution model([5]) is quantitatively given by a general mathematical expression of the type:

$N_{3d}(L, l, \theta, \varphi, ...)\, dl\, d\theta\, d\varphi\, d\ldots,$

which is the number of fractures contained in a volume of typical size([6]) L, with lengths between l and $l+dl$, orientations in $[\theta, \theta+d\theta]$ and $[\varphi, \varphi+d\varphi]$, and a series of other properties that are represented by "…". In addition to length (**diameter** of a disc-shape fracture) and angular characteristics, the expression can include some fracture shape parameters (as eccentricity), which are relevant to the intersection issue.

Using an appropriate expression for N_{3d} is obviously the key point of this study. In particular the fracture distribution model N_{3d} must contain the scaling relations that enable extrapolation of intensity from one scale to another. The simplest model contains two of such scaling laws: the fractal density (i.e. the fractal dimension D_{3d}), and the power-law length distribution (exponent a_{3d}). This has been demonstrated by number of studies (see e.g. review by /Bonnet et al. 2001/), formalized in /Davy et al. 1990/, and later further elaborated in /Bour et al. 2002/. Using these scaling assumptions, and assuming that length, density and orientations are reasonably independent entities, N_{3d} takes the following form:

$$N_{3d}(L, l, \theta, \varphi) = \alpha_{3d}(\theta, \varphi)\, l^{-a_{3d}} L^{D_{3d}} \qquad \text{Equation 4-1}$$

---

[5] 3D refers to three dimensional space.

[6] The typical size L is given, for a volume V (in 3D) by $L=V^{1/3}$ and for a plane area A (in 2D) by $L=A^{1/2}$. For isotropic volumes (cubes, spheres) the notion of "typical size" is straight. It becomes less intuitive when the volume has an anisotropic shape.

The power-law model is defined down to a limit fracture length (minimum diameter noted l_{min}).

In the following we provide a few mathematical developments and notations that will be useful all through the report.

First we aim at removing the system-size effects in order to compare observations made on systems of various sizes. We thus define the density distribution model, which is (see Figure 4-1):

$$n_{3d}(l,\theta,\varphi) = \frac{N_{3d}(L,l,\theta,\varphi)}{L^{D_{3d}}} \qquad \text{Equation 4-2}$$

Note that the previous definition requires to know (or measure) the dimension D_{3d}, which can be either the Euclidean dimension (3 for 3D systems) if the density is homogeneously distributed, or less than 3 if the pattern of fracture centres is fractal. We note that the dimension D_{3d} fixes the fracture density scaling; it is therefore a mass dimension. Details on the fractal dimension definition and subsequent fractal dimension measurements are provided in Appendix 3. In brief, the mass dimension is equivalent to the dimension of order two in a multifractal spectrum and to the so-called correlation dimension.

It is also convenient to define the density distribution of fractures with respect to a parameter subset: length, dip and/or strike, which is the integral of $n_{3d}(l,\theta,\varphi)$ with respect to the parameter(s) that is (are) not considered. To simplify the notations, we keep the same variable name as in Equation 4-3, but we specify explicitly the number of parameters of the density function. For instance, the density distribution of fracture lengths (whatever dip and strike) now becomes:

$$n_{3d}(l) = \int_{\theta}\int_{\varphi} n_{3d}(l,\theta,\varphi)\, d\theta\, d\varphi \qquad \text{Equation 4-3}$$

The density distribution of fracture orientations is:

$$n_{3d}(\theta,\varphi) = \int_{l} n_{3d}(l,\theta,\varphi)\, dl \text{ ; etc} \qquad \text{Equation 4-4}$$

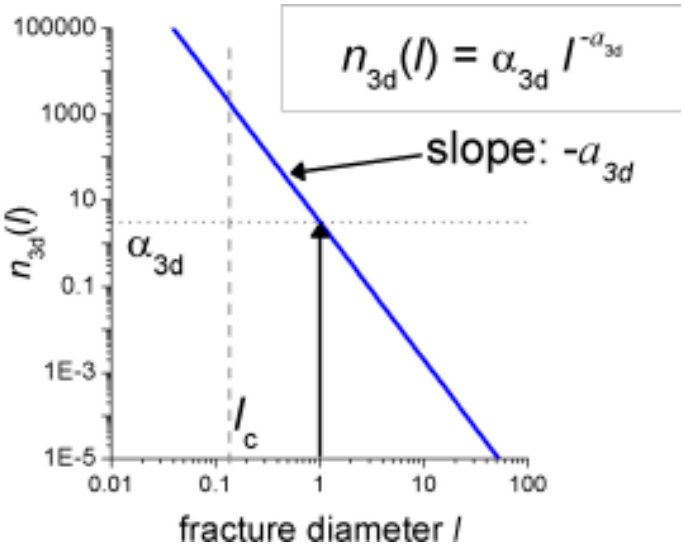

Figure 4-1. *Density distribution of fracture diameters, illustration on a log-log diagram. l_c symbolizes an arbitrary cutoff diameter of the density distribution. (The same shape is found in 2D with $n_{2d}(t)$, a_{2d} and α_{2d} instead of $n_{3d}(l)$, a_{3d} and α_{3d}).*

Finally, density distribution model can be written either for the fracture diameters (noted *l*) or for the fracture radius (noted *r*). Given Equation 4-1, the corresponding fracture density distribution written for the fracture radii (*r*) is:

$$N_{3d}(L,r,\theta,\varphi) = \left[\alpha_{3d}(\theta,\varphi)\cdot 2^{-a_{3d}+1}\right] r^{-a_{3d}} L^{D_{3d}} \qquad \text{Equation 4-5}$$

4.2.2 Notations requirements

In the SKB nomenclature, the power-law probability density function is formulated as /Munier 2004/:

$$f(r) = \frac{k\, r_0^k}{r^{k+1}} \quad \begin{matrix} k>0 \\ r_0>0 \\ r_0 \le r < \infty \end{matrix} \qquad \text{Equation 4-6}$$

where *r* refers to the fracture radius, r_0 is the location parameter (smallest value of *r*), and *k* is the shape parameter. In addition, the fracture density is expressed from the amount of fracture surface by unit of volume, P_{32} (m^{-1}). Hence, the different notations are related as:

$$k = a - 1 \qquad \text{Equation 4-7}$$

$$r_0 = \frac{l_{\min}}{2} \qquad \text{Equation 4-8}$$

As was underlined in Section 3 (Scientific framework), the value of r_0 (or eq. l_{min}, which represents the smallest fracture *consistent with* the DFN model) remains often unknown. Besides, the density expressed through P_{32} is strongly related to the minimum class of fracture radius taken into account. From the DFN model expressed in Equation 4-1, P_{32} is simply given by:

$$P_{32}(l_c) = C_{shape}\frac{\int_{l_c}^{L}\alpha_{3d}\cdot l^{-a_{3d}+2}\cdot L^{D_c}\cdot dl}{L^3}$$

where C_{shape} is a function of the fracture shape (equal to π/4 for disks) and l_c is the cutoff length representing the smallest fractures included in the calculation of P_{32}. It comes that the three parameters, l_c , P_{32} and α_{3d} are related.

Integration of the former equation leads, for $a_{3d} \neq 3$, to

$$P_{32}(l_c) = C_{shape}\alpha_{3d}\cdot L^{D_c-3}\cdot\frac{\left[l_c^{-a_{3d}+3} - L^{-a_{3d}+3}\right]}{(a_{3d}-3)} \qquad \text{Equation 4-9}$$

For a fracture system dominated by the smallest fractures ($a_{3d} \geq 3$), the dominant term is a function of l_c:

$$P_{32}(l_c) \cong C_{shape}\alpha_{3d}\cdot L^{D_c-3}\cdot\frac{\left[l_c^{-a_{3d}+3}\right]}{(a_{3d}-3)}$$

In summary, for disc-shaped fractures, if the cutoff length scale is expressed in term of diameter *l* then:

$$P_{32}(l_c) \cong \frac{\pi}{4}\cdot\alpha_{3d}\cdot L^{D_c-3}\cdot\frac{\left[l_c^{-a_{3d}+3}\right]}{(a_{3d}-3)} \qquad \text{Equation 4-10}$$

with α_{3d} defining the density term of the fracture diameter distribution. If the fracture cutoff length is expressed in term of radius r_c then we have:

$$P_{32}(r_c) \cong \pi \cdot \left[\alpha_{3d} \cdot 2^{-a_{3d}+1}\right] \cdot L^{D_c-3} \cdot \frac{\left[r_c^{-a_{3d}+3}\right]}{(a_{3d}-3)} \qquad \text{Equation 4-11}$$

When expressing DFN parameter sets, the quantity P_{32} must be accompanied with a cutoff length (radius r_c or diameter l_c). The cutoff length can be chosen by the user or dictated by resolution effects, it is not necessarily equal to the location parameter.

4.2.3 DFN derivation on planar and borehole samples

The fracture trace density distribution resulting from the intersection of the DFN with a planar sample is written as:

$N_{2d}(L, t, \theta, \varphi) = \alpha_{2d}(\theta, \varphi) t^{-a_{2d}} L^{D_{2d}}$

The relation between $\alpha_{3d}(\theta, \varphi)$ and $\alpha_{2d}(\theta, \varphi)$ is developed in Appendix 4. The relation between a_{2d} and a_{3d} is such that: $a_{2d} = a_{3d} - 1$ /Piggott 1997/. As long as a_{3d} is larger than 2, the relation between D_{2d} and D_{3d} is such that: $D_{2d} \cong D_{3d} - 1$ /Darcel et al. 2003/. The fracture trace distribution follows the abovementioned power-law model down to a minimum trace length equal to the minimum fracture diameter of the 3D parent distribution.

The fracture density distribution resulting from the intersection of the DFN with a borehole is still modelled by a power-law with:

$N_{1d}(L, l, \theta, \varphi) = \alpha_{1d}(\theta, \varphi) l^{-a_{1d}} L^{D_{1d}}$

with $a_{1d} = a_{3d} - 2$ and $D_{1d} \cong D_{3d} - 2$

The relation between fracture density terms $\alpha_{3d}(\theta, \varphi)$ and $\alpha_{1d}(\theta, \varphi)$ are thoroughly investigated throughout the report (Section 7, Appendix 4, /Davy et al. sub/).

4.2.4 Fractal terms

The fractal dimension included in the present DFN model defines the fracture density scaling; it is a mass dimension. The mass dimension is equivalent to the so-called correlation dimension (Appendix 3, see also section Fractal dimension in /Bour et al. 2002/). All the dimensions introduced above and noted D_{3d}, D_{2d} and D_{1d} refer to mass or correlation dimensions associated to the fracture density respectively in 3D, 2D and 1d.

The fractal dimension (D_c) quantifies the rate of *fractal clustering* or *fractal correlation* related to the spatial fracture density distribution of the DFN model. As illustrated in the figure below (Figure 4-2), the smaller the D_c, the higher the fractal clustering. Strictly speaking, the set of points displayed in Figure 4-2 (left) is not fractal: in that case the fracture density distribution is homogeneous[7], with $D_c=d$ (d the Euclidean dimension, 2 for a plane). However, the homogeneous case ($D_c=d$) is the upper limit of the fractal mathematical model and therefore belongs to the fractal mathematical framework described here. In other words, the homogeneous case is encompassed in the potentially fractal DFN model. Similarly in 3D we have, $D_c \leq 3$. If $D_c < 3$, then the DFN model is said fractal in strict sense. If $D_c = 3$ the fracture density distribution is said homogeneous however D_c remains the parameter "fractal dimension". Note that, by definition, the fractal dimension of a set of points distributed over an object (for instance a plane, as in the figure below) is expected to be bounded by the topological/euclidean dimension of the object (for instance $D_c \leq 2$ in a plane).

[7] The "homogeneous" distribution results from a poissonian process.

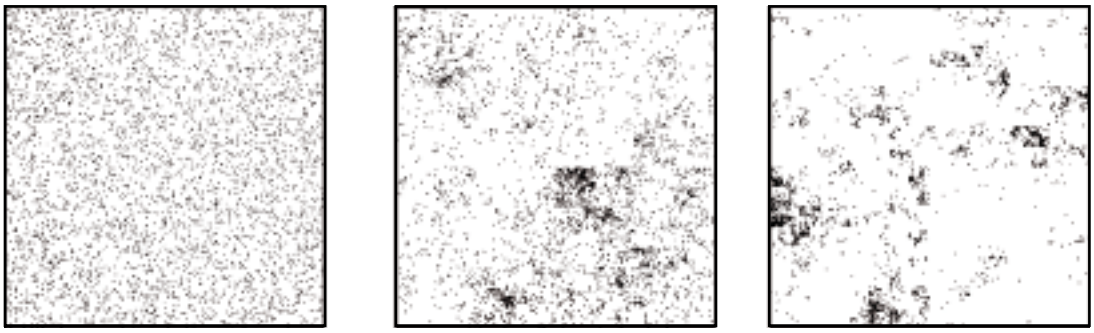

Figure 4-2. *3 sets of points generated in 2D, on a plane. From left to right Dc decreases from 2 (homogeneous case) down to 1.4.*

The term "fractal" is related to how the space is filled; the sole power-law nature of the length distribution is not sufficient to define a fractal object. One can not measure a fractal dimension less than the Euclidean dimension (strict sense of fractal) if the distribution associated to the fracture position is poissonian, this whatever the length distribution characteristics. The length distribution does not describe how the space is filled, it only provides the number of fractures of a given size. Then, whatever a, if $D_c<d$, the DFN is fractal and whatever a, if $D_c=d$, the DFN is homogeneous but can still be described within the fractal mathematical framework.

An object is said "self-similar" if it looks the same whatever the scale of observation /Mandelbrot 1982/. Applied to DFN modelling, this happens if the relation $a=D_c+1$ is satisfied. (Note that a and D_c are assumed to be independent; a cannot be used to derive D_c nor the inverse). Then whatever the scale of observation (within the range of validity of the model) the system looks the same: in a system of size L, the number of fractures whose size is equal to xL is independent of L:

$$N(xL) = \int_{xL}^{L} \alpha \cdot l^{-a} \cdot L^{D_c} \cdot dl = \frac{\alpha}{a-1}(xL)^{D_c-a+1=0} = \text{constant}$$

Note that if $a < D_c+1$ then $N(xL)$ increases with L: in that case the apparent number of larger fractures increases when the system size of observation increases, whereas on the contrary if $a > D_c+1$ then the number of larger fractures decreases when increasing the system size.

5 Forsmark site and database

The Forsmark site is one of the two candidate areas for the deep repository of nuclear waste to be built by SKB. It is located in the northern Uppland within the municipality of Östhammar, about 170 km north of Stockholm. In this section we review quickly the site configuration together with spatial localization of the available datasets. A complete site description of the Forsmark area, model version 1.2, is reported in /R-05-18/.

Three model areas define the site: in complement to the **candidate area**, within which the repository is expected to be placed, the site descriptive modelling is performed on two different embedded scale model volumes, the **regional** and the **local** model volumes (Figure 5-1). The local model encompasses the candidate area plus accesses and immediate environs, it is area is close to 30 km^2. The regional model volume is much larger (11×15 km), in order to place the local model in a larger context, mainly to allow sensitivity analysis of hydrogeological boundary conditions. The vertical extent of the model is set to 1,200 m (+100 to –1,100 m).

For the purpose of the present analysis we use the following surface and in depth dataset to build the DFN model:

- outcrops, area hundreds of sq meters, traces meter to tens of meters,
- Lineament maps hundreds of sq km, traces tens of meters to 10 km, and
- boreholes km length, traces from borehole diameter and up.

The datasets from SICADA and SDE (references in Table 5-1 to Table 5-4) are briefly presented below; their spatial position within the Forsmark site is recalled (on Figure 5-2 for the lineaments, Figure 5-3 for the outcrops and Figure 5-4 for the boreholes).

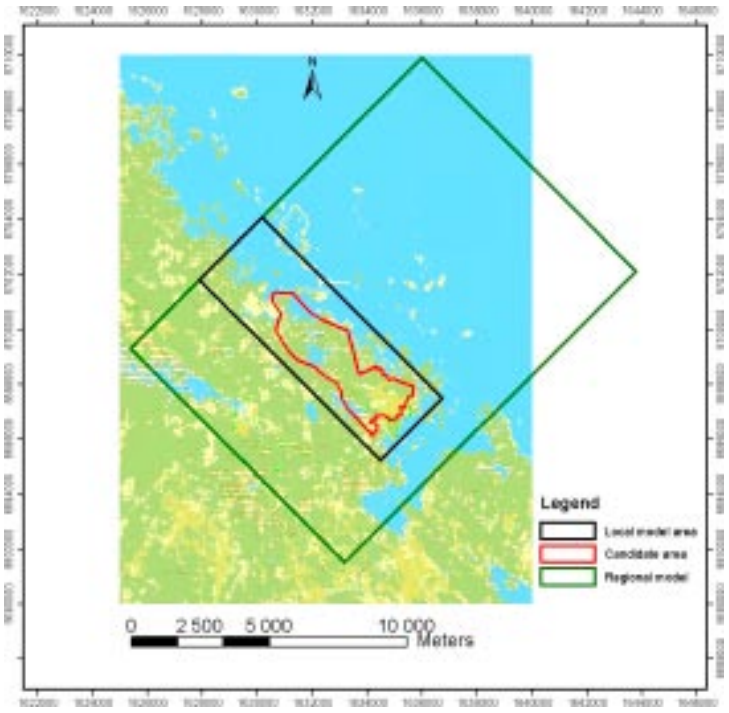

Figure 5-1. *Model volumes at the Forsmark site, with the regional model area contour, 11 by 15 km, the local model area contour and the candidate area model contour. The sea and land use are drawn in background.*

The lineament map available covers the regional model area (Figure 5-2, reference in Table 5-2). Lineaments are linked. The final dataset contains slightly above a thousand elements (linked lineament traces), classified in 3 categories: local minor, local major and regional (drawn in different colours in Figure 5-2, see legend). The maximum trace length recorded is equal to 11,445 m, with a lineament that cross cuts the entire model area in the NW direction; the minimum trace length is equal to 15 m, which is one order of magnitude below the resolution scale of the lineament map estimated at 200–300 m from the length distribution. We note that the lineament map interpretation is based on geophysical data "acquisition" campaigns that have been carried out at different times and using methods with different resolution limits. A detailed description can be found in /R-05-18/ (Section 5.2.3 and Figure 5-16).

Five outcrop trace maps are available (Table 5-1), all located in the local model area (Figure 5-3, see Appendix 1). Each of them contains about a thousand identified fracture traces for areas comprised between about 279 m^2 (AFM0010098) and 645 m^2 (AFM000053). The truncation policy for the trace mapping is 0.5 m. The largest traces on the map are limited by the map size. In addition to these fracture trace maps, each outcrop has been sampled down to a resolution scale of 0.2 meters along scanlines (Table 5-1).

The 2D superficial database is completed by a large number of depth data sampled along boreholes (Figure 5-4). Drilled boreholes (KFM-A) are about a thousand meter length whereas the other are limited to a few hundred meters (cored borehole named KFM-B and percussion boreholes named HFM-). Boreholes plunge vary from close to vertical (90°) to 60°. Note that, due to time constraints, analyses of the borehole database is limited to a few selected boreholes (mainly A-cored boreholes, especially KFM02A and KFM05A),

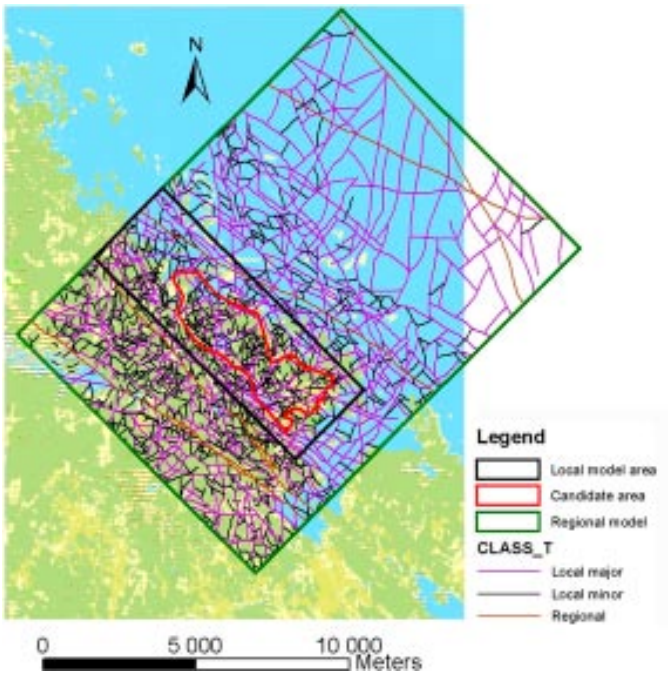

Figure 5-2. *Lineament traces within the regional model contour (thick green rectangle), 11 by 15 km.*

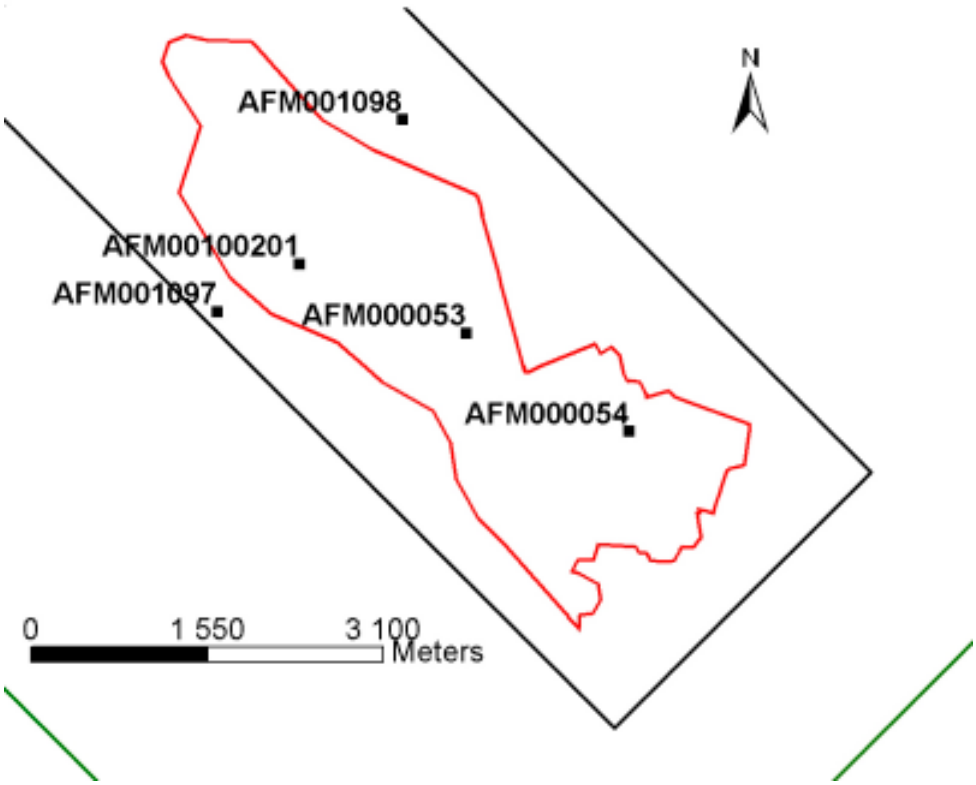

Figure 5-3. *Location of the 5 five outcrops within the local model area and the candidate area.*

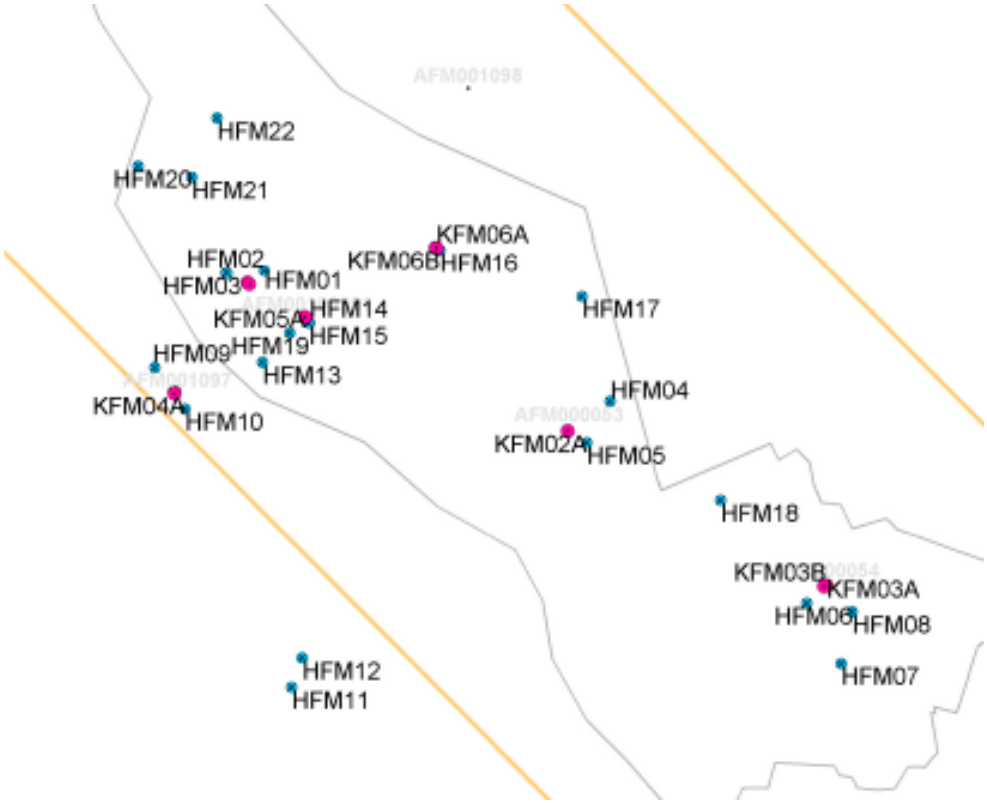

Figure 5-4. *Borehole locations within the candidate (grey line) and local model (orange line) areas. Cored (KFM…) and percussion (HFM…) boreholes and are represented respectively by pink and blue symbols.*

The different datasets are listed in the following tables:

Table 5-1. Datasets: outcrops.

Name	Link to datafile
AFM000053	SDEADM_GOL_FM_GEO_1765
AFM000054	SDEADM_GOL_FM_GEO_1344
AFM001097	SDEADM_GOL_FM_GEO_1866
AFM100201	SDEADM_GOL_FM_GEO_1911
AFM001098	SDEADM_GOL_FM_GEO_1869

Table 5-2. Datasets: lineaments.

Name	Link to datafile
Lineaments	SDEADM_GV_FM_GEO_2079 (new name: SDEAM_GV_FM_GEO_2494)

Table 5-3. Datasets: boreholes.

Name	Link to datafile
KFM01A	P_fract_core (updated early October 2005)
KFM02A	p_freq_1m_1hint (non official at the time of analysis)
KFM03A	p_one_hole_interpret
KFM04A	
KFM05A	
KFM06A	
HFM1 to HFM22	

Table 5-4. Datasets: scanlines.

Name	Description	Link to datafile
LFM000007	on AFM000053	scanlines.dbf
LFM000008	on AFM000054	
LFM000009	on AFM000053	
LFM000010	on AFM000054	
LFM000576	on AFM001097	
LFM000577	on AFM001097	
LFM000578	on AFM001098	
LFM000579	on AFM001098	
LFM000655	on AFM100201	
LFM000656	on AFM100201	

6 Local analyses

6.1 Introduction

Here data coming from different supports are analysed separately. By doing this, one comes to define "local models"[8] of DFN, i.e. linked exactly to the dataset they represent. We note that depending on the dataset, a complete (including geometrical information about fracture size, orientation and position) DFN model can or can not be build since some datasets (taken alone) do not contain the necessary information. Then, defining a global DFN model requires associating different scales and different sample support shapes, which is the purpose of Chapter "Scaling Model".

The only inter-comparison performed in this chapter concerns the different outcrop trace maps, since they share the same shape (2d planar shape) and the same resolution scale. The fracture trace maps data are therefore analysed together (a simple representation trace map by trace map).

6.2 Outcrop fracture trace maps

6.2.1 Preamble

The outcrop fracture trace maps contain the identified fracture traces, including a large amount of information such as the fracture trace length, strike, dip and position. The outcrop local lithological properties are associated to the fracture traces. Also, each outcrop belongs to a Rock Domain. The sampling and interpretation process displays the following particularities:

- Contrary to the lineament map, the fracture traces on outcrops are not linked.
- Contrary to the borehole data, the separation between Rock Units (RU) and Deformation Zones (DZ) is not performed. Despite, outcrop AFM001097 is located on one of the large shear zones that cut through the investigated area.

The particular position of AFM001097 is an opportunity to highlight whether or not the fracture traces within or outside a deformation zone have a distinct signature.

6.2.2 Fracture trace maps

Three of the maps (AFM000053, AFM000054 and AFM100201) belong to Rock Domain 29 (code 101057) associated with a dominant of type granite to granodiorite, metamorphic, medium-grained (Chapter 10). AFM001098 belongs to Rock Domain 32 characterized by a domination of granite metamorphic (code 101058). AFM001097 belongs to Rock Domain 18 characterized by a domination of granodiorite metamorphic (code 101056). Locally the outcrop lithology is refined (Figure 6-1) and presents local variations from the Rock Domain dominant rock type.

6.2.3 Orientations

All the five fracture trace maps display preferential directions of trace orientations. A complete representation of orientation distributions, including both strikes and dips, is provided through stereoplots (Schmidt projections) in the next figures (corresponding discrete stereoplots are given in Appendix 1). At that stage the distributions are not yet corrected from orientation bias.

[8] Local model differs from a model for the site local area, local is used as "linked to the local dataset".

a) AFM000053

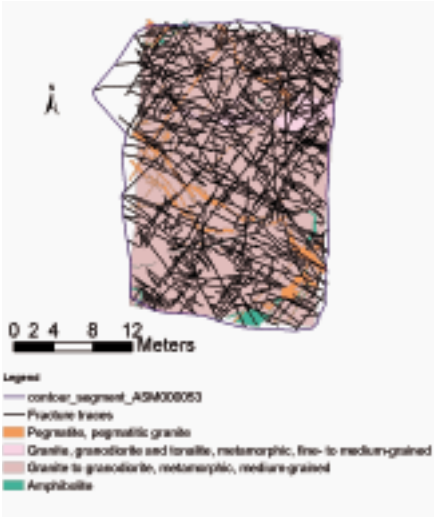

b) AFM000054

c) AFM001097

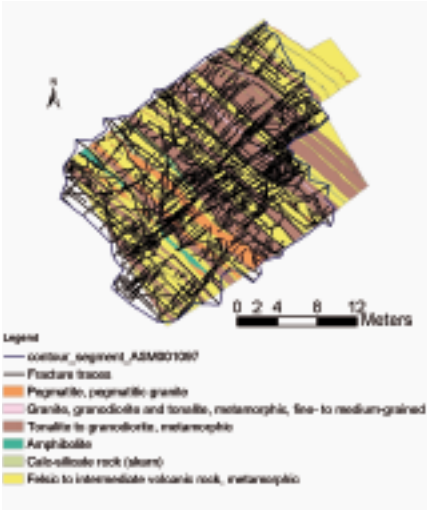

d) AFM001098

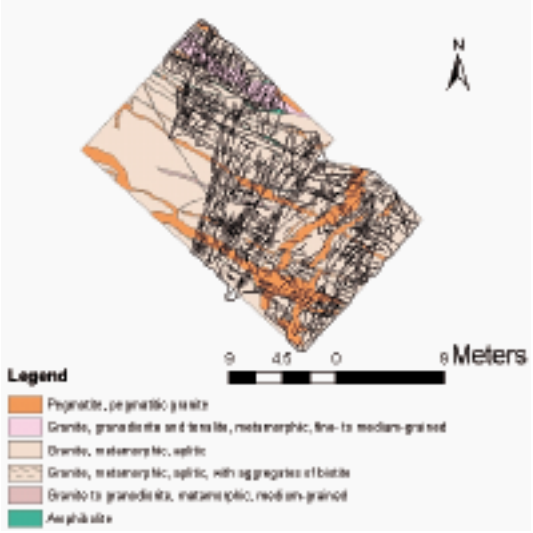

e) AFM100201

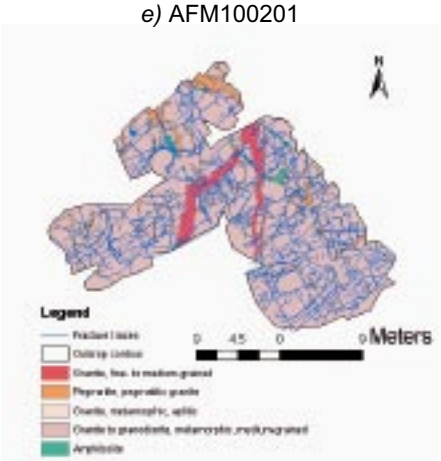

Figure 6-1. *Fracture trace maps superposed to the geological maps.*

However, intercomparison between the five datasets is allowed since all the fracture trace maps are horizontal. All the five datasets display apparent peaks of fracture intensity corresponding to close to vertical fractures.

In the perspective of the local DFN model definitions, pole sets are identified and modelled through Fisher distributions, for each outcrop dataset (To lighten the presentation, results of this analysis are provided in Appendix 1). The interpretation performed does not assume a link to the site geological history: only the pole distributions over the stereonets have been considered (Figure 6-2), in order to simply reproduce the statistical orientation distribution extracted from the outcrop trace maps. The DFN user can take the parameters provided in the associated tables (Appendix 1) to reproduce the local orientation distribution associated to each outcrop.

From the stereoplots one observes that two main peaks of fracture intensity, oriented NE and NW, appear on each sample, with little variations from one map to another.

a) AFM000053 *b)* AFM000054

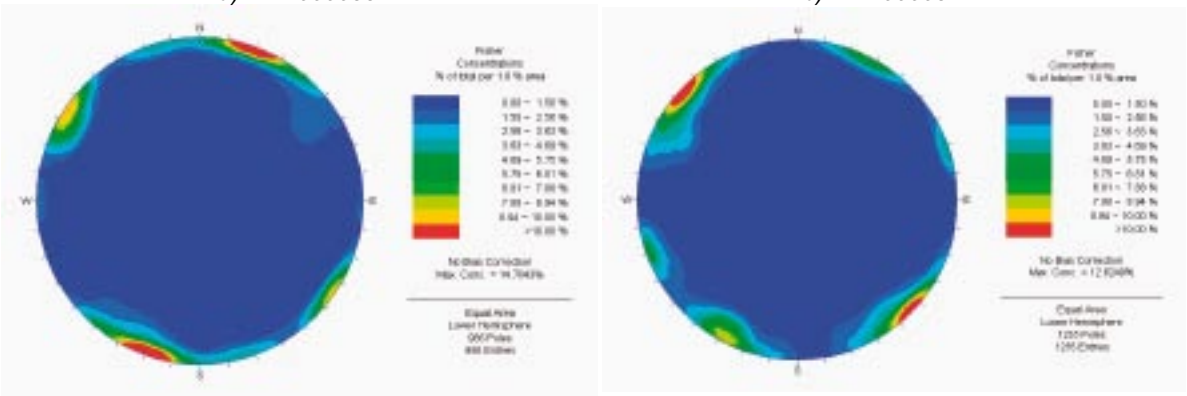

c) AFM001097 *d)* AFM001098

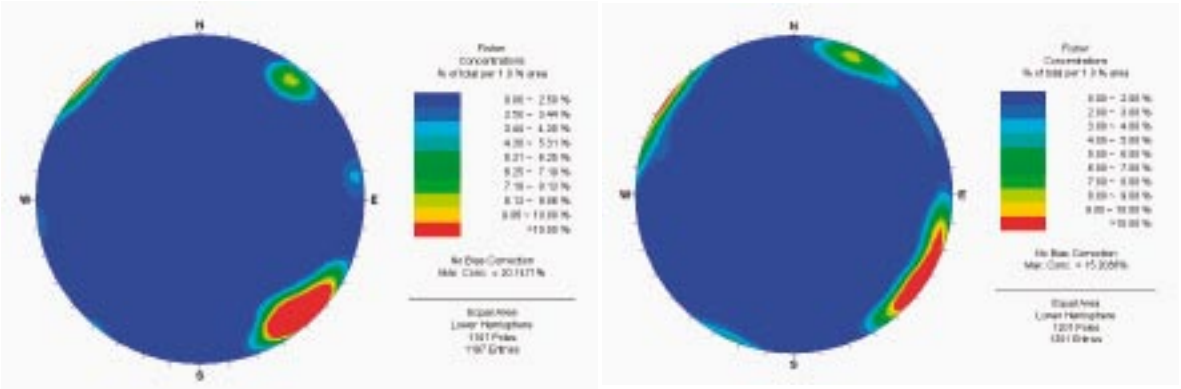

e) AFM100201

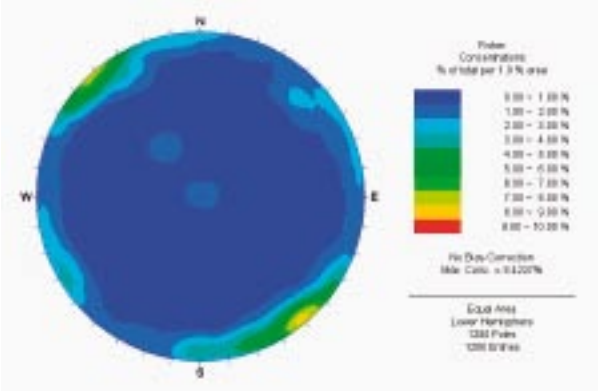

Figure 6-2. *Stereoplots (Schmidt projections, no bias correction) from fracture traces.*

The fracture orientation distribution observation is completed by the representation of two cross-sections in the strike-dip space: fracture intensity evolution with the dip and fracture intensity evolution with strike (Figure 6-3). Also, the evolution with fracture dip allows counting the proportion of fractures between subhorizontal and vertical, which is a critical parameter when comparing boreholes to outcrops data.

The relative proportion of horizontal versus vertical fractures is very similar from one outcrop to the other (Figure 6-3 left). Also the two main fracture strike directions appear on each dataset when comparing the evolution of fracture density versus fracture strike. To sum up, the five outcrops display very similar characteristics (at that stage bias correction is not yet performed): a domination of the close to vertical fractures, with mainly two trends, NE and a NW and a similar variations with dip (Figure 6-3 left). In the following (see Section 6.2.8), a single mean orientation model representing all the fracture trace maps will be defined.

6.2.4 Fractal clustering

Fractal dimensions (Section 4.2.4 and Appendix 3) associated to the fracture trace maps are derived from the application of the two points correlation function (also called integral of correlation). The method was applied previously and reported in /Darcel et al. 2004/. Details of the methodology are recalled in Appendix 3. In brief, the integral of correlation is calculated twice: once from the real fracture center dataset, leading to $C(s)$; and once from a simulated fracture center dataset (leading to $C_{homogeneous}(s)$), where the fracture centers are randomly redistributed through the sample shape, according to a poissonian process. Accordingly, for the 2D case, the quantity $C_{homogeneous}(s)/C(s)$ varies like $s^{2-D_{2d}}$, where s is a distance, 2 is the Euclidean dimension of the plane and D_{2d} the fractal dimension. D_{2d} is simply deduced from the slope ($2-D_{2d}$) of the quantity $C_{homogeneous}(s)/C(s)$ represented in a log-log diagram (Figure 6-4). Analysing $C_{homogeneous}(s)/C(s)$ instead of only $C(s)$ allows to decrease possible artefacts linked to sample shapes.In practice, the slope ($2-D_{2d}$) is measured over a finite range, comprised between a minimum and a maximum boundary distances, b_{min} and b_{max} (dotted red lines in Figure 6-4). In addition a qualitative degree of confidence is attributed to each measurement (from 3: good confidence to 1: poor confidence). It is based on the quality of the fit (departure from the theoretical straight line in the log-log representation), from which D_{2d} is deduced. A confidence level equal to 1 indicates that D_{2d} is an average scaling fit that does not render local variations; a confidence level of 3 reflects a very good power-law fit over a scale range of at least one order of magnitude.

The method is applied for the five outcrops (Figure 6-4 for outcrop AFM000053 and AFM100201). Results are summarised in Table 6-1 below and Figure 6-5.

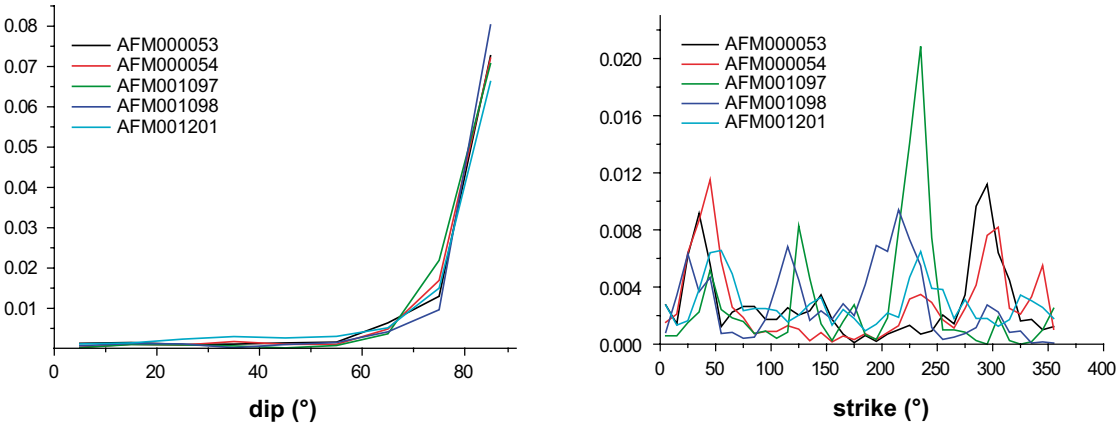

Figure 6-3. *Evolution of apparent fracture intensity versus (left) fracture dip and (right) fracture strike.*

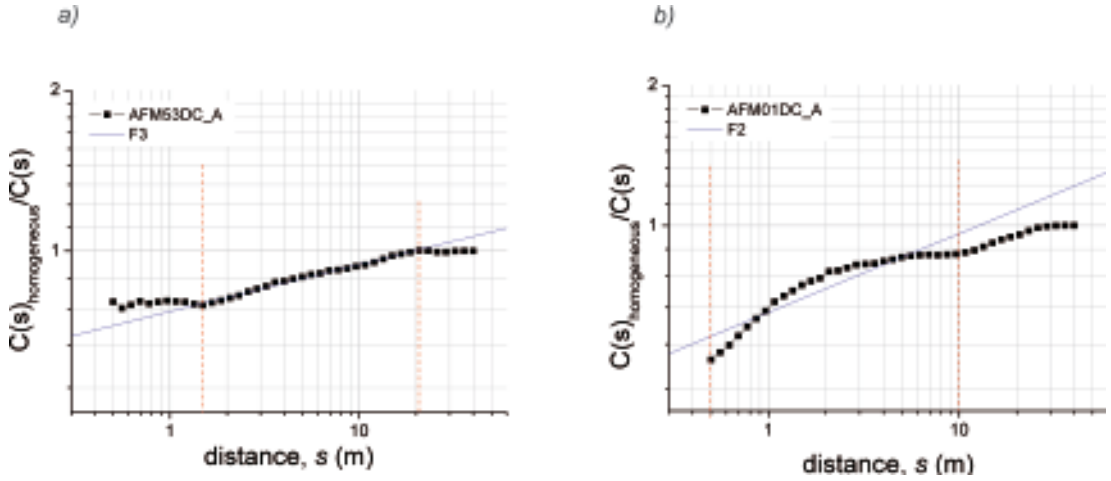

Figure 6-4. *Evolution in a log-log diagram of $C_{homogeneous}(s)/C(s)$ (in black squares). The quantity $C_{homogeneous}(s)/C(s)$ is expected to be a straight line of slope $(2-D_{2d})$ in the log-log representation. Boundaries of the fit are represented as dashed red lines. The linear fits (blue lines) for AFM000053 (a) and for AFM100201 (b), have been attributed respectively a confidence level of 3 and 1 (for a fit performed within the milestones provided in Table 6-1).*

Table 6-1. Summary of fractal dimensions D_{2d} measured for the different outcrops. See text for details.

Outcrop	b_{min}	b_{max}	Confidence level	D_{2d}	Indicative uncertainty
AFM000053	1.5	20.7	3	1.91	0.01
AFM000054	0.7	9.6	2	1.93	0.05
AFM001097	0.7	28	2	1.93	0.05
AFM100201	0.5	10	1	1.83	0.15
AFM001098	0.5	8.6	3	1.90	0.05

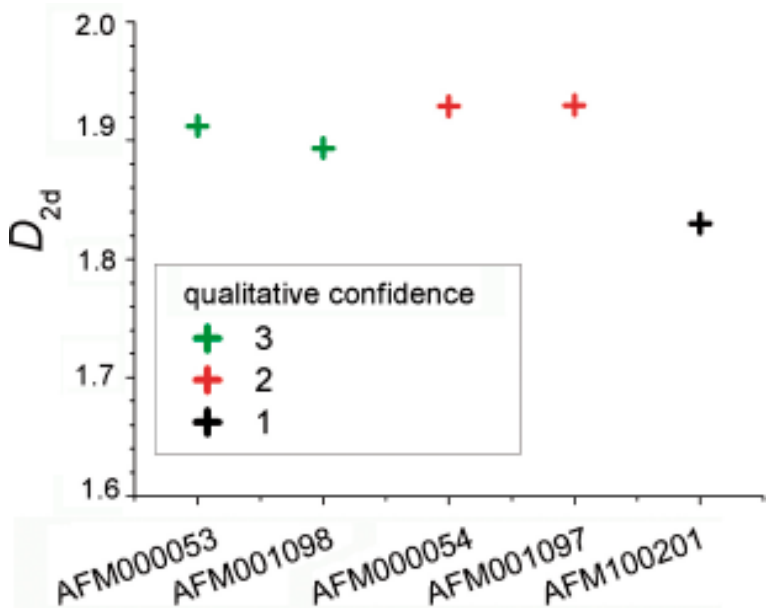

Figure 6-5. *Fractal dimensions D_{2d} measured over the five outcrops datasets.*

All the outcrops except AFM100201 display well defined (over at least one order of magnitude each time) fractal dimensions comprised between 1.89 and 1.93. Between the boundaries b_{min} and b_{max}, defined for each dataset, local variations of the slope are expressed through the "indicative uncertainty" and the confidence level. Outcrop AFM100201 has the smallest dimension (1.83) associated to a poor confidence level (local variations of the slope are important). There is no clear explanation for that behaviour. On this outcrop the clustering seems to be more pronounced (see pictures in Appendix 1) than on the other ones.

Note that if the method would be applied on a homogenous fracture centre distribution (arising from a poissonian process), the resulting curve of $C_{homogeneous}(s)/C(s)$ would be flat, leading simply to D_{2d}=2. Therefore, the apparent fractal clustering observed here (D_{2d}<2), also weak, can not result from a poissonian distribution.

By averaging over the 5 outcrops, we obtain D_{2d}=1.90±0.04. If AFM100201 is excluded, we obtain D_{2d}=1.92±0.02. Then the variability from one outcrop to the other does not exceed the indicative uncertainty defined for each dataset separately. All the outcrops except AFM100201 are consistent with a fractal dimension D_{2d} of 1.92±0.02. This indicates only weak (or subtle) fractal correlations.

6.2.5 Fracture trace density distribution

For the fracture trace map analyses, the density distributions functions $n_{2d}(t)$, noted $n(t)$ for simplicity, can be written as (see Section 4.2.3):

$$n(t) = \frac{N(t,L)}{A} \cdot L^{2-D_{2d}} \qquad \text{Equation 6-1}$$

where A is the outcrop area, L the typical linear size of the area ($L = A^{1/2}$), t the fracture trace length, D_{2d} the fractal dimension. $N(t,L)$ is equal to the number of fracture traces whose length is between t and $t+dt$. It is calculated from the fracture trace map dataset and next normalized to obtain the proper value of $n(t)$. The method used is based on a logarithmic binning /Darcel et al. 2004 Section 3.1, Davy 1993/.

In the following the density distribution functions are normalized by the map areas (A). This choice is mainly motivated by the weak fractal correlations measured over the outcrop trace maps and by the uncertainty attached to the measure (Section 6.2.4): D_{2d} is estimated to be in between 1.9 and 1.95. As a consequence, the fractal dimension associated to the DFN model is of second order importance when deriving the density length distribution parameters ((k_t+1) and α_{2d}). Anyway the potential error associated to this assumption is quantified through the factor $L^{2\text{-}D2d}$. Given the uncertainties related to the determination of A (see Appendix 1), L, D_{2d}, the uncertainty reported to the density term can be estimated by a factor between 1.15 to 1.4. As will be seen in the section, this variation is less than the observed variations in apparent density from one outcrop to the other. The consequences on the scaling analysis are mentioned in a dedicated section (Section 7).

The density-lengths distributions are thus calculated (Figure 4-1 recall how the length exponent a_{2d} and the density term and α_{2d} can be measured from the density length distribution represented in a log-log diagram); all the curves are displayed in Figure 6-6a to f. On each graph, the curve $n(t)$ (green line plus symbol curve), plus the local fits (in black) and the outcrop scale models (in orange, see Section 7.2) are provided. Local variations of logarithmic slope are displayed as inlet below the density-length distribution (in blue).

For outcrops AFM001097 and AFM100201, only one well defined trend is present. The resulting power-law fit leads to an exponent a_{2d} =2.5 eq. to k_t=1.5. For the remaining outcrops, the curves $n(t)$ are slightly curved. This effect is apparent for instance when observing the variations of $n(t)$ for the outcrop AFM000054 (Figure 6-6d); from a purely statistical point of view, the concave shape of the bi-logarithmic plot suggests that different regimes may exist, here above

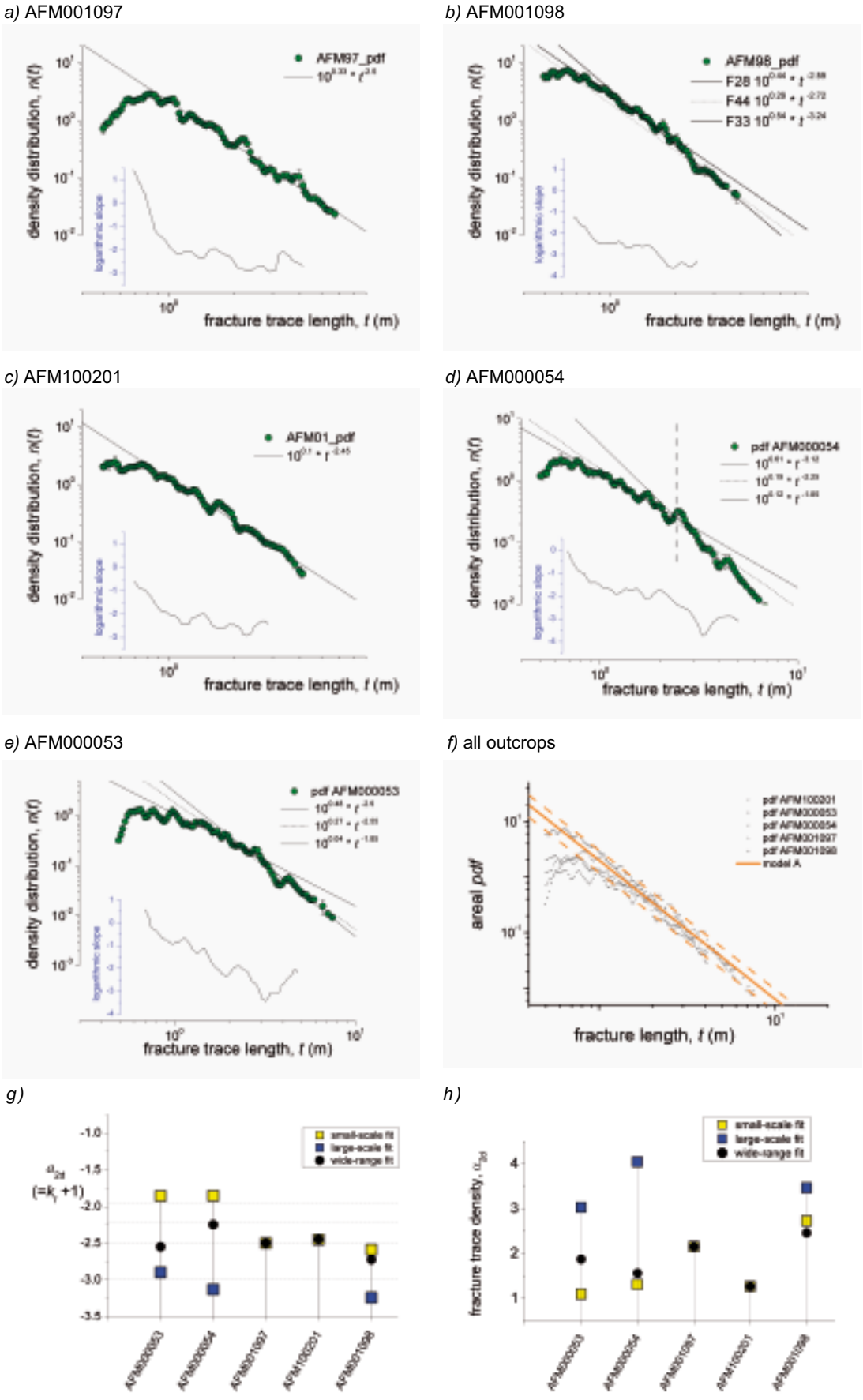

Figure 6-6. *Density length distributions for the 5 outcrops. Local variations of the local logarithmique slope are displayed in insert (blue). Density lengths distributions for the 5 outcrops, a_{2d} (=k_t+1) in g) and α_{2d} the fracture trace density in h).*

and below 2.5 m. Because it is difficult to say that these regimes are physically and statistically sound, we choose to derive 3 power-law fits for AFM000054 (note that derivation of a_{2d} and α_{2d} are simultaneous):

- above 2.5 meters: a_{2d}=3.1 (eq. to k_t=2.1) and α_{2d}= 4.1,
- between the map resolution scale and 2.5 meters length: a_{2d}=1.85 (eq. to k_t=0.85) and α_{2d}=1.32, and
- through the entire range of admissible scales: a_{2d}=2.15 (eq. to k_t=1.15) α_{2d}= 1.55.

We do not believe that the 3 fits are sound and valid, but this exhaustive methodology combined with arguments on the scaling consistency of the DFN model should permit us to capture the most likely model. Each dataset is therefore firstly treated individually and, when possible, several fits are considered, to reflect:

- the trend of the smallest sizes (fit called "small-scale", yellow square on Figure 6-6g and h),
- the trend of the largest sizes (fit called "large-scale", blued square on the same figure), and
- the mean behaviour, over both the small and larger sizes (fit called “wide-range”, black circles on the same figure).

The power-law fitted models are summarized in Figure 6-6g and h. Large discrepancies appear both between the fits within a single outcrop and from one outcrop to the other: the exponent a_{2d} (eq. to k_t+1) varies between 2 and 3 and α_{2d} varies simultaneously from a factor two to three (Figure 6-6g and h). The slope variation between smallest and largest scales is more pronounced for outcrop AFM000054 (Figure 6-6d). Variations of local length exponents between 2 to 3 (k_t varies from 1 to 2) correspond in fact to almost all the possible values classically associated to natural systems. However, many of the fits performed reflect the finite size of the samples, the outcrop map special shapes and resolution effects.

When plotting the 5 density length distributions on one single graph (Figure 6-6f), the distributions do not appear very different the one from the other. The two enveloping curves displayed (dashed orange lines in Figure 6-6f) have the same slope (a_{2d} =–2.5) and densities equal to 1.2 and 3. In other words, for equivalent values of a_{2d}, the density term α_{2d} may vary by a factor of two. Discrepancies appear mainly from a size equal to 0.8 and towards shorter lengths. Over that range of scale it appears difficult to distinguish between real tendency and resolution sampling effect.

Finally we underline that the density length distribution related to AFM001097 does not display a distinct signature, although a very large proportion of the fracture traces included in the analysis belong to a deformation zone.

6.2.6 Local models

For each outcrop one can define a “local DFN model” that matches precisely the outcrop dataset. The range of validity of such a model is restricted: it is a priori usable only at the exact outcrop geographical position. Validation simulations (code 3FLO, reference in Section 10) are performed in order to check the DFN parameters consistency with the dataset. At that stage, the model parameters are derived from stereological rules (4.2.3) for the exponents a_{3d} (eq. to k_r) and D_{3d}. Also, the relation between the orientation distribution and the density term α_{3d} (parent distribution) leading to the value of α_{2d} (apparent density on a planar outcrop) is fitted through a simple trial and error process[9].

The model local_AFM001097 is defined, in 2D, with a_{2d}=2.5 (eq. to k_t=1.5) and α_{2d}= 2.14. The location parameter is not known (resolution effects inherent to fracture trace mapping prevent

[9] A complete calculation of the link between orientations and density terms is provided in the next chapter.

from observing r_0). In order to simplify the numerical simulation process, D_{2d} is approximated to 2 (also it was measured equal to 1.93±0.2). Consequently, the fractal correlation, due to a fractal dimension D_{2d} equal to 1.93±0.2, will not be reproduced. We recall however that taking D_{2d} equal to 2 is consistent with the density term also provided (Section 6.2.5). In complement, the orientation distribution is expressed in term of Fisher distributions (parameters are provided in Appendix 1).

Numerical modelling coupled to the trial and error method lead to a parent distribution, for the model "local_AFM001097", to the following parameters: a_{3d}=3.5 (k_r=2.5), α_{3d}= 3.2 and D_{3d}=3 (and $P_{32}(r_c=0.1)$=11.24 , Equation 4-12), with the orientation distribution recalled in Appendix 1.

The fracture trace map characteristics arising from model "local_AFM001097" are illustrated for one realisation local_AFM001097 (Figure 6-7). The parent fracture density distribution can be generated down to any minimum fracture radius[10]. In the present case, it is arbitrarily generated down to a fracture radius equal to 0.4; accordingly the 2D fracture trace length distribution simulated departs from the power-law model for fracture traces shorter than 0.8 m (Figure 6-7e). One can observe the qualitative consistency between the real and simulated fracture trace map (Figure 6-7a and b) consistency between trace length distributions (Figure 6-7e) and orientation distributions (Figure 6-7c and d). The same procedure can be simply repeated to provide the local models related to the five outcrops.

In the next section the model local_AFM001097 is employed as a support to analyse the scanline data.

6.2.7 Consistency with scanline data

Use of scanline data

The 2D fracture trace mapping is complemented by a scanline sampling at different places of the site, in particular on the five outcrops analysed above (see Table 6-2). We illustrate here how the scanline sampling could contribute to the DFN modelling process. Indeed, scanlines should potentially be used to assess the model validity between 20 and 50 cm, at least locally for the five outcrops.

During scanline sampling, fractures whose apparent trace length is equal to or larger than 20 centimeters are recorded; several characteristics are recorded: the intersection position, the trace length, orientation etc. Scanlines constitute therefore potentially additional information that can contribute to the DFN modelling process.

Table 6-2. Fracture intensity along scanlines.

Name	Fracture intensity (P_{10})	Outcrop
LFM000007	2.3	AFM000053
LFM000008	3.9	AFM000054
LFM000009	2.9	AFM000053
LFM000010	3.0	AFM000054
LFM000576	2.9	AFM001097
LFM000577	1.7	AFM001097
LFM000578	5.4	AFM001098
LFM000579	3.0	AFM001098
LFM000655	1.1	AFM100201
LFM000656	2.6	AFM100201

[10] This does not affect the relation between α_{2d} and α_{3d}.

a) simulated trace map local_AFM001097

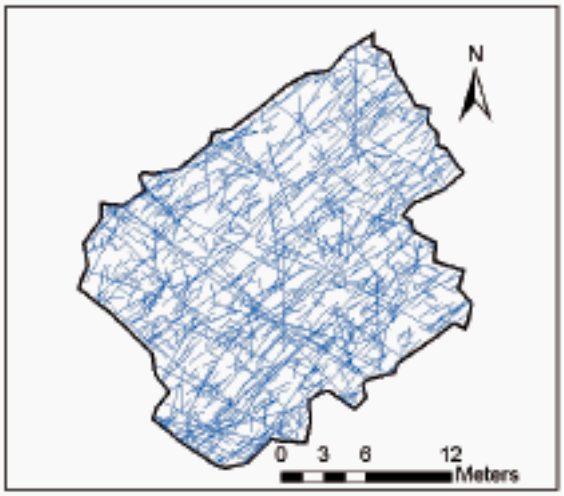

b) data: trace map AFM001097

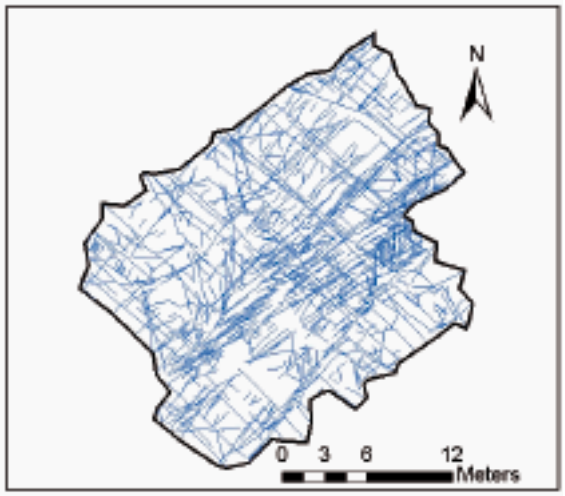

c) Simulated orientation distribution

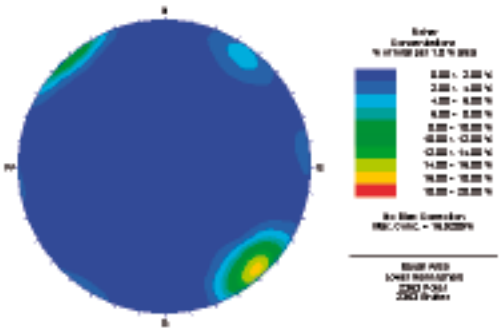

d) data: orientation distribution

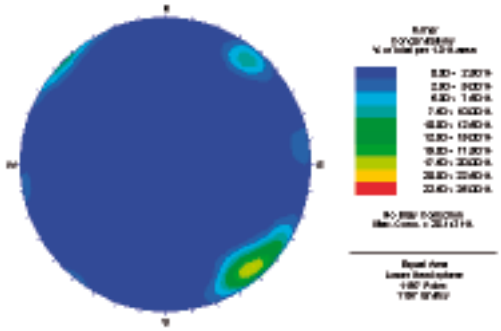

e) simulated and data density length distributions

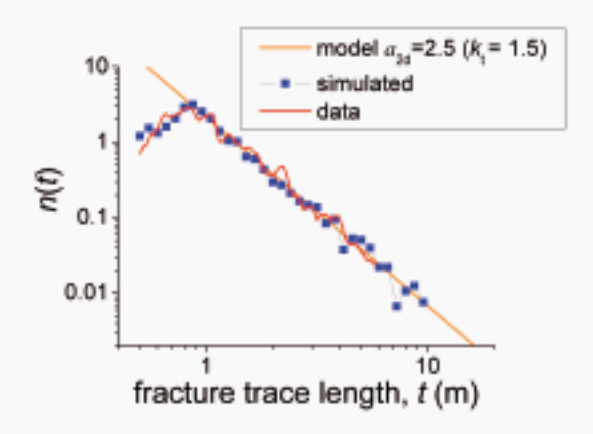

Figure 6-7. *Comparison of the model local_AFM001097 with the corresponding dataset. Parameters of local_AFM001097 are:* a_{3d}*=3.5 (*k_r*=2.5),* α_{3d}*= 3.2 and* D_{3d}*=3 (and* $P_{32}(r_c=0.1)=11.24$*), with the orientation distribution recalled in Appendix 1.*

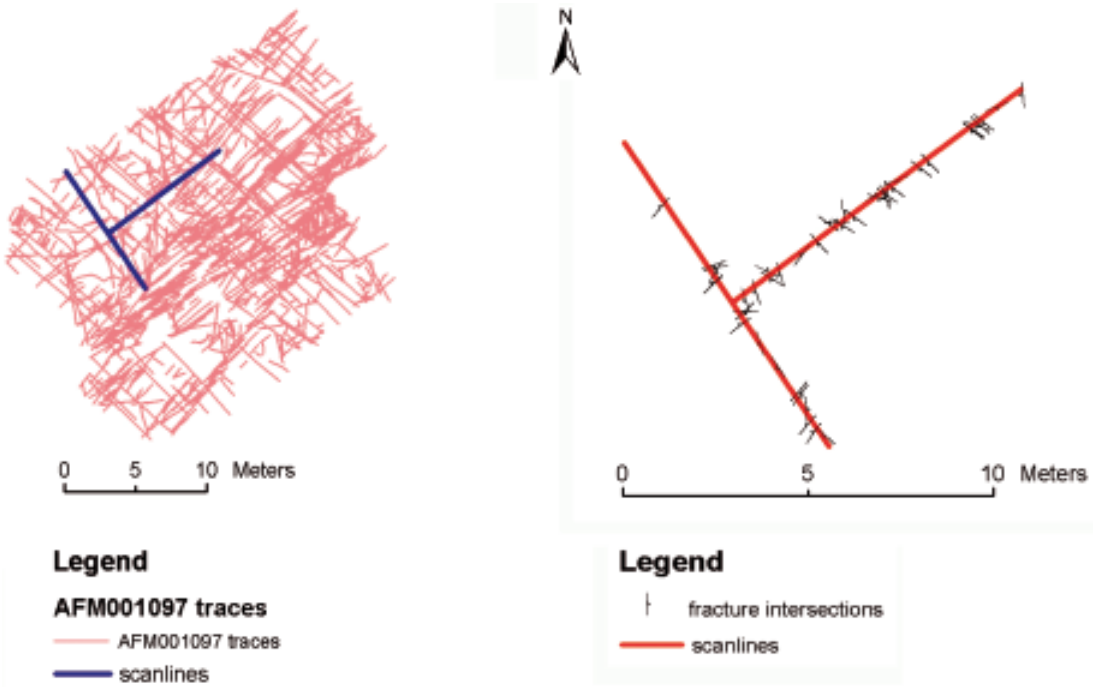

Figure 6-8. *Scanlines on outcrop AFM001097.*

In the present case a total of 288 fracture intersections are recorded along 10 scanlines (see Table 6-2) for a cumulative length equal to 99.3 meters. On each trace map, scanlines are gathered by pairs of perpendicular directions. The scanline orientations differ from map to map. Locally, the fracture intensity (averaged over the 2 perpendicular directions) is comprised between 2.3 and 4.7 fractures per meters; the mean fracture intensity is 2.9. The ratio between fracture intensity measured on two perpendicular scanlines for each outcrop is comprised between 1.26 (AFM000053) and 2.36 (AFM100201).

The number of scanlines per outcrop combined to the quantity of fractures sampled is considered to be too low to enable a length, an orientation or an integral of correlation analysis. We propose nevertheless to check the consistency between the measured scanline fracture intensity and the 2D-3D DFN model parameters. This provides also a picture of the 1d fracture intensity variability intrinsic to the DFN Model. Numerical simulations (software 3FLO, /Billaux et al. 2005/) are used to test the 1d fracture intensity consistency between the trace map and the scanline map records. Model local_ AFM001097 is selected to perform the analysis (see Section 6.2.6).

Numerical modelling

Fractures (from DFN model local_AFM001097 whose parameters are recalled in Section 6.2.6) are generated by their centers within a 3D cubic domain of edge E=30 m (see Figure 6-9). A 2D horizontal sampling plane and two sampling lines are defined. The two scanlines are ten meters length and oriented like LFM000576 and LFM000577 (resp. noted T2 and T1 in Figure 6-10 and Figure 6-11) on AFM001097. Since field scanline sampling is simulated, the shortest fracture traces to be recorded are equal to 20 cm. Then fractures whose radius is smaller or equal to 10 cm are simply not generated and fracture traces shorter than 20 cm do not contribute to fracture intensity estimate.

A large number of realisations is performed. Each time the fracture intensity along the two scanlines is recorded. Mean values and variability of the fracture intensities simulated along the scanlines are next estimated over all the realizations.

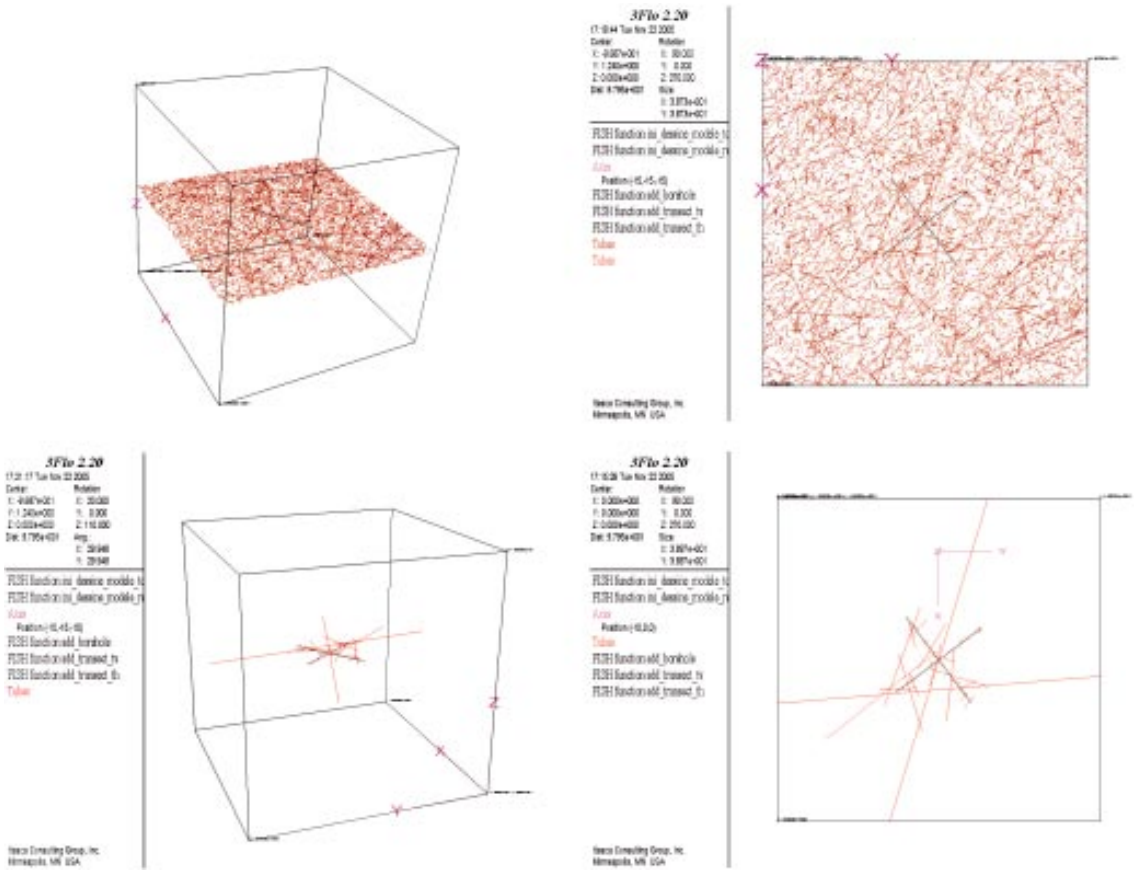

Figure 6-9. *Numerical simulation illustration (code 3FLO, /Billaux et al. 2005/). Fracture discs are generated in 3D. Fracture traces on the sampling plane are displayed above and fracture traces intersecting the scanlines are displayed below. Convention: X to the South, Y to East and Z to growing elevation.*

From model local_AFM001097, two models are considered: one with a minimum fracture radius (r_0) equal to 0.4 m (apparent size at which the fracture trace density departs from the power law model when going towards small scales) and the other with r_0 equal to 0.1 (corresponds to a fracture diameter of 0.2, equal to the cutoff length applied during scanline sampling). Results are presented in Figure 6-10.

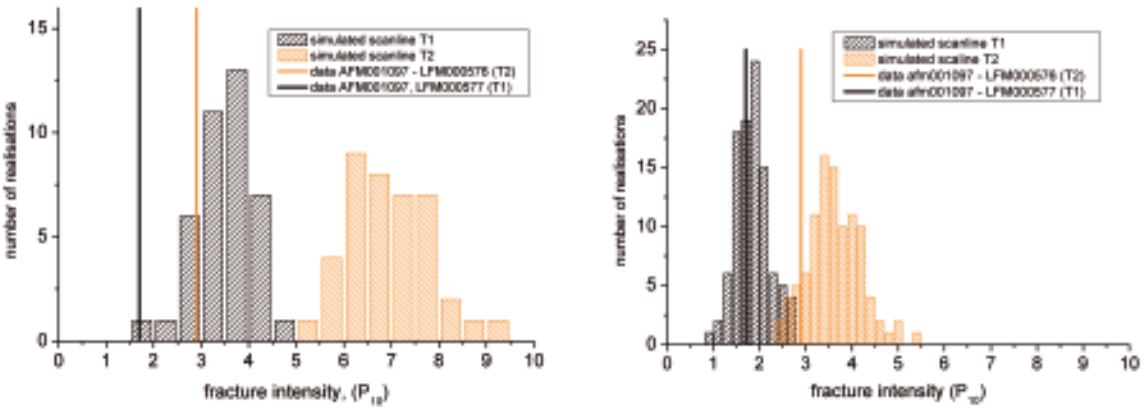

Figure 6-10. *Histograms of fracture intensity along scanlines (left) r_0 =0.1, 40 realisations (right) r_0 =0.4, 100 realisations. Column/bars are results from numerical simulations, dashed lines are the values measured on the scanlines from AFM001097.*

The simulation process provides an illustration of the intrinsic variability of the DFN **model** considered. In that case the mean fracture intensity is representative of the DFN model and several realisations are necessary to catch it. Qualitatively, the simulated value of fracture intensity for one realisation can differ up to roughly a factor 2 from the mean value.

The model with r_0 equal to 0.1 predicts mean fracture intensity about twice the values observed, whereas the model with r_0 equal to 0.4 seems to be more consistent with the data. Additional simulations are performed to calculate the evolution of the mean fracture intensity with r_0 (Figure 6-11). Results show that even the model with r_0=0.4 tends to overestimate the number of fracture intersections along the scanline. Fracture intensities measured on all the scanlines are reported in the figure. However scanline orientations vary from one place to the other; it is therefore difficult to perform a direct comparison of all the fracture intensity values (grey dotted lines in Figure 6-11).

A tentative interpretation of the former comparison would indicate that the limit of the power law model validity could be comprised somewhere in the range of twenty to fifty centimeters (which is larger than the borehole diameter). However, the scanline data representativity and the model assumptions must be kept in mind. For the moment (local scale) the model reproduces only the fracture length and orientation distribution; for the present simulation purpose the fractal clustering was not reproduced in the modelling; no domaining were defined within the AFM001097 area. In other words, the density parameter evaluated reflects the *mean* fracture intensity. Numerical simulations have shown that even with such a simple model the apparent values of P_{10} measured on the two scanlines (potentially vary by a factor 2 to 3, from one realisation to the other (Figure 6-10). Several very different interpretations could be considered:

- uncertainty: the true limit of the sampling process is not equal to 0.2 but larger (thin fractures not seen by the human eye?),
- the number of small fractures is not satisfactorily modelled by the local_AFM001097 power-law model,
- the scanline data of AFM001097 sample a low density zone of the outcrop; this is illustrated on Figure 6-12, were only the traces have been used (limit set to 50 cm). Nevertheless, a virtual scanline couple is located at a place were the fracture intensity is almost 2.5 times higher than for the real scanline position. The model is for the moment representative from a mean density (established as an average over all AFM001097) whereas the scanline data is representative for a low density.

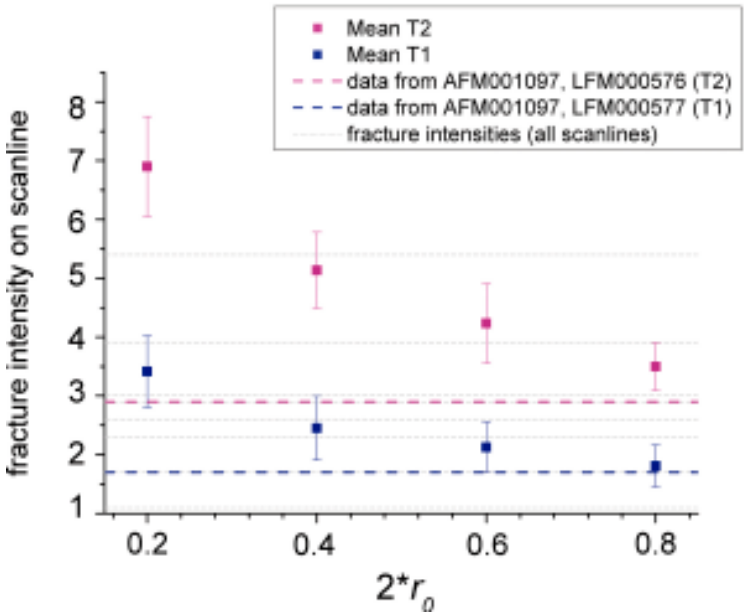

Figure 6-11. *Evolution of the mean fracture intensity for different r_0.*

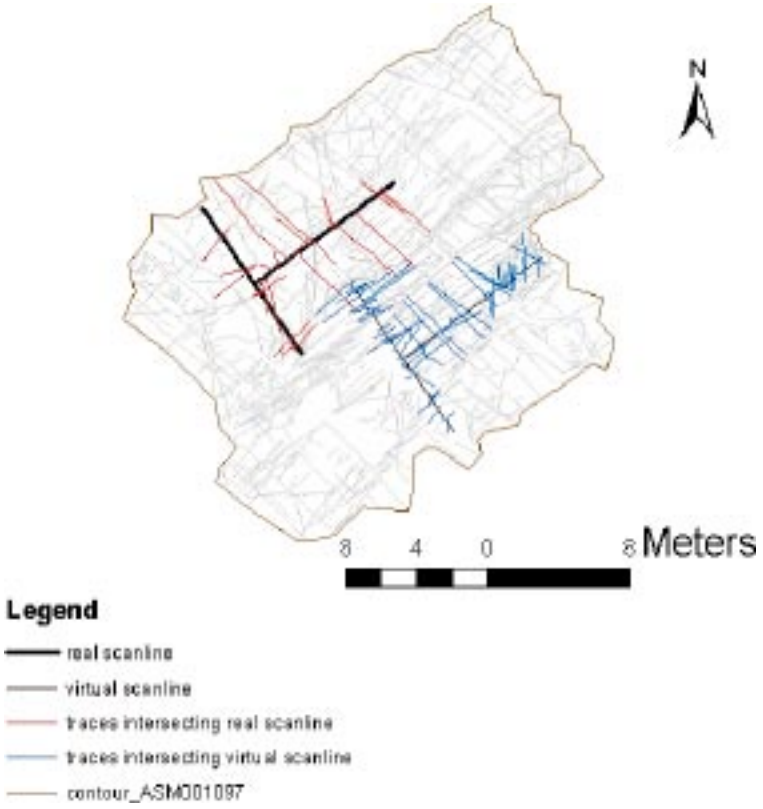

Figure 6-12. *Variability of scanline sampling illustrated on the traces off outcrop AFM001097. Scanline sampling (cutoff 50 cm) performed leads to 27 intersections (scanlines in thick black) and virtual scanline sampling leads to 65 intersections (traces in blue).*

The present basic comparison between data and model has shown that a factor of two on the P_{10} value may arise from the DFN and scanline respective orientations, from the data location (Figure 6-12), from the stochastic nature of the modelling, even for a Poissonian spatial process and obviously from the power-law model scale range of validity. Although the data available here prevent to draw a general conclusion about the power-law model validity towards small scales, we have shown here how they can be used to check the model consistency. As a conclusion about the use of scanline data, whatever the assumption about r_0 and the model obvious departure from reality, the fracture intensity simulated or measured varies rather from a factor of two than from an order of magnitude. Variability is significant (Figure 6-12). Many explanations can be invoked. At that stage this can be viewed as an uncertainty of the modelling process. The issue of model validity towards smallest scales will be further investigated when interpreting the borehole data.

We therefore can doubt that two scanlines per outcrops are sufficient to catch the fracture intensity variability on each outcrop. In addition the total number of fractures sampled along one scanline is to low to allow a length and/or an orientation analysis (see also /Darcel et al. 2004/ where an attempt were made to analyse the lengths). The number of fracture traces per outcrop is slightly larger than one thousand whereas the number of fracture sampled through the scanline is less than fifty elements. Note additionally that the apparent length exponent along the scanline should be (a_{3d}-2); the smallest fractures are proportionally less sampled.

On one side, the local 1d fracture intensity variability can potentially arise from many sources (the scanline orientation, the lmin, the lengths, the local density etc). On the other side, the scanline dataset is restricted to two samples by outcrops, containing a small number of fractures. In that sense the scanline dataset analysis must be taken cautiously. We consider the analysis here as exploratory.

6.2.8 Outcrop model

Approach

The local models defined in Section 6.2.6 are related to the geographical position and to the Rock Domain of the datasets they are derived from. Given the relatively limited number of datasets available to sample the different Rock Domains present on the site, and given the results of Section 6 (no striking difference between trace length distributions from one RD to the other), it is not justified to differentiate the DFN models properties from one RD to the other. Accordingly the aim of the "outcrop model" to be defined here is to provide a mean DFN model, at the outcrop scale (10 meters), that could be used as a proxy over the whole model areas. The outcrop model should catch the main characteristics of the fracture system, in terms of fracture size and orientation distribution, and spatial centre density distribution. Obviously the "outcrop model" will differ slightly from the local models.

The determination of mean DFN models is the central axis of the present developments. Although a full description of the DFN model variability is obviously fundamental, we have put emphasis on the determination of mean parameters; it was beyond the scope of the present work to fully describe the variability.

Orientations

In previous sections it has been shown that the orientation distributions of the different outcrops present large similarities (Figure 6-3). Then we chose to combine the outcrop datasets to define a "2d global orientation" distribution of the candidate model. By doing this, one obtains a total of almost 6,000 fracture orientations from which a bulk orientation distribution is derived (Figure 6-13). Note that the apparent regular repartition of fracture poles every five degrees in the dip direction and every 10 degrees in the strike direction reflects the precision on orientation measurements (Figure 6-13).

The orientation distribution is then subdivided into several subsets based on the main local peaks of intensity observed. Three of them have horizontal poles (i.e. vertical fractures), the fourth is made of subvertical poles (horizontal fractures). The global orientation distribution is modelled by 4 sub sets of fractures characterized by a Fisher distribution. We note that the only way to reproduce exactly the observed orientation distribution is to use bootstrapped orientation. The division in 4 sets constitutes a simplification that reproduces the principal characteristics of the orientation distribution.

In summary, 4 orientation subsets are defined (see Table 6-3), 3 close to vertical and one close to horizontal. The main vertical set is trending NE; it contains more than half of the fractures that intersect the outcrop plane. The second set contains around one third of the total. These two sets are ubiquitous in the different outcrops, with a mean strike of N200 to N230 for the NE set, and N110 to N125 for the WNW set (except for AFM100201). The remaining subset includes the horizontal fracture (dip≤45°). We note here, that the two main sets present on the fracture trace map (NE and WNW) are also visible on the lineament map (Figure 5-2). However the proportion is different: the NE set prevails in outcrop maps, while the orientations are more equally distributed between the different sets in the lineament map.

Density-length model

As was shown in Section 6.2.5, the restricted range of scales available to perform a power-law fit prevents from defining easily the power-law exponent from the sole outcrop scale trace map datasets[11]. We nevertheless here define a mean density-length model with parameters α_{2d}=1.85 (Figure 6-6h) and a_{2d}=2.5 (eq. to k_t=1.5; Figure 6-6g). Locally (depending on the observed outcrop), the density term can vary up to 50% (in Figure 6-6f), orange straight line, plus

[11] The scaling analysis is provided in the next chapter.

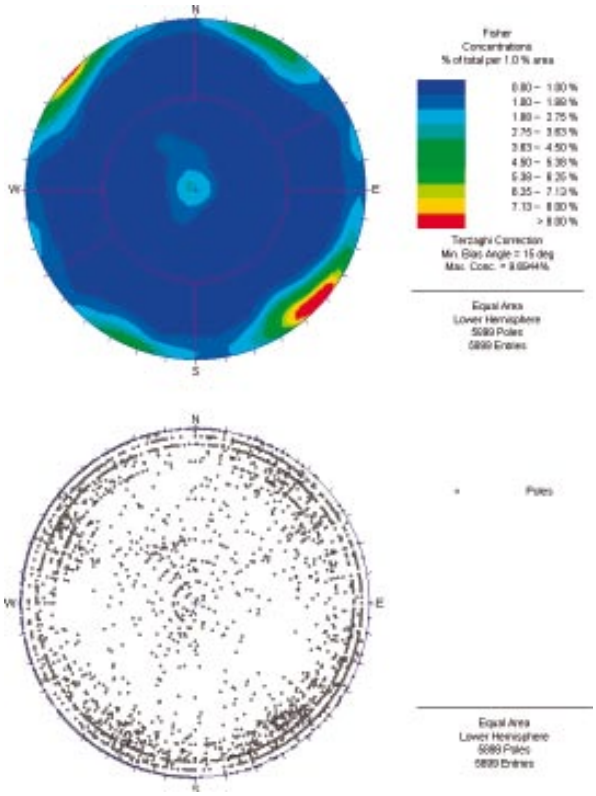

Figure 6-13. *Stereoplots from outcrop datasets (Schmidt projection, equal Area, lower hemisphere), pole (below) and contour (top) plots. 4 main sets are defined from the diagram (black lines), 3 of them being subhorizontal and the remaining subvertical.*

variations by about 50% in density, plus and minus, in orange dashed lines). The parameters of the first 2D candidate model are recalled in Table 6-4. The consistency of this model is further assessed in Chapter "The Scaling Model".

Table 6-3. Division in sets of the combined outcrop dataset.

SET	Mean strike	Mean dip	K	Apparent weight (in %)	Bulk weight (in %)
NE	224	88	13	57	51.8
WNW	119	88	18	28	25.8
NNW	163	87	25	09	7.9
SUBHZ	62	7	15	05	14.5

Table 6-4. 2D candidate site model called Model A[12].

Model name	a_{2d}	k_t	α_{2d}	D_{2d}	Orientations
Model_A	2.5	1.5	1.85	2.	"outcrop" Table 6-3

[12] "Model A" refers to a mean model whose main parameter is the length exponent *a* (eq. to *k*+1). *a* is fixed whereas the density term and fractal dimensions are defined on average. Derivations of Model A rely on variations of density term and fractal dimensions. The DFN candidate models definitions are recalled in Section 7.2 and 8.

6.3 Lineaments

The lineament map covers the regional model area (Figure 6-14a). Contrary to the outcrop fracture trace maps, the lineaments are linked. Lineament mapping is a difficult exercise that consists in linking at best segments whose fracturing nature is not completely assessed (see /R-04-15/ Section 4.2.3 and Figure 4-14 for details). After the linking process, the largest lineament size recorded is comparable to the regional model scale, with a lineament that cross cuts the entire model area in the NW direction.

The resolution scale of the lineament map is estimated at 200–300 m. However, the regional lineament mapping is performed both inland and offshore, leading to local variations in resolution scale. In short, the resolution is much better inland than offshore, which causes an apparent decrease of the fracture density from the continent to the sea. As a consequence the density length distribution requires in itself a scaling analysis: depending on the location and on the fracture lengths, the resolution differs, entailing complexity for defining the map area and normalising the distribution.

To deal with the abovementioned issue (the density length distribution analysis requires having a unique resolution scale within one map), the lineament map is separated in two analysis domains (Figure 6-14b). We assume that each resulting domain has a distinct but constant resolution scale. The variations, in terms of resolution scale, between the undersea and the mainland lineaments are illustrated in Figure 6-14a. The aerial subarea displays a smaller resolution scale than the sea area.

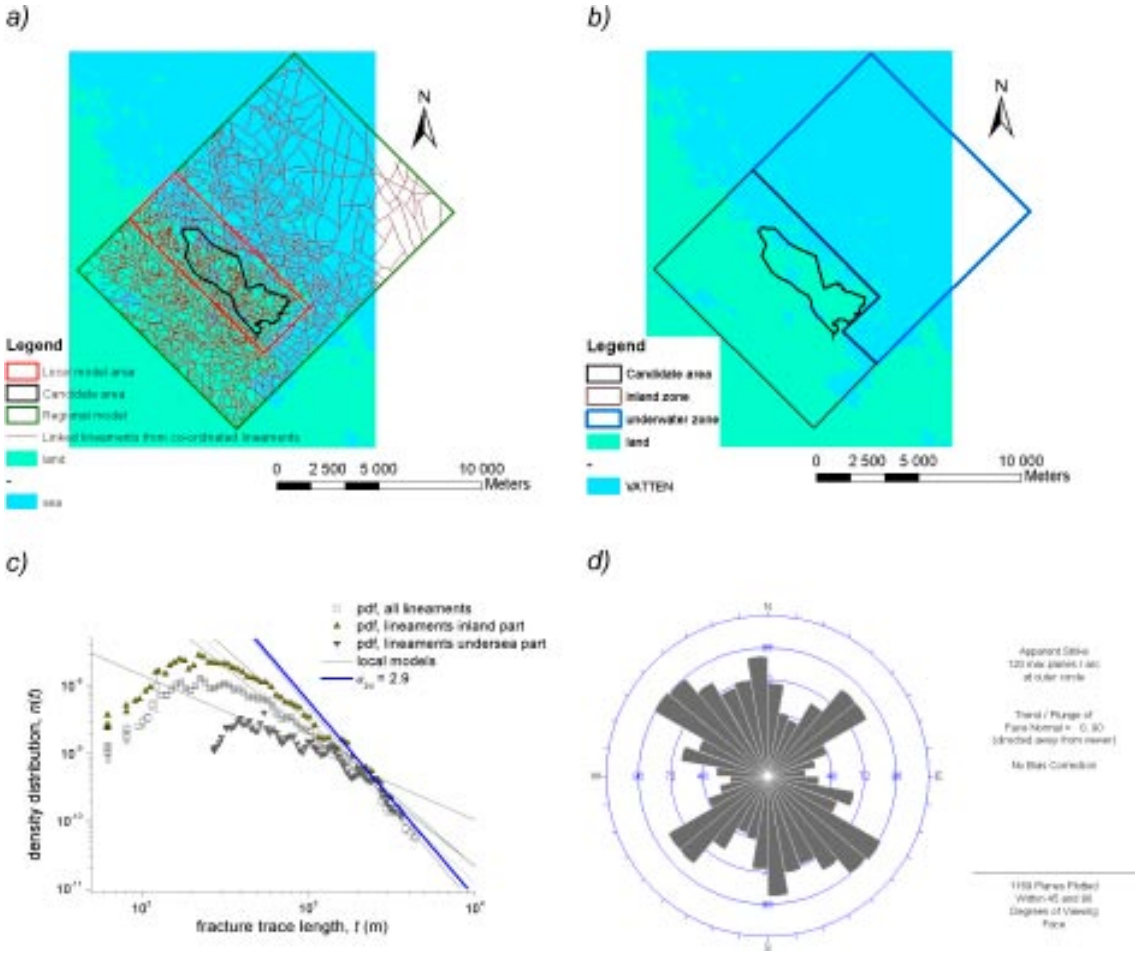

Figure 6-14. *(a) Lineament traces within the regional model contour, 11 by 15 km; local major lineaments are in green, local minor in violet and regional lineaments in brown. (b) Definition of two analysis-domains. (c) Density distribution n(t) for the complete lineament map, the inland part and the undersea part, (d) Rosette diagram of the complete lineament map.*

Many trends could be measured on the density distribution curves, with several possible power-law fits, from values close to –1 (central part of the undersea set) up to –2.95 (largest lineaments, above one km). These trends result partly from the mixing of resolution scales. The only trend apparent on both datasets is encountered for the largest scale (a_{2d}=2.95, eq. to k_t=1.95).

Due to the resolution differences that are clearly observable for the lineament dataset, we have not attempted to calculate the fractal dimension associated to the integral of correlation.

The lineament orientation information is restricted to strike. As illustrated in a rosette diagram (Figure 6-14c), the strikes are broadly distributed, with nevertheless three main directions, estimated visually, of striking towards NW (300–320), NS (350–360) and NE (40–50).

6.4 Borehole data

6.4.1 Introduction

Data collected in borehole logs are very complex and rich. This complexity raises the problem of fracture definition. Therefore assumptions related to the link between the 2D-fractures analysed above and the 1d-fractures sampled along boreholes are briefly reviewed before proceeding with the borehole analysis. In the present section the analysis remains descriptive (or "local", by analogy to the 2D descriptive analysis in Section 6.2). Inter comparison between different boreholes and between scales is the object of the Chapter Scaling Model.

To provide a simple overview of the underground data variability, a global analysis of spatial correlation (through D_c) is presented. Next, due to time constraints, the analyses are limited to two boreholes, KFM02A and KFM05A. These 2 boreholes were chosen as they somehow can illustrate potential variations in the site by their geometry and geographical location. We note that even though the different boreholes data are all gathered in one well formatted database, each borehole displays some particularities which preclude the use of fully automatic analysis procedures.

6.4.2 1d-fracture definition

Boreholes are a huge but very restricted window of observation at depth on the natural DFN. Additionally, boreholes can not be viewed exactly as 1d straight lines but rather as a slightly curved cylinder of finite diameter (see Appendix 4). Thus, one must keep in mind the difference between the sampled object (the natural DFN) and the sample support shape (the borehole).

In correspondence with the geometrical DFN, the following apparent geometrical parameters can be registered along boreholes:

- fracture occurrences: amount or fracture intensity (P_{10}),
- fracture orientations (strike and dip),
- fracture width.

Indications on spatial organization and variability can be derived from the fracture intensity. Of course, no information about fracture length can be directly registered along the boreholes. Both the fracture apparent orientation distribution and intensity distribution must be corrected from orientation bias. Even the intercomparison between two boreholes of different directions relies on the parent distribution through an orientation bias correction. In fact, the building of a parent DFN model from borehole observations necessarily relies on strong assumptions and is model-dependent.

Besides, three levels of "sampling" coexist in the boreholes:

- "**individualized fractures**": Fracture intersections exist and can be individualised (labels: Open, Partly open, Sealed Fracture): position, orientations and internal properties are recorded.
- Fractures appear in clusters, no individualisation is possible (labels: Open_crush, Sealed_Network): extension, approximation of a fracture intensity and some internal parameters are recorded.
- Large scale volumes, RU (Rock units) and DZ (deformation zones), are delimited from single hole interpretation; DFN is expected to be defined in the RU, however individualized fractures exist in both these types of volumes.

These three levels of sampling overlap. In addition, depending on the applications related to the DFN, the fracture status of open or sealed takes on a particular importance. We note that even if fractures can not be individualized, fracture intensity values are estimated. However, no information about orientation is available in the fracture clusters (crush zones or sealed networks).

In the following, we assume that the 1d-DFN corresponding to the 2D/3D DFN derived from the surface analysis includes the individualized fractures (partly_open, open and sealed) *that fully intersect the boreholes*. Nevertheless the internal complexity mentioned above must be kept in mind.

6.4.3 Global analyses

Some of the analyses have been applied directly to each borehole taken as one single dataset (open+partly open+sealed, RU and DZ zones together). In particular the fractal dimension associated to the integral of correlation is calculated for the different KFM – boreholes.

The integral of correlation method is applied on all the fracture intersection positions identified (in file p_frac_core) and visible in bips. Integrals of correlation are measured from a minimum distance s_{min}=0.1 up to s_{max}=500. Results are summarised in Table 6-5 and Figure 6-15 below.

A well defined single fractal dimension can be defined in each case, except for KFM01A where two tendencies are observable. The range of validity of the fit varies between 2 to 3 orders of magnitude.

If we assume that the variability is given by the variability of D_c from one borehole to the other, then the correlation dimension D_c, measured on 1d sample in the site is estimated to be equal to 0.9±0.05. This value is compatible with the value measured on the 2D data. This is indicative of weak fractal correlations.

Table 6-5. Fractal dimension measurements along boreholes.

Borehole	D_{1d}	b_{min}	b_{max}	Confidence level
KFM01A	0.96	0.1	10	3
KFM01A	0.82	10	500	3
KFM02A	0.86	0.1	400	3
KFM03A	0.82	0.1	10	3
KFM04A	0.95	0.2	200	3
KFM05A	0.89	0.1	505	2
KFM06A	0.92	0.5	500	3

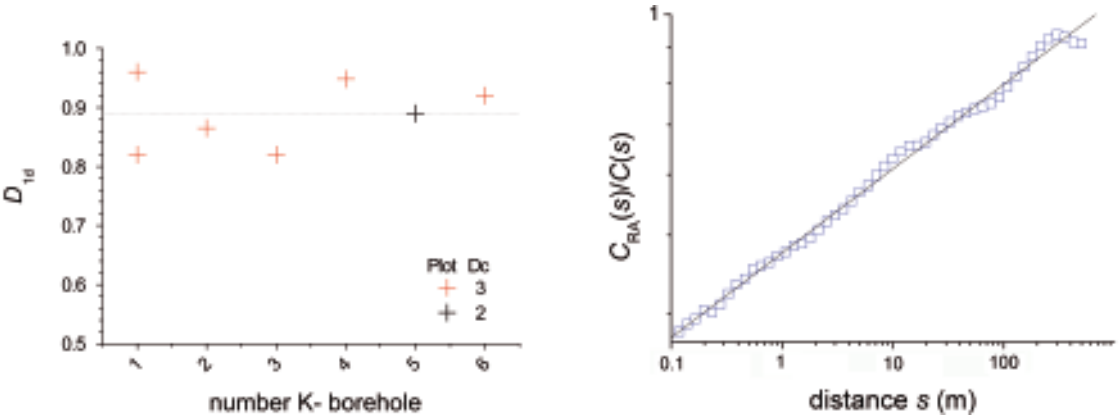

Figure 6-15. *Fractal dimensions measured along K-boreholes, (left) summary of measurements, (right) case of KFM02A.*

6.4.4 Descriptive local analyses

Borehole KFM02A

Preliminary remarks

KFM02A is a borehole close to vertical with mean trend and plunge of 275° and 85° respectively (Table 5-9 in /R-05-18/). The total borehole length is about 1,000 meters. We also note that:

- No data are registered between secup 96 and 100 meters, at the transition between two types of drilling, cored and percussion; however, zero values were assigned (in the database delivered) to the corresponding P_{10} values and a RU (RU1) is associated.
- 15% percent of the mapped fractures do not have any measurable orientation. This does not affect the P_{10} values.
- No sealed network[13] is mapped.

Description

On average, the fracture intensity (on individualized fractures) along KFM02A (RU and DZ together) is equal to **2.4**. When only the RU are counted, the average fracture intensity is reduced to **1.4** (see Table 6-6). In both cases standard deviations associated are above the mean values, thus reflecting a high variability. If every "type" of fracture is counted (fractures plus clusters of fractures, open and sealed) to estimate the fracture intensity, a value of **4.4** is reached. Although we do not discriminate here between the open and sealed fractures, we notice that individualized fractures are dominated by the sealed fractures (green bars to be compared to red and magenta bars in Figure 6-16b and c). Besides, the few crush zones are restrained within Deformation Zones and no information related to "sealed network fracturing" is recorded.

Table 6-6. Fracture intensities (from individualized fractures) measured on KFM02A.

KFM02A	Size	<P_{10}>	Sdv
ALL (RU+DZ)	[1:990]	2.4	3.1
RU	[1:728]	1.4	1.7

[13] "Sealed network" is a concept that started to be mapped after borehole KFM03A, so that no sealed network are mapped in KFM01A, KFM02A and KFM03A-B.

The fracture intensity high variability is furthermore illustrated through the subdivision of this borehole in terms of RU and DZ (Figure 6-16a), and through the variations of fracture intensity (Figure 6-16b). The variability observed here is only partly reflected in the fractal dimension measured between 0.86 and 0.9 (Section 6.4.3). The geological complexity and the variations in intensity observed from one RU (and DZ) to the other are displayed Figure 6-16c and d.

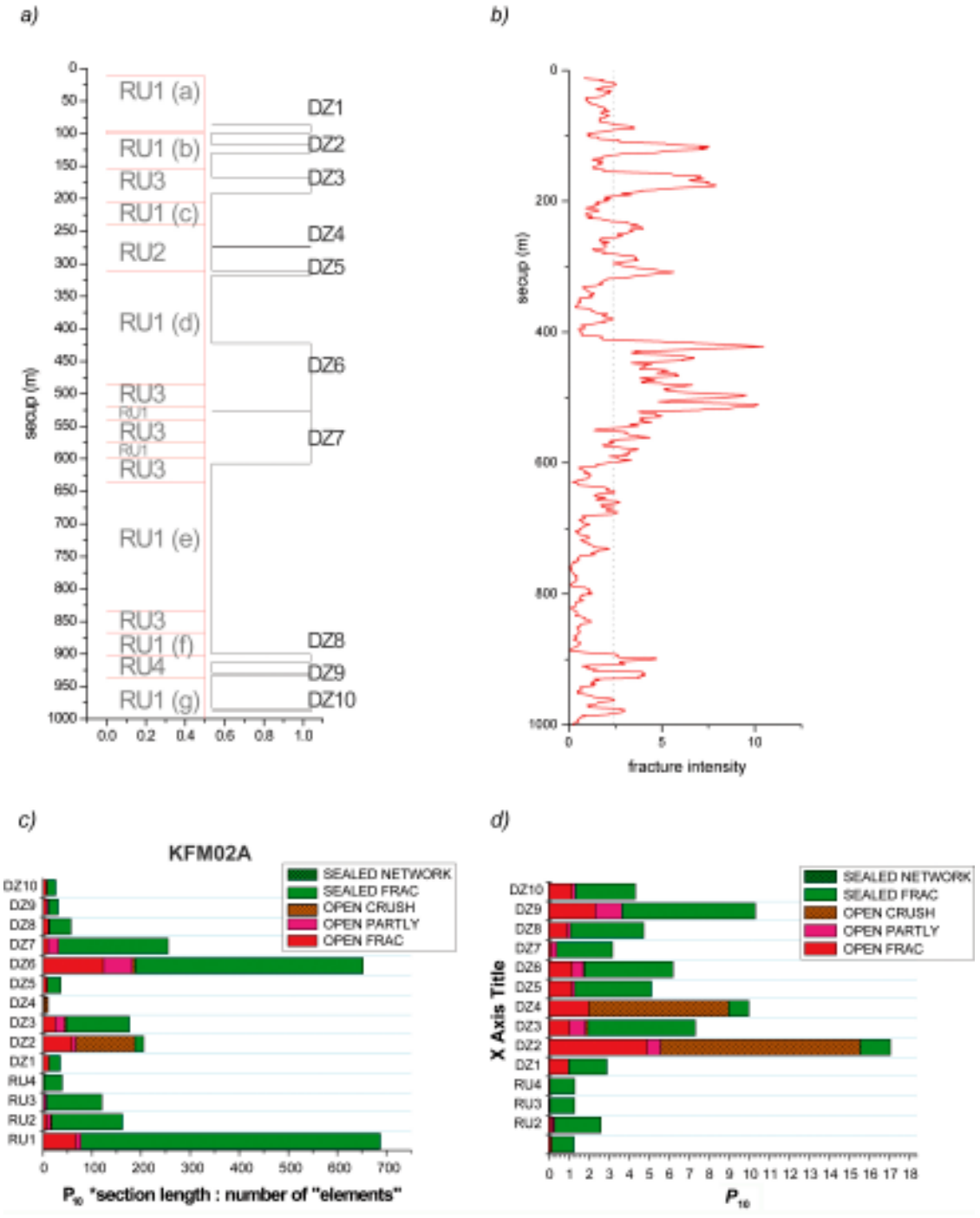

Figure 6-16. *Borehole KFM02A, (a) RU and DZ definition from p_one_hole_interpret. (b) fracture intensity (P_{10} smoothed by adjacent averaging n=10) along the borehole (fracture=open+partly open+sealed). (mean represented as a dashed grey line). (c and d) relative proportion of the different "type" of fractures for the RU and DZ zones.*

An insight of the fracture orientation distribution is provided through the stereoplots – (Schmidt projections) of the fracture poles belonging to the DZ (Figure 6-17a) and to the RU (Figure 6-17b). This illustrates again at the orientation level, the high variability associated to the fracturing.

Finally, even within a single Rock Unit, variability is present. The fracture intensity decreases slightly with depth, as illustrated by the values of fracture intensity within the RU1 of KFM02A (Figure 6-18, RU1 subsets defined in Figure 6-16, RU1a is the most superficial and RU1g the deepest). The trend is visible for the sealed, open and partly opened fractures. However, the decrease is less than the internal variability (Figure 6-18b).

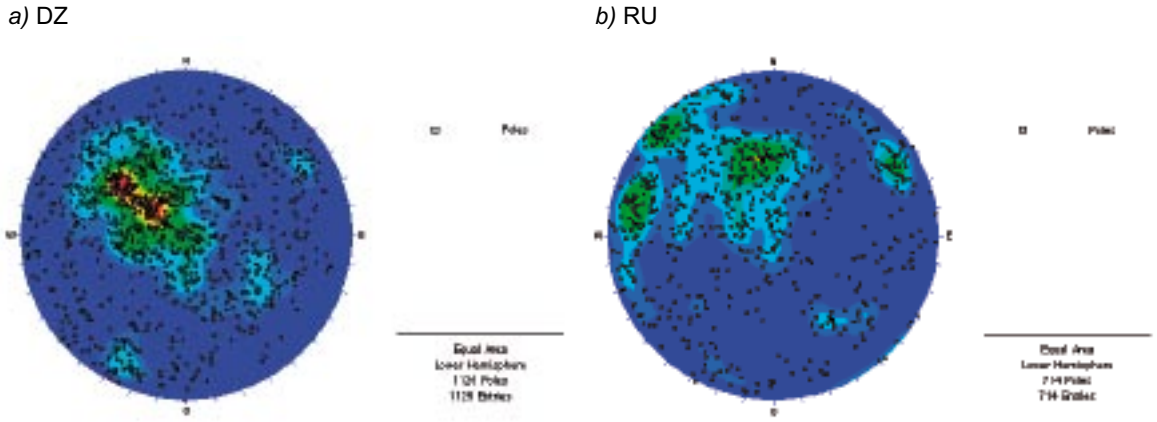

Figure 6-17. *KFM02A, stereoplots (Schmidt projections, not corrected), a)fractures from Deformation zones and b) fractures from Rock Units.*

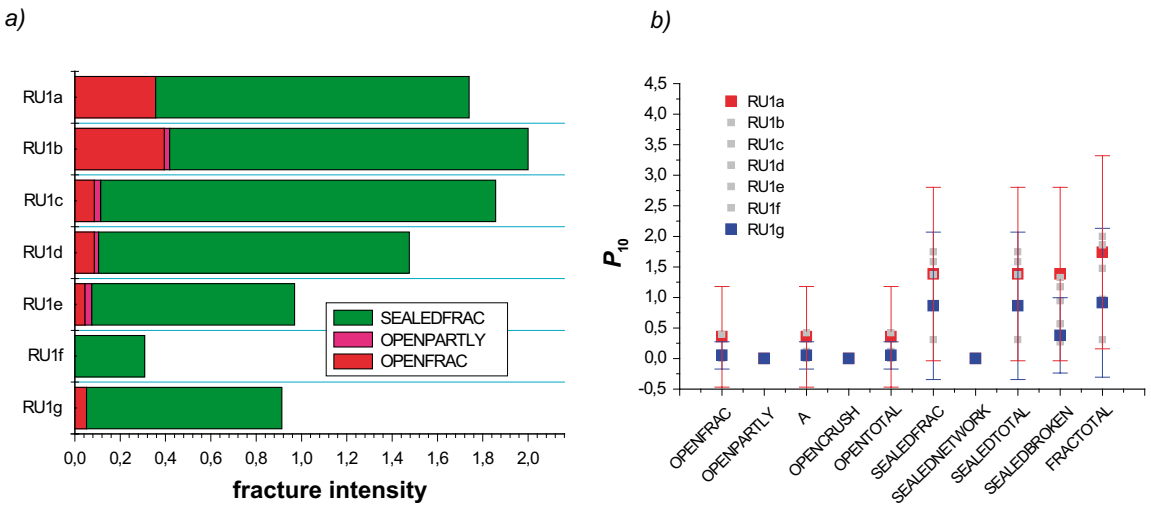

Figure 6-18. *Borehole KFM2A. Fracture intensity variations within a single rock unit, RU1. Subsets RU1a down to RU1g are defined toward increasing depth. a) mean fracture intensity, b) mean plus standard deviation.*

Borehole KFM05A

KFM05A is an inclined borehole with a mean trend and plunge of 90° and 60° respectively (Table 5-9 in /R-05-18/). The total borehole length is about 1,000 meters, sampled between an elevation of –82 meters down to –822 meters.

On average, the fracture intensity (on individualized fractures) along KFM05A (RU and DZ together) is equal to **3.2**. When only the RU are counted, the average fracture intensity is reduced to **2.0** (see Table 6-7). In both cases the associated standard deviations are above the mean values, thus reflecting a high variability. If every type of fracturing is counted (individualized fractures plus crush and sealed networks) to estimate the fracture intensity, a value of **5.2** is reached. Although we do not discriminate here between the open and sealed fractures, we notice that individualized fractures are dominated by the sealed fractures (green bars to be compared to red and magenta bars in Figure 6-19b and c). In addition, borehole KFM05A contains a significant amount of sealed network fracturing (see also Section 7.3.2) and a few crush zones.

The fracture intensity high variability is furthermore illustrated through the subdivision of this borehole in a few RU and DZ (Figure 6-19a), and through the variations of fracture intensity (Figure 6-19b). The variability observed here is only partly reflected in the fractal dimension measured closed to 0.9 (Section 6.4.3). The geological complexity and the variations in intensity observed from one RU (and DZ) to the other are displayed Figure 6-19c and d.

An insight of the fracture orientation distribution is provided through the representation of stereoplots of the fracture poles belonging to the DZ (Figure 6-17a) and to the RU (Figure 6-17b). Both distributions display similar characteristics with 3 apparent peaks of intensities, two subvertical ones and one horizontal.

Finally, even within a single Rock Unit, variability is present. Here the mean fracture intensity increases slightly with depth, as illustrated by the values of fracture intensity within the RU2 zones of KFM05A (Figure 6-21, RU2 subsets defined in Figure 6-19, RU1a is the most superficial from an elevation equal –240 m down to –292 m, and RU1c the deepest one, from elevation –597 m down to –738 m). The trend in fracture intensity is observed for the individualized fractures and for the sealed network fracturing, whereas the intensity of open fractures remains constant.

Conclusion

The preceding descriptive analyses demonstrate the complexity of interpretation for even a single borehole. Moreover, the intercomparison between boreholes becomes straightaway highly thoughtful since it requires the further inference of a 3D model coupling both orientation and apparent fracture intensity. Therefore additional interpretations regarding in depth fracturing are directly moved through the calculation of $\alpha_{3d}(\varphi)$ in the next chapter.

Table 6-7. Fracture intensities (from individualized fractures) measured on FKM05A.

KFMO5A	Size	$<P_{10}>$	Sdv
ALL (RU+DZ)	[1:898]	3.2	3.5
RU	[1:622]	2.0	2.6

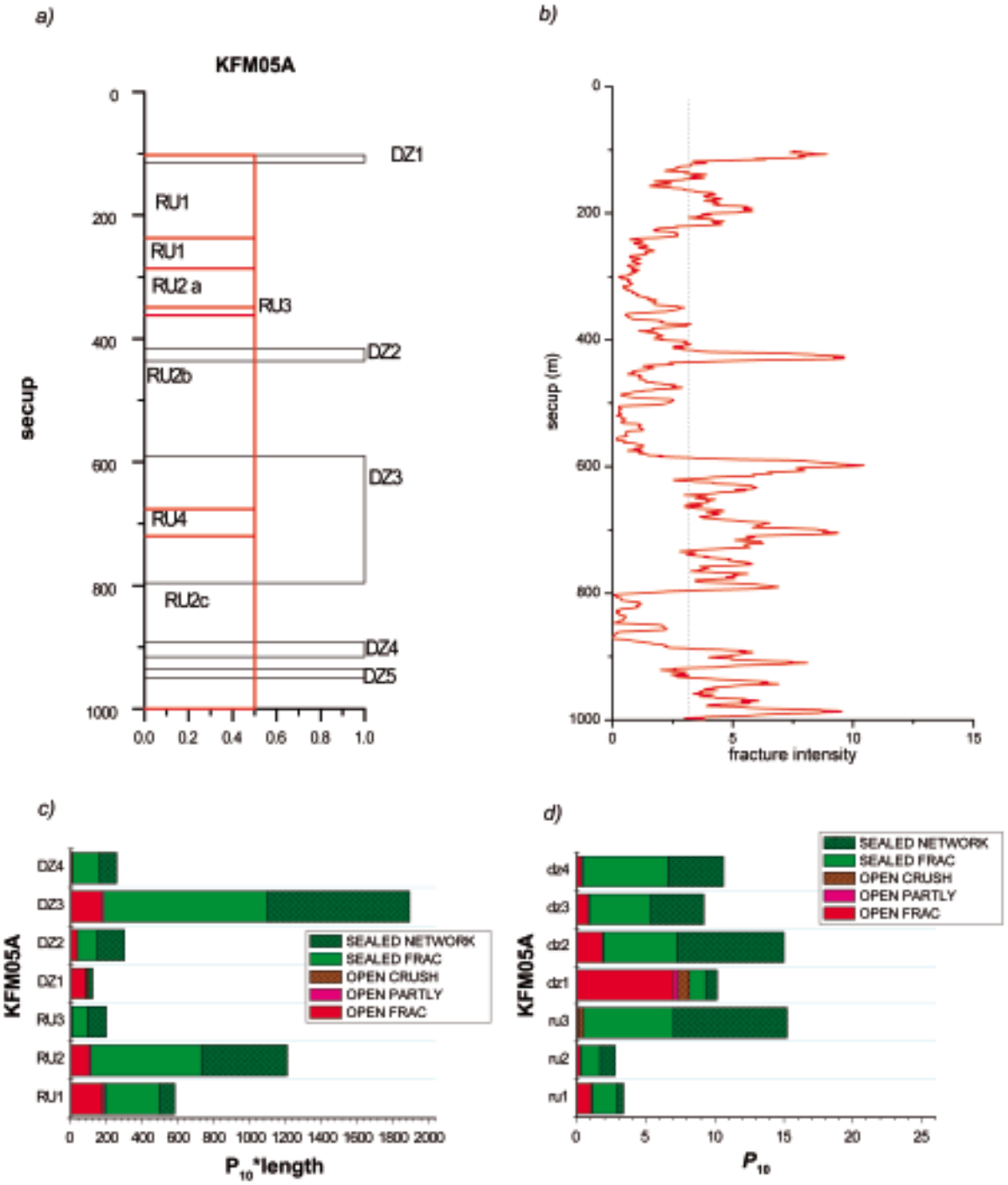

Figure 6-19. *KFM05A, (left) RU and DZ definition from p_one_hole_interpret. (right, top and bottom)relative proportion of the different "type" of fractures for the Rock Units and Deformation zones. c) and d) fracture intensity (P_{10} smoothed by adjacent averaging n=10) along the borehole (fracture=open+partly open+sealed), (mean represented as a dashed grey line).*

a) KFM05A-DZ *b)* KFM05A-RU

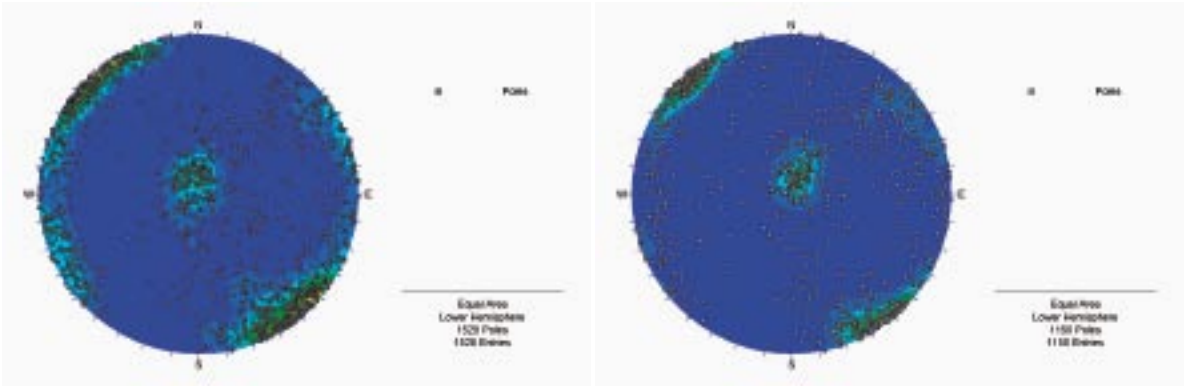

Figure 6-20. *KFM05A, stereoplots (Schmidt projection, not corrected from orientation bias) a) RU and b) DZ.*

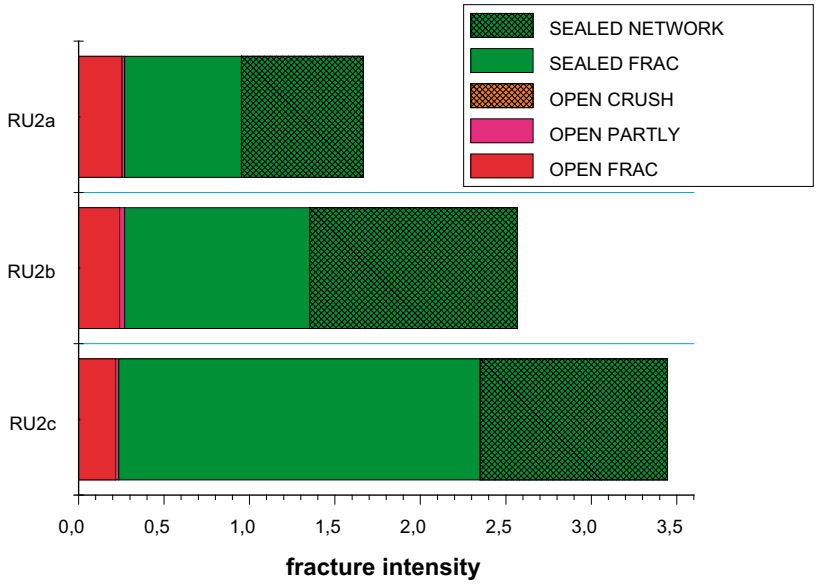

Figure 6-21. *KFM05A, internal variability within the RU2 at different depths.*

7 The scaling model(s)

The general framework within which the scaling model is defined is recalled in Section 3. In the following, we first define the theory and methodology required to assess a sound comparison between data taken at different scales, with different techniques. Then we discuss the likelihood scaling models that are consistent with data, and we perform an analysis of these scaling models in terms of data consistency and potential geological controls. We end up with a discussion on some peculiar fracturing zones that are the crush zones and the sealed networks.

7.1 Theory and methodology

The scaling DFN model has been defined in Sections 3 and 4. We recall the main assumptions:

- The main parameters of the DFN model are the fracture size, and fracture orientations. In the absence of information about fracture shape, a disk shape is assumed. Note that any polygonal or elliptic shapes would give similar results, as long as the anisotropy in the fracture-plane shape remains small.
- Length and orientations are assumed to be independent parameters, meaning that small and large fractures should have similar orientation distributions. Testing this assumption requires a large number of data. The simplest method would consist in dividing the orientations into several classes, and in analysing the length distribution for each class. However the small number of points within each class, as well as the natural variability, make the calculation of a scaling length exponent per class questionable. We thus make the following analysis in the framework of this assumption. We will discuss some elements of consistency when comparing boreholes and outcrops. However we recommend to consider the independence assumption as a potential source of uncertainty when using the DFN model.
- At last, we consider that the fracture length distribution can be modelled by a power law, and that the fracture density (number of fractures per unit volume) is scale independent (D_c=3). The latter assumption is consistent with the large correlation dimensions calculated for both outcrops, boreholes, and lineaments. The differences with the constant-density model (fractal dimension of 1.9 in 2D or 0.9 in 1d) are not statistically demonstrated, and anyway lead to differences in fracture density much smaller than the other sources of uncertainty or variability.

With these assumptions, the general scaling model is thus (see Equation 4-2):

$n_{3d}(l, \theta, \varphi) = \alpha_{3d}(\theta, \varphi)\, l^{-a_{3d}}$.

The power-law exponent a_{3d} contains the scaling information. It is critical because fracture densities extrapolated at large scale are highly sensitive to it. The "density" term $\alpha_{3d}(\theta,\varphi)$ is the fracture density for a length l of 1. It is fundamentally related to the scaling exponent a_{3d}, so that it is meaningless to compare two different values of α_{3d} if they have been calculated for two different scaling exponents. On the other hand, $\alpha_{3d}(\theta,\varphi)$ is the only information that can be used for really comparing the consistency of a DFN model with data taken on different places, at different scales. In a sense the fracture network orientation density is used as the "DNA" of a DFN model, and the consistency analysis consists in comparing the DNA of different data.

The method for calculating $\alpha_{3d}(\theta,\varphi)$ and a_{3d} from the outcrop fracture trace maps, and from borehole fracture intensity are developed in Appendix 4 and in /Davy et al. sub/. To be short, the basic equations that we use for calculating α_{3d} are:

$$\alpha_{3d}(\theta,\varphi) = \frac{\alpha_{2d}}{n_{2d}} \frac{2}{\sqrt{\pi}} \frac{\Gamma(\frac{a_{3d}+1}{2})}{\Gamma(\frac{a_{3d}}{2})} \int_t \frac{n_{2d}(t,\theta,\varphi)}{\sin\varphi} dt \qquad \text{Equation 7-1}$$

with t the fracture trace length on outcrops, Γ the gamma function, α_{2d} and d_{2d} the parameters of the 2D power-law fit on fracture traces, such as:

$$n_{2d}(t) = \alpha_{2d} t^{-a_{2d}}$$

and

$$n_{2d} = \alpha_{2d} \int_t t^{-a_{3d}+1} dt$$

For the 1d/3d stereology problem, the recorded fractures are those that cross the entire borehole. The classical Terzaghi correction was found not be to valid because of an incorrect consideration of this breaking condition, and of the power-law length distribution (Figure 7-1).

The general expression of the borehole fracturing intensity for a power-law length distribution was calculated from numerical simulations. We found the following expression to be valid up to a_{3d}=5 with an excellent accuracy:

$$n_{1d}(\theta,\varphi) = \alpha_{3d}(\theta,\varphi) \frac{\pi d^{3-a_{3d}}}{2(a_{3d}-3)(a_{3d}-2)(a_{3d}-1)} \cos\varphi^{a_{3d}-2} \left(1 - \frac{3}{38} * (a_{3d}-3) * (7.4-a_{3d}) * (1-\cos\varphi^{a_{3d}-2})\right)$$

where d is the borehole diameter. Note that the classical P_{10} is the integral of n_{1d} over both θ and φ, that is:

$$P_{10} = \int_\theta \int_\varphi n_{1d}(\theta,\varphi) d\theta \cdot d\varphi$$

This expression is valid only if the smallest element of the 3D fracture distribution (l_{min}) is smaller than the borehole diameter d. If not and if l_{min} is larger than $10d$, the classical Terzaghi correction is obtained (see Figure 7-2).

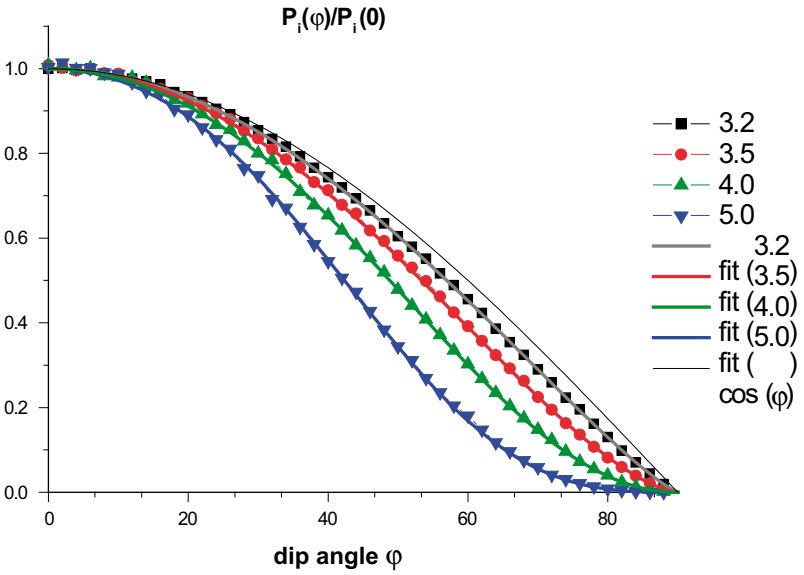

Figure 7-1. *Probability for a fracture of dip φ to intersect a vertical borehole normalized by the same probability for a dip φ=0. The curves are calculated for different values of a_{3d} (see legend). The cos(φ) correction, classically denoted Terzaghi correction, is the thin black line. The colour lines indicate the fit obtained with the equation given below.*

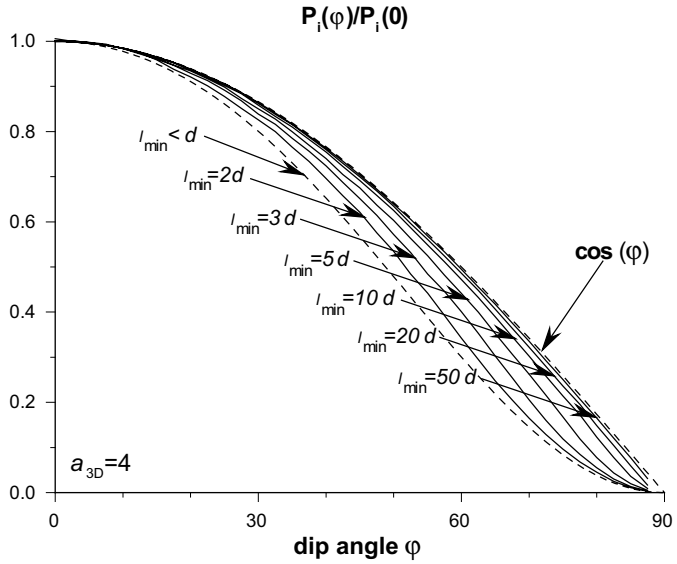

Figure 7-2. *Same legend than Figure 7-1 for a fracture distribution with a power-law length dependency valid down to l_{min}, and l_{min} larger than the borehole diameter d.*

The expression for $l_{\min}$>10d becomes:

$$n_{1d}(\theta,\varphi) = \frac{\pi}{4} \cdot \alpha_{3d}(\theta,\varphi) \cdot l_{\min}^{3-a_{3d}} \cdot \cos\varphi \left(\frac{1}{a_{3d}-3} - \frac{2}{a_{3d}-2}\frac{d}{l_{\min}} + \frac{1}{a_{3d}-1}\left(\frac{d}{l_{\min}}\right)^2 \right)$$

This additional complexity is in fact helpful to address the $l_{\min}$ issue from the stereology analysis.

7.2 Definition of a global scaling model

7.2.1 Data analysis

The Global Scaling Model (GSM) derivation relies on density distribution interpretations. At this stage of the DFN model analysis, borehole data are not integrated since they only sample one scale – the borehole diameter – and thus do not provide any scaling argument about fracture sizes. Moreover the comparison of borehole fracturing intensity and outcrop trace length distribution is model dependent.

The fracture trace-length density distributions have been calculated at ranges of: the outcrop scales (1–10 meters), and the lineament scales (300 m–10 km). Each dataset taken independently can hardly define a valid GSM since it covers a very restrictive range of scales. But linking directly outcrop fractures and lineaments is also debatable: Do these objects, whose geological nature is very different (see discussion in Section 2), belong to the same distribution?

We thus consider two extreme possibilities for the global scaling model (Figure 7-4 and Figure 7-3).

The first GSM represents a kind of synthesis of the information derived from the outcrop datasets. We first put all the related fracture traces together in order to calculate an average density distribution. The resulting curve (Figure 7-3b) displays a slight concave shape in a log-log plot, which means that a single scaling exponent is not well defined. We can not distinguish whether this is due to some finite size effects or to the very nature of fracturing. The central part of the curve is consistent with a length exponent a_{2d} equal to 2.5 (eq. to k_t equal to 1.5).

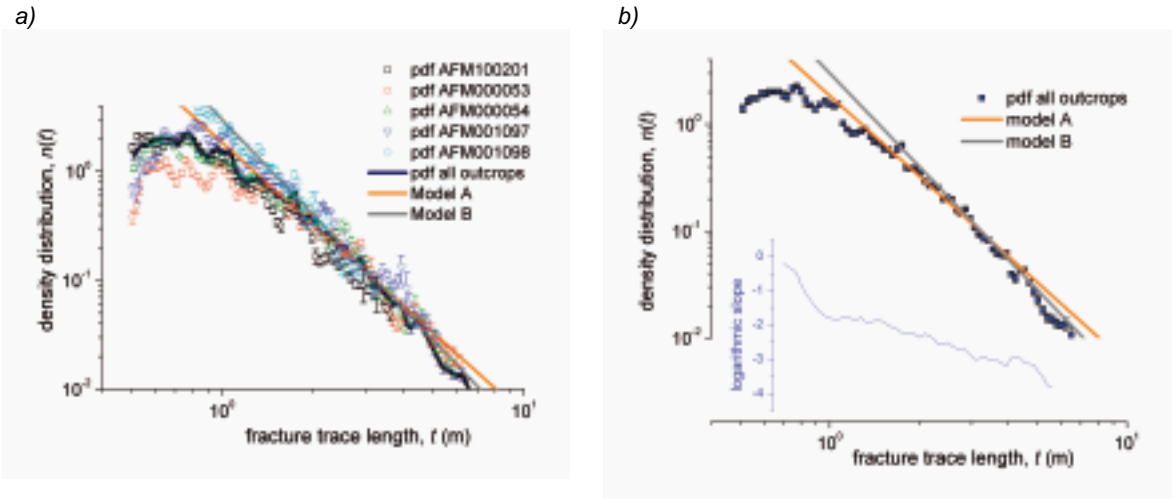

Figure 7-3. *Outcrops density distributions, a) pdf calculated for the five outcrop trace maps separately (symbols), pdf calculated over the sum of the five outcrop datasets (navy line) and the two site models: "model_A" (orange thick straight line) and "model_B" (grey thick line). b) Same figure without the individual pdf curves (plus logarithmic slope as an inlet).*

This value is also consistent with several exponents derived from the local and independent analysis of the different outcrop sets (see Section 6.2.8). We thus decide to take this model as a potential candidate for the GSM, at least representative of the variations observed in the outcrop scale range. In the next paragraph, this model will be called "**model_A**" (see Table 7-1 for a sum up). It overestimates the lineament density, when extrapolated at the kilometer scale, by about one order of magnitude (Figure 7-4 and Figure 7-5d).

The second GSM that we define is based on the assumption that outcrops and lineaments belong to the same distribution (blue straight line in the Figure 7-4). This model has a length exponent a_{2d} equal to 2.9 (eq. to k_t=1.9). It fits the outcrop density distributions for trace lengths larger than about 2 m. Note that this exponent is equal to D_{2d}+1, with D_{2d} the fractal dimension of fracture traces that was found to be 1.9 for most outcrops (also consistent with the correlation dimension of 0.9 measured for boreholes). This model thus leads to a self-similar description of the fracture networks in the sense that derived fracture networks have a look independent of the observation scale. This second GSM model is called Model B in the following.

The model parameters, deduced from data fits, are given in Table 7-1.

Both global models are now applied to each dataset to evaluate the variability in the density term α_{2d} (note that, as mentioned above, it is meaningless to compare α_{2d} for different exponents). For a_{2d}=2.5, α_{2d} varies from 1.26 to 2.17, while a mean value of 1.85 was derived from the mean model (Table 7-2, model reference: "outcrop"). For a_{2d}=2.9, α_{2d} varies between 2.0 and 3.0 (see also Table 7-2, Model B).

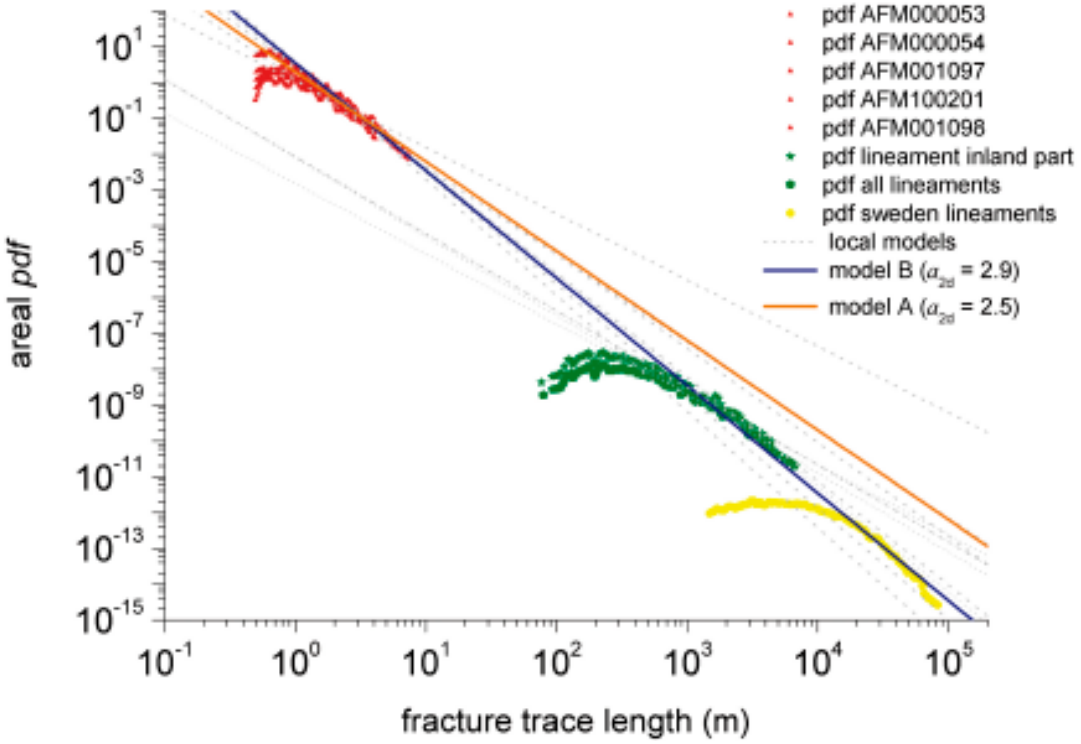

Figure 7-4. *Multiscale pdf distribution, data in symbols, models in straight lines (see inlet legend for details).*

Table 7-1. 2D candidate model parameters.

Model name	a_{2d}	k_t	α_{2d}	D_{2d}	Orientations
Model_A	2.5	1.5	1.85	2.	“outcrops”
Model_B	2.9	1.9	3.	2.	“outcrops”

Table 7-2. 2D models.

Outcrop reference name	Model reference	Exponent a_{2d} (k_t)	Density α_{2d}
AFM000053	model_A	2.5 (1.5)	1.85
AFM000053	Model_B	2.9 (1.9)	3.0
AFM000054	Model_A	2.5 (1.5)	1.85
AFM000054	Model_B	2.9 (1.9)	3.0
AFM100201	Model_A	2.5 (1.5)	1.26
AFM100201	Model_B	2.9 (1.9)	2.0
AFM001097	Model_A	2.5 (1.5)	*2.15*
AFM001097	Model_B	2.9 (1.9)	3.0
AFM001098	Model_A	2.5 (1.5)	2.7
AFM001098	Model_B	2.9 (1.9)	3.0

7.2.2 Numerical illustration

We provide here a simple inference between the 2D GSM model parameters up to the 3D model parameters, through numerical procedures. We note that the complete calculation, integrating both the density and orientation terms, is provided in Section 7.3.

Here we chose to keep the orientation distribution expressed in terms of Fisher distributions (Table 6-3 in Section 6.2.8). Then the 3D density term α_{3d} is simply fitted through numerical simulations, since for a given orientation distribution α_{3d} is simply proportional to α_{2d}. The numerical procedure was already used above for defining the 3D model local_AFM001097 (Section 6.2.6). Results of the numerical simulations are provided in Table 7-3. These results will be compared to the complete calculations of $\alpha_{3d}(\varphi)$.

We recall that the two models considered assume disc-shape fractures in 3D whose length (diameter) and orientations are modelled through the present approach. At that stage, the fractal nature of the fracture system is not handled in the model (although it could) since the fractal dimension measured in 2D corresponds to a weak fractal correlation. As a consequence, one can not expect more, from a simulated DFN, than lengths, orientation and apparent densities aspects.

The two GSM models are generated in 3D and sampled on horizontal ten meter scale and km scale outcrops. The corresponding fracture trace maps are provided in Figure 7-5. For illustration purposes, the outcrop contour of AFM001097 is chosen to represent the ten meter scale (Figure 7-5a and b) and the local and regional model areas are chosen to outline the km scale (Figure 7-5d, e and h). On the figure, the two first columns correspond to the models (leftmost column for Model_A, middle column for Model_B) and the remaining one (rightmost) to the original data. In addition, each line of the figure corresponds to a scale of observation coupled to a range of scales for the representation of fracture trace lengths: it is obviously impossible to observe at one glance all the fracture traces, from the meter to the km scale.

The first scale of observation is the "outcrop scale" (a, b and c), where fracture traces are represented within the contour of AFM001097, with a minimum trace t_{min} equal to 0.5 m and a maximum trace length simply bounded by the system size. At that scale of observation (see also Figure 7-3), the apparent difference between model_A and model_B above one meter is hardly observable from the simulated trace maps. The variations in fracture trace length proportions (largest versus smallest fractures) is however illustrated further in Figure 7-6.

The second scale of observation corresponds to the local and regional model areas. In Figure 7-5d to f, the minimum trace length represented is set to 2,000 m (representation zoomed over the local model area). As expected from the multiscale pdf distribution (Figure 7-4), one observes that Model A, arising from the single outcrop scale observations, overestimates largely the of the lineament density. Over that range of scales Model B (a_{3d}=3.9, equivalent to k_r=2.9) provides the same trace length distribution than the data. Note that this is simply an illustration of the concordance of data and Model B already provided in the density length analysis (Figure 7-4). Finally, the simulated DFN's are represented at the regional scale, with a minimum trace length set to 500 m, which corresponds roughly to the resolution scale declared for the lineament data analyses. Model A (Figure 7-5g) is simply not provided because of the limit of representation possibilities. Model B seems to over predict slightly the fracture density; this is simply due to the larger amount of traces, in the model by comparison to the dataset, below the kilometer scale. Whether this discrepancy is due to a resolution effect inherent to the lineament dataset analysis or to a limit of the fracture concept, or a limit of the power law model, remains an issue that could not be assessed within the project.

Table 7-3. 3D candidate model parameters.

	a_{3d}	α_{3d}	D_{3d}	Orientations
Model_A	3.5	3.2	3.	"outcrops"
Model_B	3.9	5.4	3.	"outcrops"

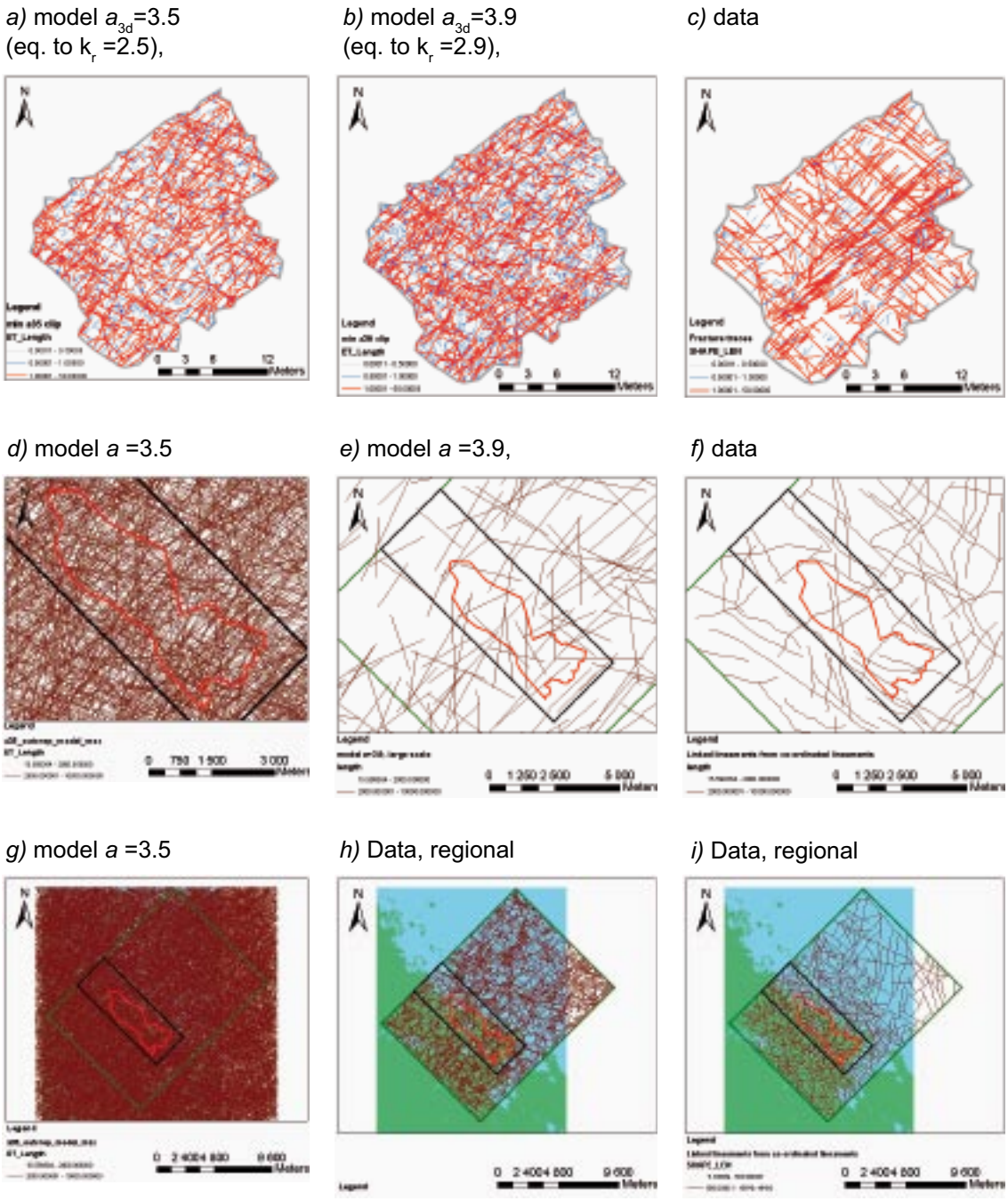

Figure 7-5. *Simulated fracture trace maps from 2D-3d candidate models: model A in leftmost column and Model B in middle column. Corresponding data in rightmost column. From top to bottom the scale of observation and the minimum fracture trace t_{min} increases.*

From the preceding illustration (Figure 7-5) the apparent difference between Model A and Model B is hardly discernable towards the outcrop scale (Figure 7-5a and b). However, based on the model equations in Section 4.1, the number of fracture traces whose length is larger than 10 meters varies roughly of a factor two between Model A and Model B. This is simply illustrated in the following Figure 7-6. The fracture trace maps correspond to the same realisation as in Figure 7-5, but they are displayed within a square area of side 50 m. Fractures whose trace is larger than 10 m together with fractures whose trace is smaller than one meter (with a parent fracture diameter larger than 0.5 m) are represented by red and black lines respectively. As expected, the number of traces larger than 10 increases of a factor close to two from Model B to Model A. Also, the proportion of smallest fractures (red lines) decreases from Model B to Model A.

Finally we provide simulations, for the two GSM models, of the fracture intensity measured along km-long boreholes. The bulk DFN model is sampled along boreholes that have exactly the size and shape of real cored-boreholes of the site. For doing this, a kilometric cube of generation is defined. Then a borehole is placed at the cube center. Two boreholes are considered: a copy of KFM02A and a copy of KFM05A. The numerical boreholes mimic exactly the real borehole shape (radius and local deviations). Fractures of the DFN are generated from a minimum scale equal to the borehole diameter and without a limit towards largest scales. During the simulation process, fractures fully intersecting the boreholes are identified and their characteristics (size, center position, orientation), as long as the position (secup and elevation) on the borehole, are registered.

The method of generation is adapted in order to avoid huge computation times and memory requirements, due to the wide range of scales modelled (from the borehole diameter up to the lineament scale within a kilometric space): instead of initially generating the DFN and next detecting the fractures intersecting a given sample (plane, borehole), the fracture generation and sampling are performed simultaneously; by doing this, only the fractures intersecting the sample are kept in memory. Secondly, the region of generation is adapted to the fracture range of size; by doing this, one avoids generating cm scale fractures hundreds of meters away from

a) Model A (a_{3d}=3.5 eq. to k_r=2.5), *b)* Model B (a_{3d}=3.9 eq. to k_r=2.5)

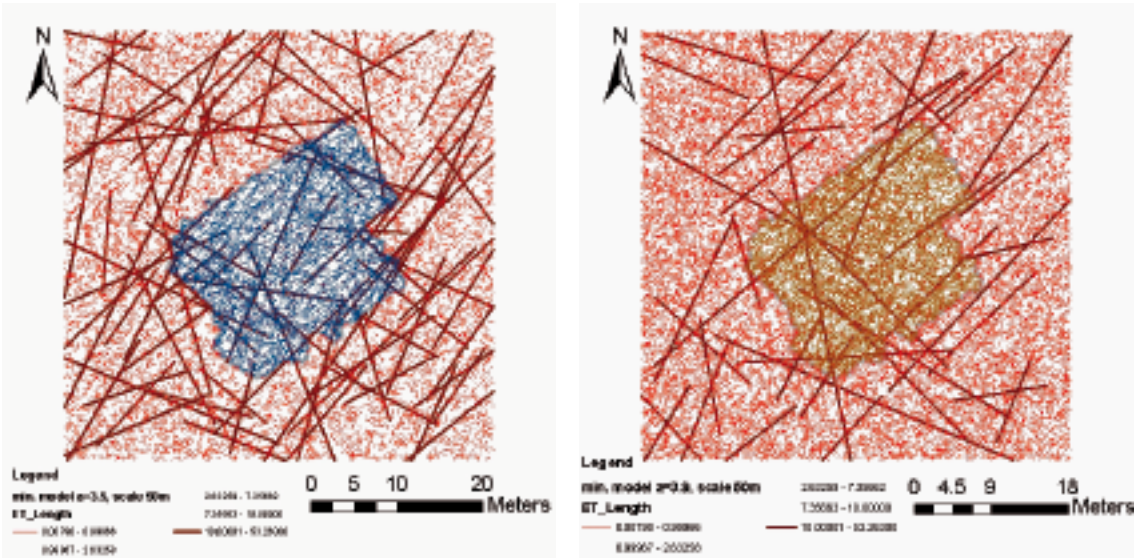

Figure 7-6. *Complement to Figure 7-5, fracture trace map observed in a fifty meters squared area, resulting from a 3D parent fracture model with minimum fracture radius set to 0.25 m (diameter 0.5 m), for Model A (a) and model B (b).*

the sampling object. These adaptations allow to simulate the DFN dynamics through several scales, which is essential when dealing with borehole data whose characteristic lengths go from the borehole diameter (less than 10 cm) up to the borehole length (that reaches one kilometer for the cored boreholes).

From the simulations (Figure 7-7) we observe that:

- the 2D-3d DFN model overestimates up to a factor of two the mean value of P_{10}; the amount of horizontal fractures seems to be large,
- model B leads to a larger fracture intensity than the "outcrop" model,
- the fracture intensity is larger on borehole KFM05A than for KFM02A,
- the fracture intensity variability is weak since no spatial correlation is included at that stage in the modelling.

a) borehole equivalent to KFM05A

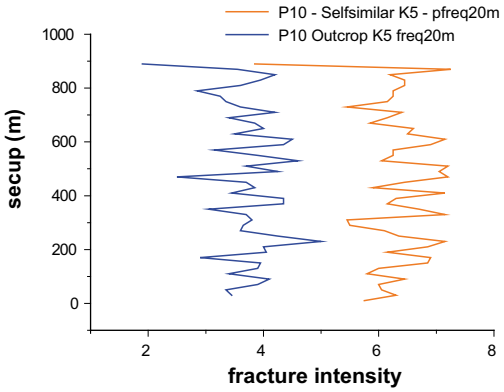

b) borehole equivalent to KFM02A

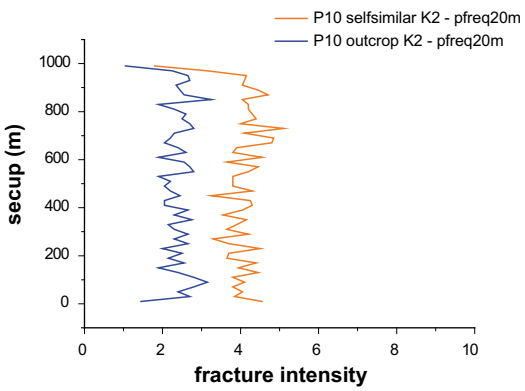

c) borehole equivalent to KFM05A

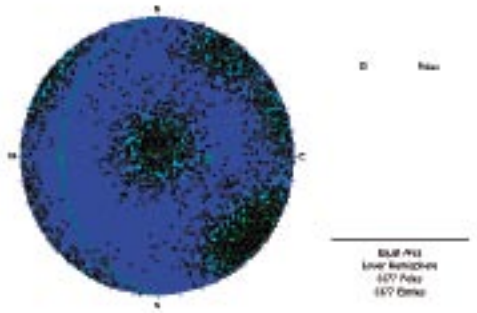

d) borehole equivalent to KFM02A

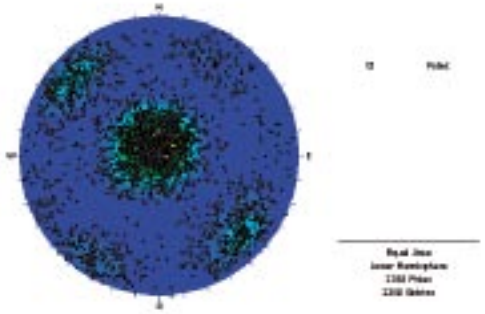

Figure 7-7. *Simulations of the 2D-3d model on boreholes equivalent to KFM05A and KFM02A. (Great circle in c) shows the range of fracture poles perpendicular to the borehole mean orientation; this represents the poles that can not be sampled by the borehole).*

7.3 Consistency analysis

As stated before, the model consistency is assessed by comparing the α_{3d} values calculated from the borehole fracturing intensity and from the outcrop fracture trace maps. We check α_{3d} for both different values of a_{3d} that have been defined in the previous paragraph: a_{3d}=3.5 (k_r=2.5) and a_{3d}=3.9 (k_r=2.9).

We analyse the only dependency with fracture dip: $\alpha_{3d}(\varphi)$, which is calculated by integrating over strike θ. A detailed analysis on both θ and φ would have required a very large dataset – that we do not have – in order to get a decent level of statistical relevance. The fracture dip is anyway a key parameter when calculating α_{3d} since it controls the intersection probability with horizontal plane and vertical boreholes.

Figure 7-8 shows the 3D density terms calculated by two different methods. The difference between both methods illustrates the data variability and the related statistical issues. As for the next figures (Figure 7-8, Figure 7-10, Figure 7-11, Figure 7-13 and Figure 7-14), α_{3d} is plotted with a log scale, which make possible the comparison of large and small values. The uncertainty on α_{3d} depends on the dip value: subhorizontal fractures (small φ) are badly sampled on horizontal outcrops, which explains why the uncertainty on α_{3d} is so large for the first two points on the left of the figure. The uncertainty also depends on the number of fractures over which α_{3d} is calculated. There also exists an horizontal error bar, which is about the uncertainty on the dip measurement (± 5°).

The density term α_{3d} was first calculated for the different outcrops by applying the stereological rules defined in Section 7.1, and by using the 2D fit parameters defined in the previous Section 7.2 in Table 7-3. Figure 7-9 gives values of α_{3d} integrated over the whole range of fracture orientations. Densities varying between 2.1 and 4.35 were obtained for Model A (derived from the sole outcrop trace maps), and between 3.6 and 5.5 for Model B (close to self-similar). These values are fully compatible with the α_{3d} values calculated from the numerical modelling performed independently (Section 7.2.2).

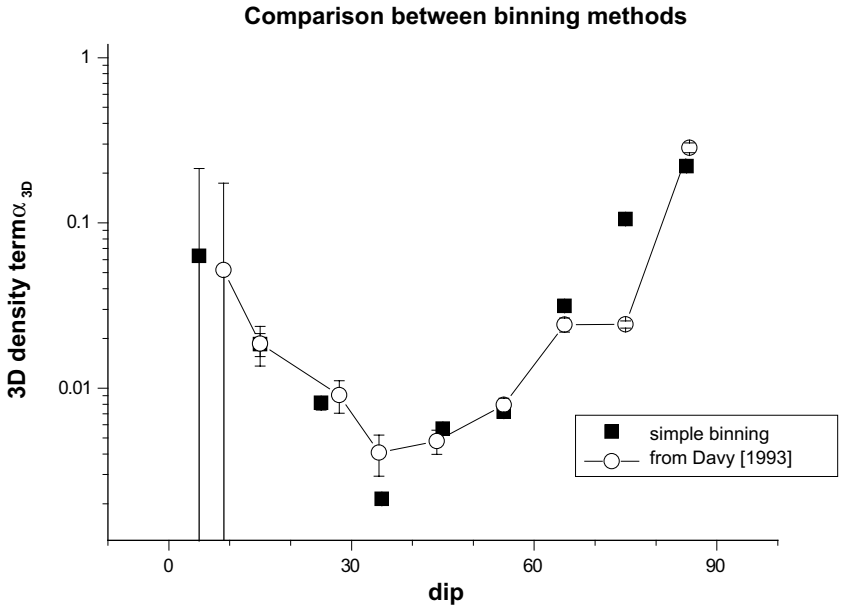

Figure 7-8. *The 3D fracture density term α_{3d} calculated for the outcrop AFM0010098 with two different methods. The first one is based on a simple logarithmic binning; the second one is derived from /Davy 1993/, which ensures a sufficient number of elements for each dip value.*

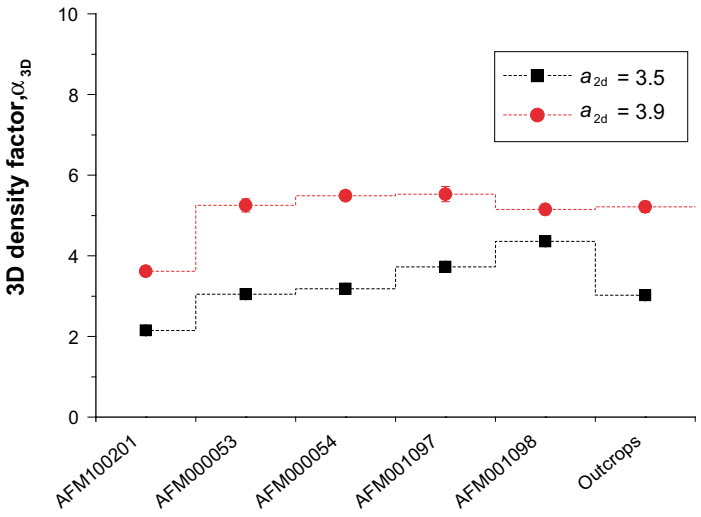

Figure 7-9. *α_{3d} calculated for each outcrop trace map and for the two candidate models, model A (a_{3d}=3.5, or k_r=2.5) and model B (a_{3d}=3.9 or k_r=2.9).*

Variations of $\alpha_{3d}(\varphi)$ with dip is shown in Figure 7-10 for each outcrop and for both GSM models. Most fractures are vertical, but the number of subhorizontal fractures is quite important. The smallest frequency is observed for fractures dipping between 30° and 60°. We note that the error bars increase towards small dips, reflecting the increase of uncertainty due to orientation bias[14] (detailed expression provided in Appendix 1). We observe a remarkable consistency between AFM000053, AFM000054 and AFM001098. AFM001097, the outcrop that corresponds to a shear zone, exhibits small densities in the dip range of 30° to 60°, and quite large densities for subvertical fractures. In AFM10201, the fracture density is more or less constant from 0 to 70°, and increases for vertical fractures.

The "likely" outcrop, where all fracture traces have been put together, is representative of the curve average. It will be taken as an illustrative reference when comparing with boreholes.

Finally, we note that the differences between the two GSM models (a_{3d}=3.5 Figure 7-10 left, and a_{3d}=3.9 Figure 7-10 right) are qualitatively small except for a shift of the curves in proportion to the average α_{3d} values.

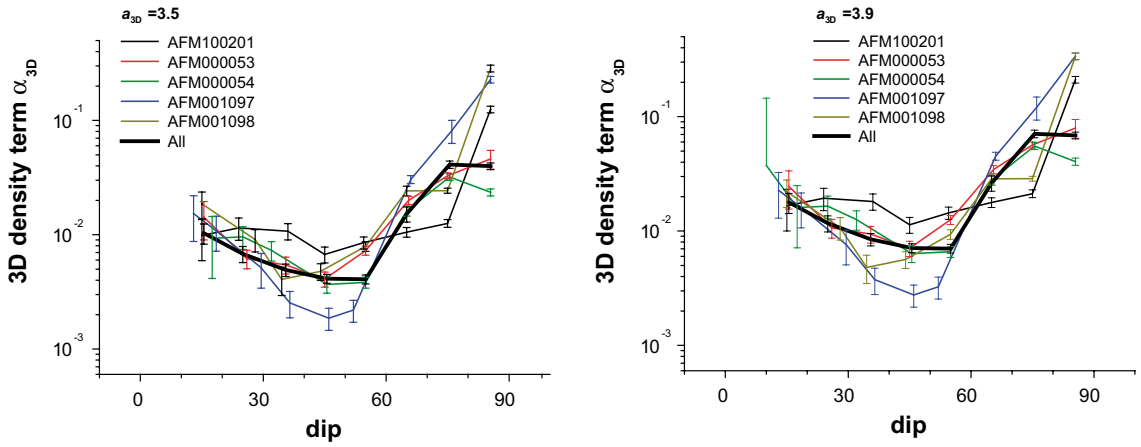

Figure 7-10. *$\alpha_{3d}(\varphi)$ for the five outcrop trace maps. Left Model A (a_{3d}=3.5 eq. to k_r=2.5). Right, "self-similar" model (a_{3d}=3.9 eq. to k_r=2.9).*

[14] On the contrary, errors bars increase towards large dips for vertical boreholes.

We now compare the density term $\alpha_{3d}(\varphi)$ calculated from the 2D outcrop datasets with $\alpha_{3d}(\varphi)$ calculated from boreholes. Borehole KFM02A is investigated in details (Figure 7-11, Figure 7-12 and Figure 7-14); in total, four boreholes have been analysed (Figure 7-13).

First we claim that the calculation of $\alpha_{3d}(\varphi)$ (or $\alpha_{3d}(\theta, \varphi)$) is the only way to compare fracture orientations between boreholes of different orientations, and obviously between boreholes and outcrops. Stereonet representation could be adapted to handle the $\alpha_{3d}(\theta, \varphi)$; however, the representation does not allow superposition of curves that make the interpretation easier (especially when investigated the density variations from horizontal to vertical fractures).

In Figure 7-11, we have analysed the entire borehole KFM02A with either a_{3d}=3.5 (left) or a_{3d}=3.9 (right). We recall that, except in Figure 7-14, $\alpha_{3d}(\varphi)$ is calculated from the entire amount of fractures in the borehole, mixing RU, DZ and different depths.

For each length exponent, two cases are displayed: l_{min} (the smallest fracture length, with $l_{min}=2*r_0$) smaller than the borehole diameter (yellow disks), and l_{min} set to one meter (yellow stars). We observe that l_{min}=1 leads to a systematic overestimation of $\alpha_{3d}(\varphi)$ when compared to the outcrop densities (the grey lines). Model B (a_{3d}=3.9 eq. to k_r=2.9) coupled to no lower limit (yellow disks in Figure 7-11a) seems to fit better the outcrop data, at least for dips larger than 30°.

The 3D density of subhorizontal fractures is larger in outcrops than in boreholes, whatever the GSM model. This is consistent with an increase of the subhorizontal fracturing close to surface /R-05-18/. As a consequence, a DFN model that is constrained only by surface data would produce unrealistically large fracturing intensities along boreholes. This is consistent with the conclusions drawn from numerical simulations (see Section 7.2.2).

Figure 7-12 reproduces exactly Figure 7-11, with a linear vertical axis. This helps to visualise the actual variation of fracture density with dip.

Based on the interpretations related to borehole KFM02A, the 3D density terms $\alpha_{3d}(\varphi)$ were calculated for a few other boreholes: the cored KFM05A (Section 6.4.4), and two percussion drilled boreholes HFM04 and HFM05. Again all depths, RU and DZ were used together.

The main conclusion of the analysis of KFM02A still holds. The subhorizontal fractures are more frequent in outcrops than in boreholes, and the trends are very similar for fractures dipping between 30° and 90°. The only difference is that the outcrop model (model A, a_{3d}=3.5 eq. to k_r=2.5) is now as efficient as model B (a_{3d}=3.9 eq. to k_r=2.9) to ensure the consistency between boreholes and outcrops.

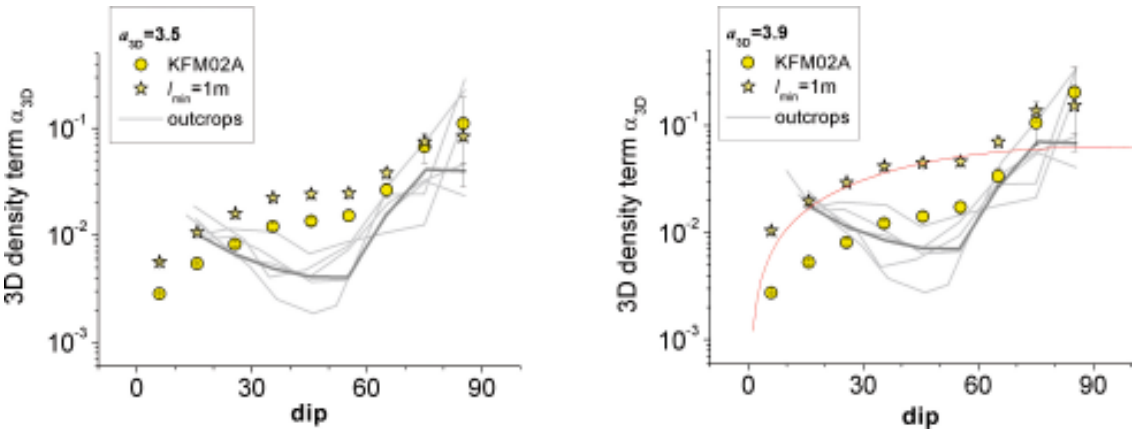

Figure 7-11. *3d density term, $\alpha_{3d}(\varphi)$ for borehole KFM02a, with the two possible models: the "outcrop" model on the left with a_{3d} equal to 3.5, and the "self-similar" model on the right with a_{3d} equal to 3.9. $\alpha_{3d}(\varphi)$ is calculated without limit on l_{min} (yellow disks) and with l_{min} equal to one meter (stars). $\alpha_{3d}(\varphi)$ values calculated from the 2D outcrops are drawn as grey lines, the thickest corresponding to the mean 2D model. The red dashed line corresponds to the homogeneous orientation model.*

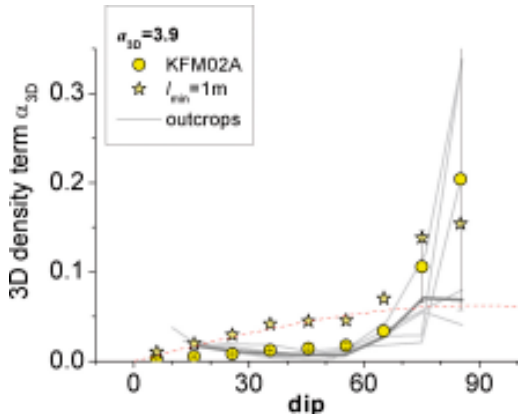

Figure 7-12. *3d density term, $\alpha_{3d}(\varphi)$, same graph as in Figure 7–11a with ordinate axis in linear instead of log.*

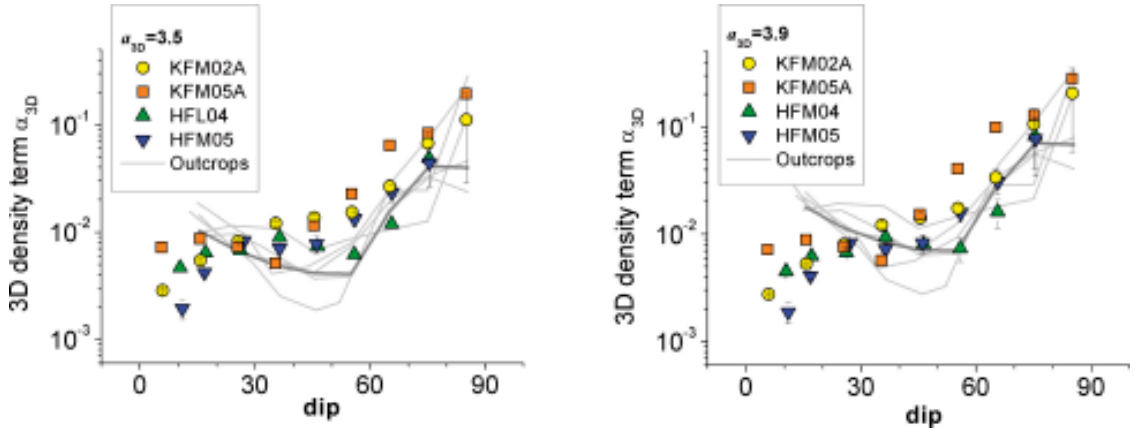

Figure 7-13. *3d density term, $\alpha_{3d}(\varphi)$ for the outcrop model (a_{3d}=3.5, left), and for the self-similar model (a_{3d}=3.9, right) calculated for boreholes KFM02A, KFM05A, HFM04 and HFM05. $\alpha_{3d}(\varphi)$ from 2D datasets are outlined in grey lines.*

Finally, the 3D density terms $\alpha_{3d}(\varphi)$ is calculated within the different rock units and deformation zones defined along the borehole KFM02A (Figure 7-14). The objective is to provide an insight of the possible variations in $\alpha_{3d}(\varphi)$ as a function of geology and depth. We have compared the following zones (see scheme in Figure 6-16): DZ6, DZ7, RU1a, RU1d and RU1e. These units are chosen because they contain enough fractures to derive statistically sound values of $\alpha_{3d}(\varphi)$. In addition, we note that RU1a is located close to the surface; RU1d is located between 300 m (secup) and 400 m, and RU1d between 650 m to 830 m. We first observe, as it could be expected, that the deformation zones are characterized by larger fracture densities than rock units and outcrops. As a consequence, the densities of rock units are smaller than the one calculated for the whole borehole, which is presented in the Figure 7-11. The best-fitting model, that is the model which ensures the best consistency between rock units and outcrop datasets, is now the "outcrop" model, with the exponent a_{3d}=3.5.

Moreover the upper rock unit (red squares in Figure 7-14) shows an increase of the fracture density for subhorizontal fractures, consistent with outcrop fracturing.

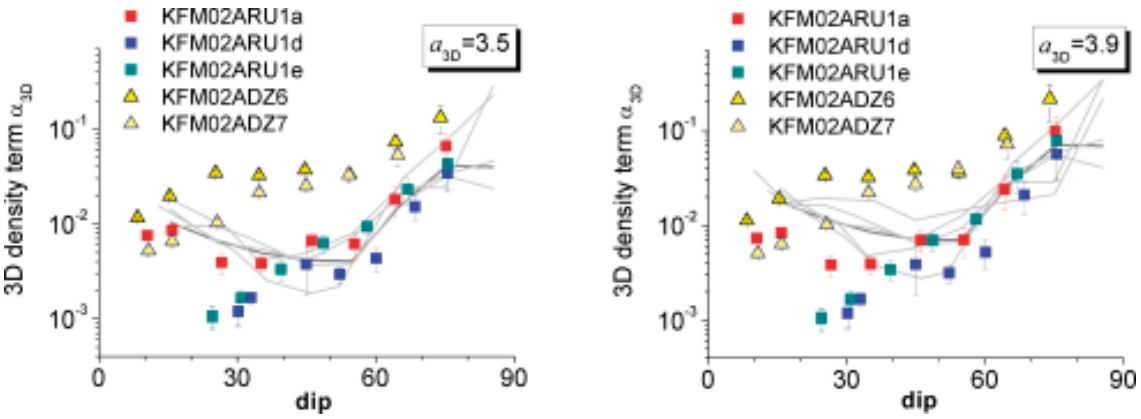

Figure 7-14. *3d density term, $\alpha_{3d}(\varphi)$, recalculated from some subparts of KFM02A: RU1a, RU1d and RU1a=e (coloured squares), DZ6 and DZ7 (yellow triangles). The outcrop models are drawn as grey lines. On the left, α_{3d} is calculated for a_{3d}=3.5, on the right for a_{3d}=3.9.*

From this part, we draw several important conclusions for the general GSM model:

- There exists an important subhorizontal fracturing that occurs close to surface, which makes outcrop fracturing different, in term of density, from the fracturing observed in deep geological units from boreholes. The difference between surface and deep units does not exist for fractures dipping more than 30–40°.
- The rock units are remarkably consistent with outcrops for dips larger than 30–40°, and for the "outcrop" model (a_{3d}=3.5 eq. to k_r=2.5, Figure 7-14). Model B (a_{3d}=3.9 eq. to k_r=2.9, Figure 7-14) tends to predict larger fracture densities in outcrops than in rock units defined in boreholes (in the dip range of 30–40°).
- Fracturing densities from the DZ at depth are larger than fracture densities observed on outcrops: so, there is no equivalent, in the outcrops, of the Deformation Zones, identified at depth.
- The best-fitting model is defined for l_{min} (the smallest fracture length, r_0=l_{min}/2) smaller than the borehole diameter. With this method, it is not possible to say more about l_{min}. Models that consider larger values of l_{min} (1 m for the stars plotted in Figure 7-11) do not ensure the consistency between outcrops and boreholes.

7.3.1 The crush zones

There exists a few crush zones along boreholes that cannot be investigated through our analysis because of the lack of any orientation information. Quantitatively speaking, this missing information is small and should not affect the statistical model. The total number of fractures that are likely to be in crush zones represents 7.5% of the total for KFM02A, and 0.6% for KFM05A (see Table 7-4).

Table 7-4. Number of crush zones and sealed-network zones in the boreholes KFM02A and KFM05A.

	KFM02A	KFM05A
Truly referenced fractures (open and sealed)	1,839	2,678
Crush zones	7	3
Fractures in crush zones	139	16
Sealed network zones	–	~ 50
Fractures in sealed network	–	1,835

These crush zones are more valuable than their statistical occurrence since they may bear a significant part of the flow. Moreover the crush zones may be somewhat representative of the lineaments. By analyzing the occurrence of the crush zones, we may infer the link between boreholes, outcrops and large-scale lineament maps.

An issue is to know if the lineaments belong to the same statistical model as the fractures in boreholes and outcrops. Let us assume that it is true, and that the shear zones represent large structures, whose length is larger than a given value l_{lin} to be determined. The occurrence of these structures is ruled by a probability distribution function, such as (see Equation 3 in /Davy et al. 2006/ above):

$$N_I(l > l_{lin}) \sim h \frac{l_{lin}^{3-a_{3d}}}{a_{3d} - 3}$$

where h is the borehole length. The total number of intersecting fractures is:

$$N_T \sim h \frac{d^{3-a_{3d}}}{a_{3d} - 3} \frac{2}{(a_{3d} - 2)(a_{3d} - 1)}$$

L_{lin} can be derived from the ratio between both numbers:

$$l_{lin} = d \left(\frac{2}{(a_{3d} - 2)(a_{3d} - 1)} \frac{N_T}{N_I} \right)^{\frac{1}{a_{3d}-3}} \qquad \text{Equation 7-2}$$

l_{lin} just depends on a_{3d}, in a way given in the graph below (N_I is given by the number of crush zones and N_T by the number of "truly referenced fractures" in Table 7-4):

With a power-law length exponent a_{3d} of about 3.9 (eq. to k_r=2.9), the minimum length of shear zones is estimated at about 100 m–1 km. If the exponent is smaller, this length becomes very large, up to 10–100 km for a_{3d}=3.5 (eq. to k_r=2.5). This simple analysis gives the conditions for the shear zones to be *statistically consistent* with the rest of the fracture sets. If we assume that the shear zones have the same length as the lineaments, it is not unreasonable to think that their minimum length is about 100 m–1 km, which is consistent with a power-law exponent a_{3d} of about 3.9. This result shows that the conditions for having lineaments consistent with outcrops is the same as that of having shear zones consistent with borehole fractures. This is not really surprising but this was worth checking out.

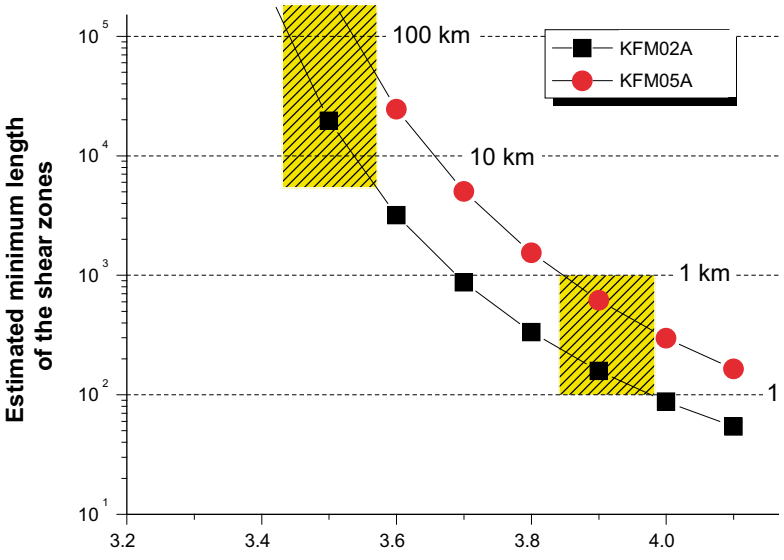

Figure 7-15. *Estimated minimum shear zone length using Equation 7-1.*

7.3.2 Sealed networks

The sealed-network zones are not included in the dataset when calculating the statistical density distribution because no information is provided concerning their orientation.

In KFM05A, there are about 50–700 sealed-network zones (depending on how we define a "zone") with an estimated fracture density of about 2, comparable with the density of the treated fracture dataset.

In fact, "sealed network" is a concept that started to be mapped after the sampling of borehole KFM03A. A sealed network zone has a particular signature with respect to the rest of fracture types identified on boreholes: it consists actually in a very dense cluster of small fractures (high clustering is illustrated in Figure 7-16 below). Due to the high fracture density in a sealed network zone, the characteristics of each "sealed-network fracture" are not registered. Therefore only an estimate of the fracture intensity (P_{10}) is provided for each identified sealed network zone. We suspect that most of these fractures are smaller than the borehole diameter; then, it will be really difficult to perform a comparison between the sealed network fractures and the rest of the fractures, because of the dependence of the fracture density on the smallest recorded fracture length.

The sealed networks are potentially an important (at least worth being considered) part of the fracture system at least for their mechanical consequences. How should the sealed network zone or sealed network fractures be related to the rest of the fracture system (cluster of small fractures, single fracture zone or something in between) remains an issue.

We recommend analysing some of the sealed-network zones in order to understand the geological factors that may control their occurrence, and to quantify their spatial organisation. With the currently available database (fractures lumped in any given sealed network zone), this analysis cannot be done.

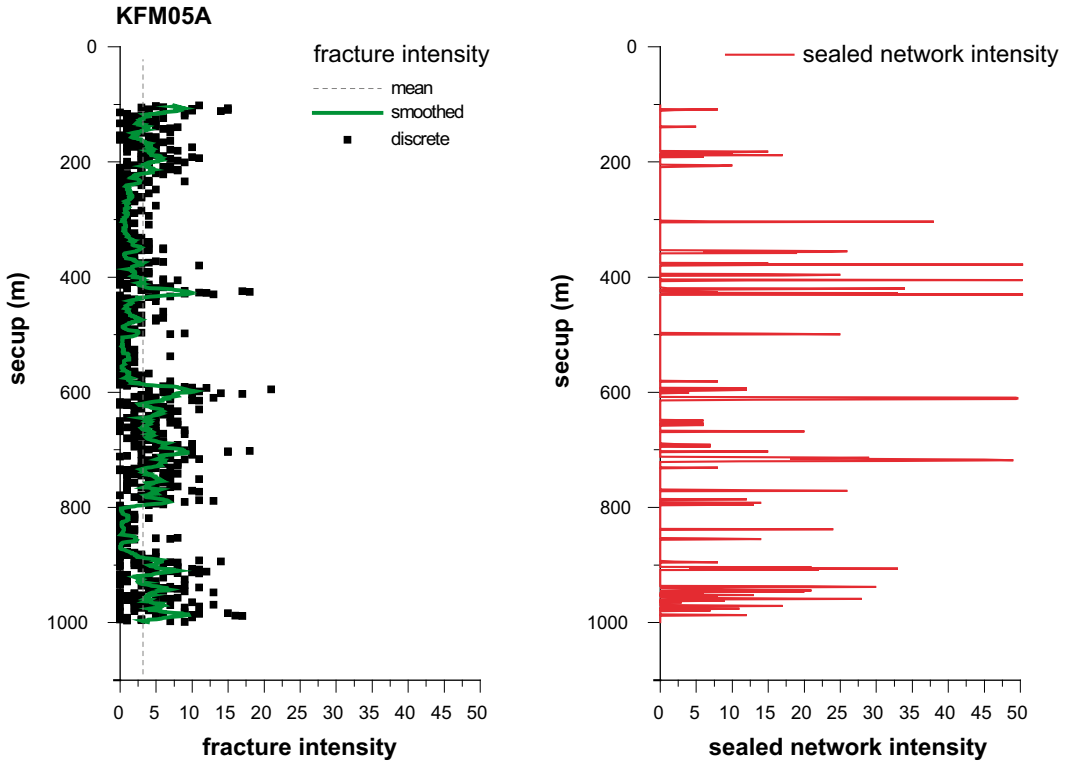

Figure 7-16. *Fracture intensity profile for KFM05A, corresponding to both open and sealed fractures (left) and sealed-network fractures (right). The latter is characterised by locally high densities and strong clustering.*

8 DFN model parameters

Both local (Section 6.2.6) and scaling (Section 7) DFN models have been defined along the report. Given the different variations observed in terms of apparent density, fractal correlation dimension and power-law length exponent, the value of the latter was found to implicate the major source of uncertainty in the DFN modelling process (Figure 8-1, grey) .

Two main candidate models are defined, Model A and Model B, defined by a constant length exponent. Model A refers to the DFN models having a_{3d} equal to 3.5 (eq. to k_r equal to 2.5) and Model B refers to the DFN models having a_{3d} equal to 3.9 (eq. to k_r equal to 2.9). For the two models, the orientation distribution chosen arises from the outcrop datasets (fisher distributions provided in Table 6-3).

Both models were refined to either local constant values of densities (the local models, Figure 7-9) or a mean density, derived from five datasets gathered and combined in the scaling analysis (global models). The different parameters obtained (in terms of a_{3d}, α_{3d} and D_{3d}) are summarized in Table 8-1. the mean fracture density $\alpha_{3d,mean}$ is provided; in complement, the extreme values of fracture densities found from the different datasets (local models), are also provided ($\alpha_{3d,min}$, $\alpha_{3d,max}$). This provides a picture of the DFN model variability (Figure 8-1, inlet, variability around the mean model). The range of validity of the models is discussed in the conclusions (next section).

We note finally that the variability of the DFN models remains obviously lower than the real fracture system; one reason is that fractal correlations are not yet included in the modelling. We think more generally that this issue should be tackled together with the consideration of second order correlations and with the issue of fracture definition with scales.

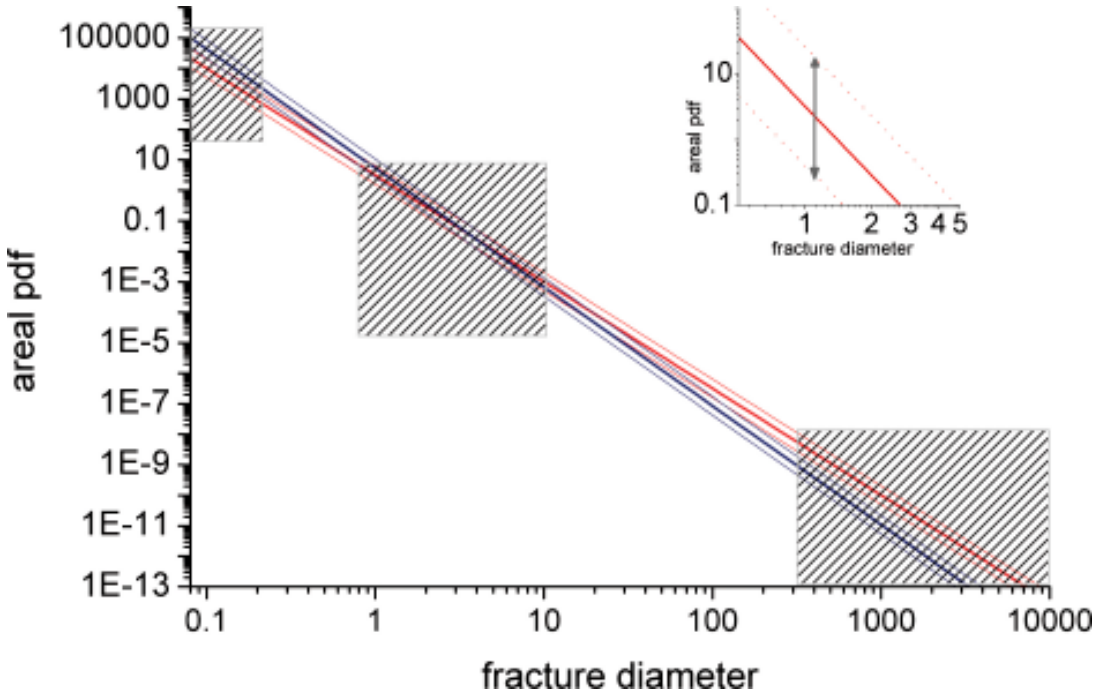

Figure 8-1. *GSM models, the two candidate models, with a_{3d}=3.5 (eq. to k_r = 2.5) in red and a_{3d}=3.9 (eq. to k_r = 2.9) in blue. Dashed zones represent windows of observation. Density variability is illustrated in inlet.*

The smallest fracture (fracture radius r_0 or fracture diameter l_{min}) consistent with the DFN model remains an open question (see the conclusions in next section). We chose therefore to express the results P_{32} like $P_{32}(r_c)$, where r_c is chosen by the user (see Section 4.2.2, Equation 3-2).

The DFN model parameters equivalent to Table 8-1, expressed in terms of k_r and P_{32}, are provided in Table 8-2 below. As expected for power law DFN models dominated by the small scales (a_{3d}>3, eq. to k_r>2), the shorter is r_c, the larger is the density P_{32}. Below a certain scale (r_c) the fracture density measured, P_{32}, is larger for Model B (with k_r=2.9) than for Model A (with k_r=2.5).

Table 8-1. GSM parameters summary (see Table 8-2 for P_{32} and k_r).

	a_{3d}	$\alpha_{3d,mean}$	$\alpha_{3d,min}$	$\alpha_{3d,max}$	D_{3d}	Orientations
Model_A	3.5	3.0	2.1	4.35	3.	Table 6-3
Model_B	3.9	5.2	3.6	5.2	3.	Table 6-3

Table 8-2. GSM parameters summary.

	Model_A	Model_B
k_r	2.5	2.9
D_{3d}	3	3
orientations	Table 6-3	Table 6-3
$P_{32,mean}(r_c=250)$	0.21	0.02
$P_{32,min}(r_c=250)$	0.15	0.01
$P_{32,max}(r_c=250)$	0.31	0.02
$P_{32,mean}(r_c=0.5)$	4.71	4.54
$P_{32,min}(r_c=0.5)$	3.3	3.14
$P_{32,max}(r_c=0.5)$	6.83	4.54
$P_{32,mean}(r_c=0.039)$	17.09	46.14
$P_{32,min}(r_c=0.039)$	11.97	31.95
$P_{32,max}(r_c=0.039)$	24.79	46.14

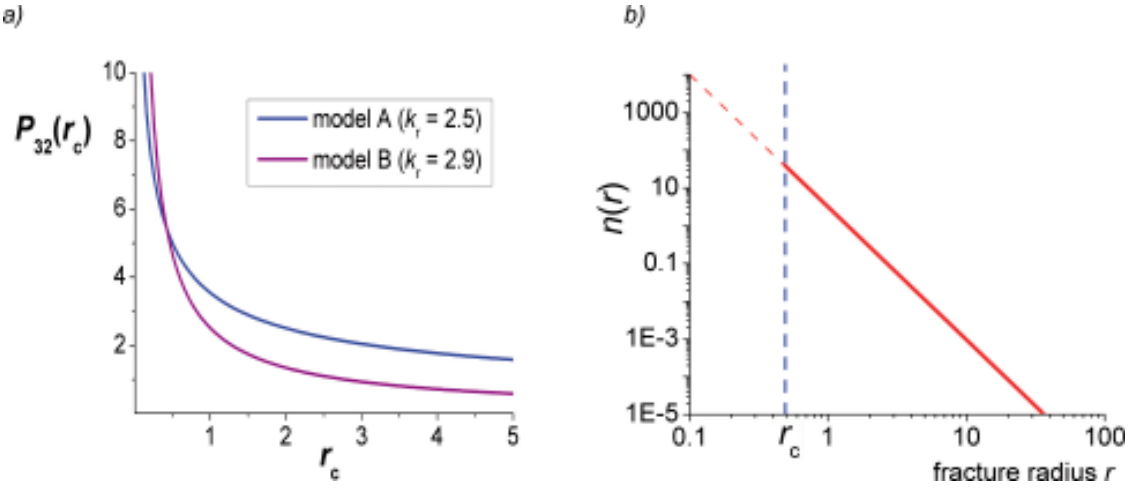

Figure 8-2. *a) Evolution of $P_{32}(r_c)$ for the two mean models: Model A and Model B. b) fracture radius density distribution (red lines), limit r_c symbolized by the blue dashed line.*

9 Conclusions

In this report, we aim at defining a self-consistent method for analysing the fracture patterns from boreholes, outcrops and lineaments. The objective was both to point out some variations in the fracture network parameters, and to define the global scaling fracture models that can encompass all the constraints brought by the different datasets.

From the surface data analyses, we define two possible global scaling models. The first one is consistent with the scaling measured in the outcrops. Its scaling exponent is a_{3d}=3.5 (eq. to k_r=2.5); it overestimates the fracture densities observed in the lineament maps. The second one assumes that both lineaments and outcrops belong to the same distribution model, which entails a scaling exponent a_{3d}=3.9 (eq. to k_r=2.5).

Both models have been tested by looking for the best consistency between boreholes and outcrops in the fracture density-dip relationships. This consistency analysis has been limited to boreholes KFM02A, KFM05A, HFM04 and HFM05. The main conclusions that we draw are the following:

- There exists an important subhorizontal fracturing that occurs close to surface, which makes outcrop fracturing different from the fracturing observed in deep geological units from boreholes. The difference between surface and deep units does not exist for fractures dipping more than 30–40°.
- The rock units are remarkably consistent with outcrops for dips larger than 30–40°, and for the "outcrop" model (model A, a_{3d}=3.5, eq to k_r=2.5, Figure 7-14). The model B (model B, a_{3d}=3.9, eq to k_r=2.9) tends to predict fracture densities larger in outcrops than in rock units defined in boreholes (in the dip range of 30–40°).
- Fracturing densities from the DZ at depth are larger than fracture densities observed on outcrops: so, in that way there is no equivalent in outcrops of the Deformation Zones encountered at depth.
- The best-fitting model is defined for l_{min} (the smallest fracture diameter, l_{min}=2*r_0) smaller than the borehole diameter. With this method, it is not possible to say more about l_{min}. Models that consider larger values of l_{min} (1 m for the stars plotted in Figure 7-11) do not ensure the consistency between outcrops and boreholes.
- The shear zones, as well as the lineaments, may belong to a different global scaling model than rock units. Further investigations and more data are necessary to characterize this additional GSM.

10 Numerical tools

Dips 5.0	
Origin 7.5	
Arcview 9	
Access	
Excel	
3FLO 2.20-002	/Billaux et al. 2005/
Geosciences Rennes Numerical Tools	

11 References

Billaux D, Paris B, Darcel C, 2005. 3FLO Version 2.2 – Calculs d'écoulements et de transport tridimensionnels. ITASCA Consultants internal report, Volumes 1–4.

Bonnet E, Bour O, Odling N, Main I, Davy P, Cowie P, B Berkowitz, 2001. Scaling of Fracture Systems in Geological Media, Reviews of Geophysics, 39, 3, 347–383.

Bour O, Davy P, Darcel C, Odling N, 2002. A statistical scaling model for fracture network geometry, with validation on a multi-scale mapping of a joint network (Hornelen Basin Norway), J. Geophys. Res. 107, 2113, doi: 2001JB000176.

Darcel C, Bour O, Davy P, 2003. Stereological analysis of fractal fracture networks, J. Geophys. Res. Vol. 108, No. B9, 2451, 10.1029/2002JB002091, 30 September 2003.

Darcel C, Davy P, Bour O, De Dreuzy J-R, 2004. Alternative DFN model based on initial site investigations at Simpevarp. SKB R-04-76, Svensk Kärnbränslehantering AB.

Davy P, Sornette A, Sornette D, 1990. Some consequences of a proposed fractal nature of continental faulting, Nature, 348, 56–58.

Davy P, 1993. On the frequency-length distribution of the San Andreas fault system, J. Geophys. Res. 98, 12,141–12,151, 1993.

Davy P, Darcel C, Bour O, Munier R, de Dreuzy J R, 2006. Note on the angular correction applied to fracture intensity profile along a core, submitted to J. Geophys. Res.

Feder J, 1988. Fractals, 283 pp, Plenum, New York.

Gouyet J F, 1992. Physique et structures fractales, Masson.

Grassberger P, Procaccia I, 1983. Measuring the strangeness of strange attractors, Physica, 9, 198–208.

Hentschel H G E, Proccacia I, 1983. The infinite number of generalised dimensions of fractals and strange attractors, Physica 8D, 435–444.

Korvin G, 1992. Fractal models in Earth sciences, Elsevier.

Mandelbrot B B, 1982. The fractal geometry of Nature, 468 pp, W. H. Freeman, New York.

Munier R, 2004. Statistical analysis of fracture data, adapted for modelling Discrete Fracture Networks-Version 2. SKB R-04-66, Svensk Kärnbränslehantering AB.

Piggott A R, 1997. Fractal relations for the diameter and trace length of discshaped fractures, J. Geophys. Res, 102, 18,121–18,125.

SKB, 2004. Preliminary site description. Forsmark area-version 1.1. SKB R-04-15, Svensk Kärnbränslehantering AB.

SKB, 2005. Preliminary site description. Forsmark area-version 1.1. SKB R-05-18, Svensk Kärnbränslehantering AB.

Viseck T, 1992. Fractal growth phenomena, 488 pp, World Scientific, London.

Appendix 1

Fracture trace maps – outcrops

Local analyses

Five fracture trace maps were analysed in the study. Their reference name, area and number of traces are recalled in the table below; their location within the site are recalled in Figure A1-1. In the next pages a descriptive representation of the corresponding data is provided with:

a) trace map together with geological characteristic,

b) a picture of the outcrop or close to the outcrop,

c) a graph corresponding to the density-length distribution (power-law exponent a_{2d}),

d) a graph corresponding to the integral of correlation calculation (fractal dimension D_c),

e) discrete stereonet (lower hemisphere equal area projection),

f) contoured stereonet (lower hemisphere equal area projection).

Table A1-1.

Outcrop	Outcrop area	L ($\sqrt{area}$)	Number of fractures
AFM000053	645.5	25.4	986
AFM000054	596.1	24.4	1235
AFM001097	486.7	22.1	1197
AFM100201	501.2	22.4	1280
AFM001098	279.9	16.7	1201

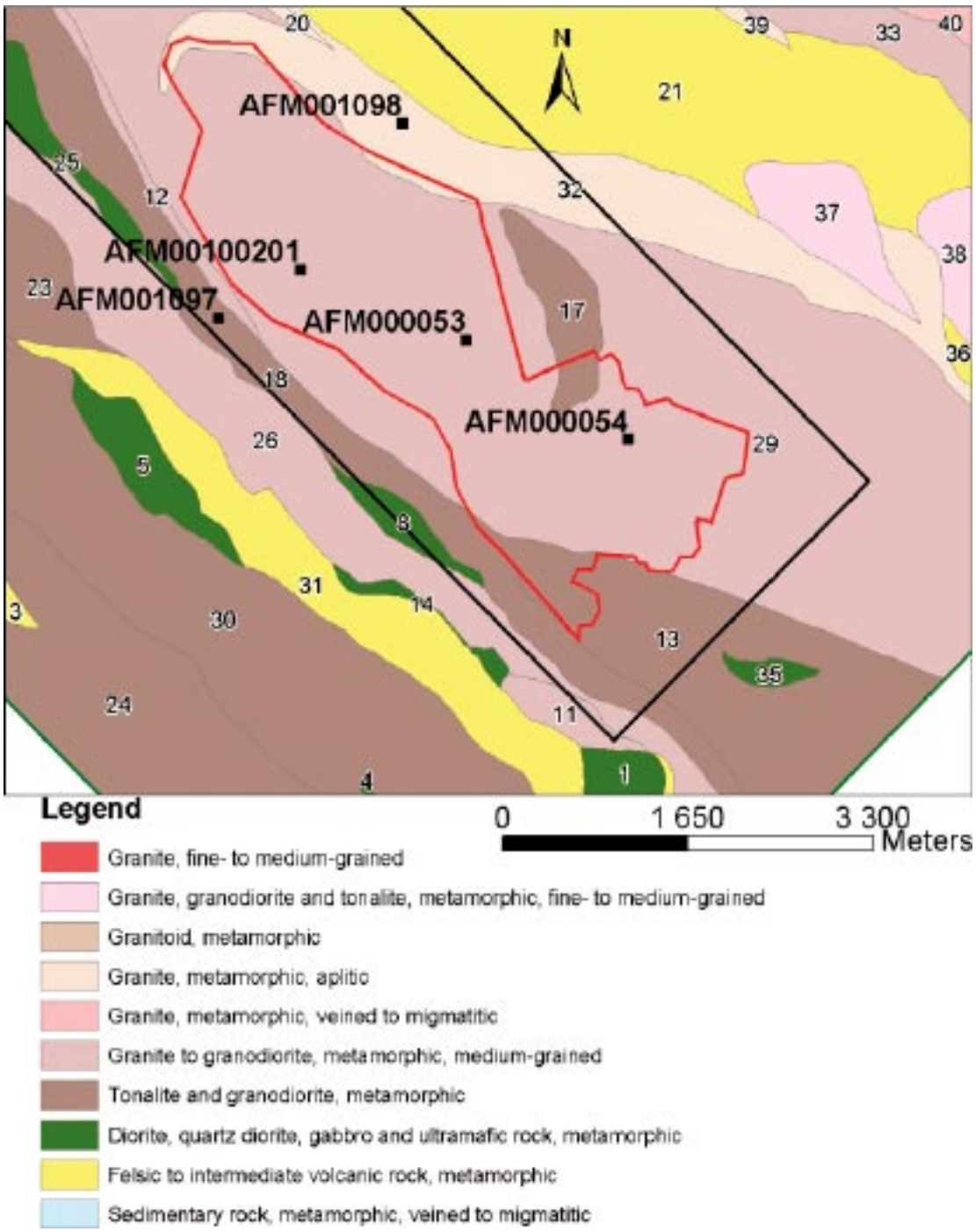

Figure A1-1. *Location of the five outcrops within the site (numbers indicate the rock domains).*

AFM000053

a)

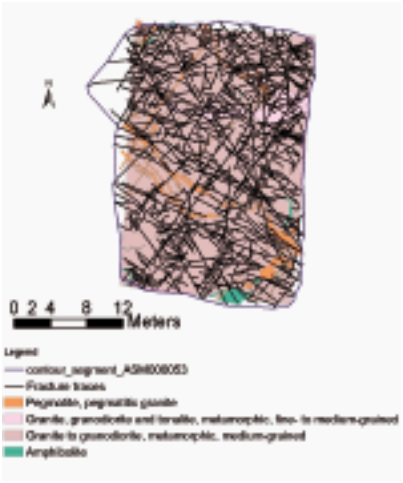

b)

c)

d)

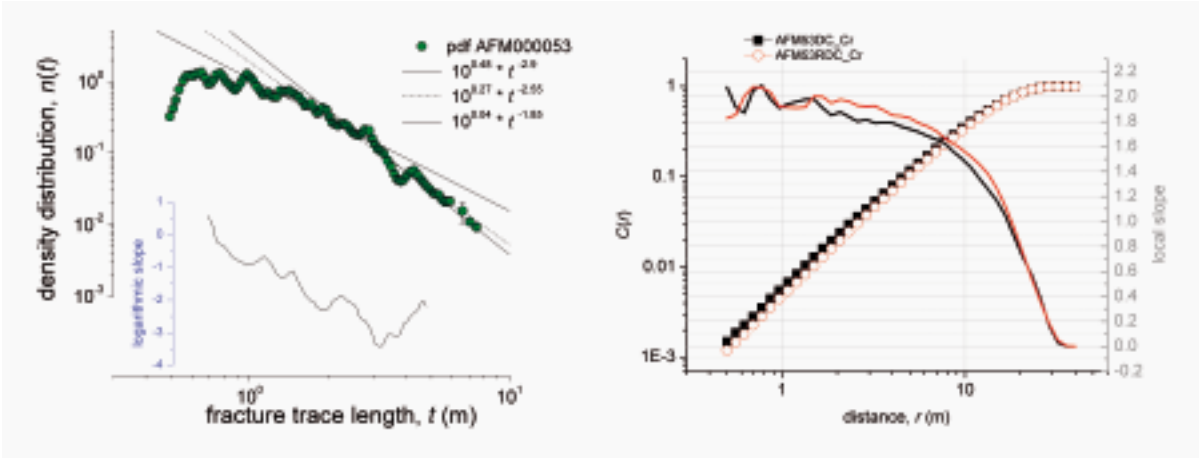

e)

f)

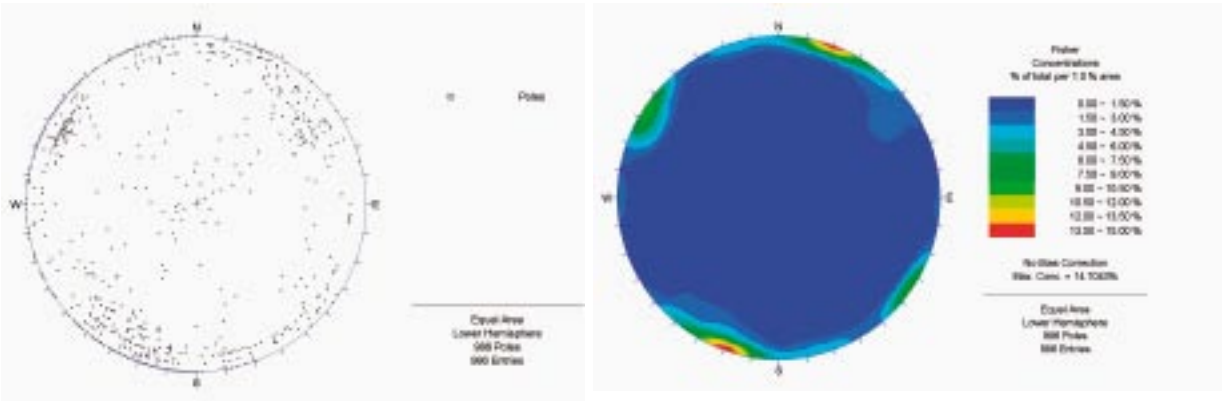

AFM000054

a)

b)

c)

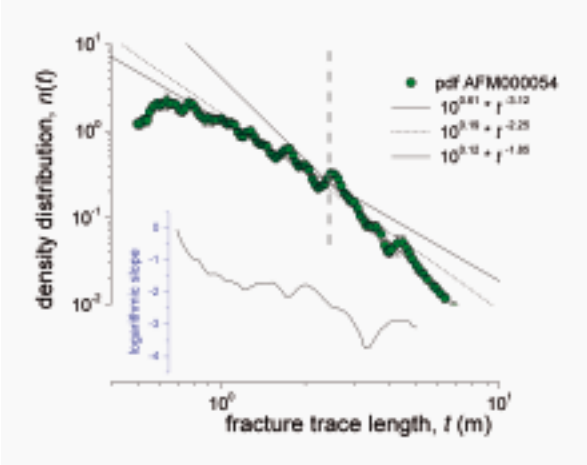

d)

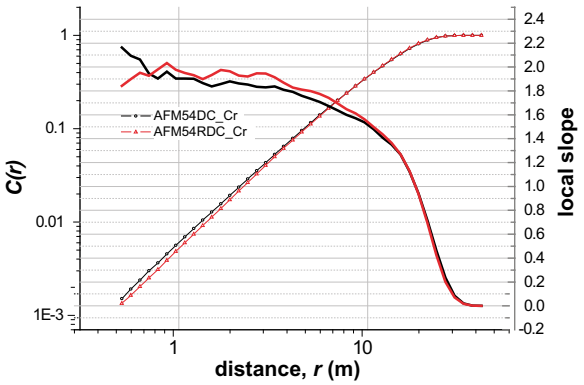

e)

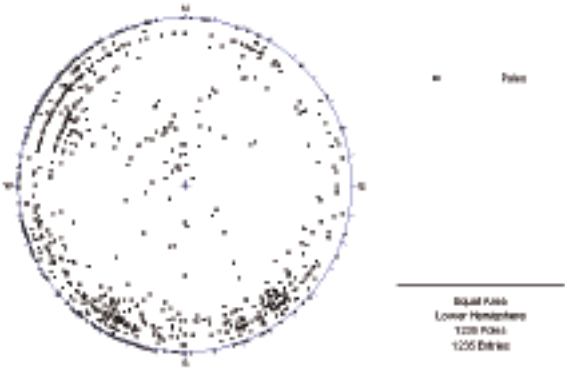

f)

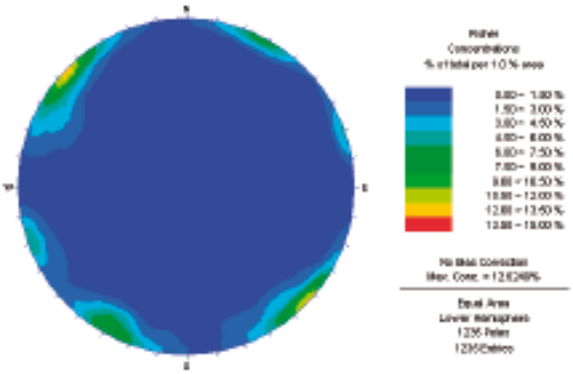

AFM001097

a)

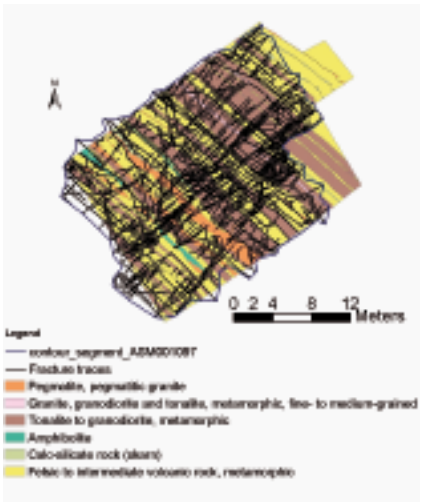

b)

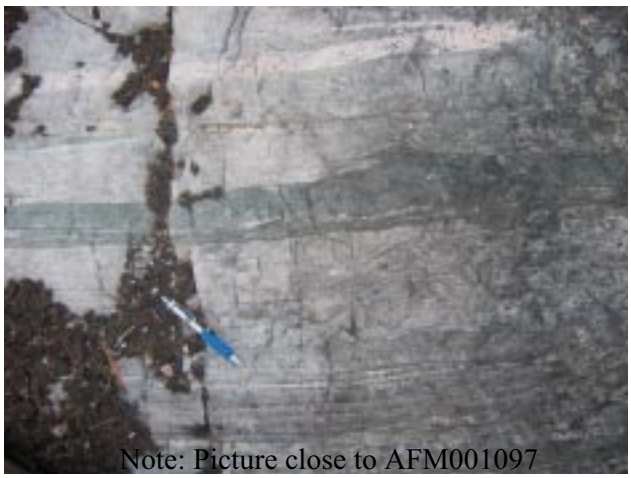

c)

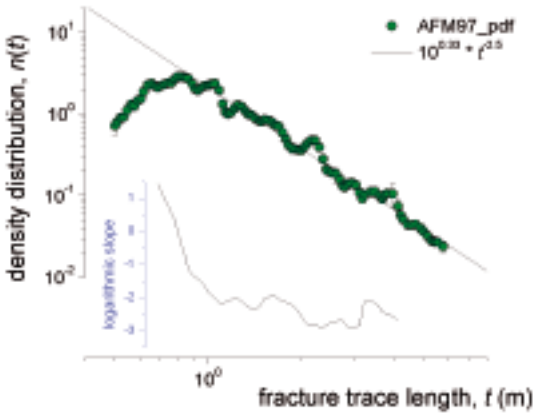

d)

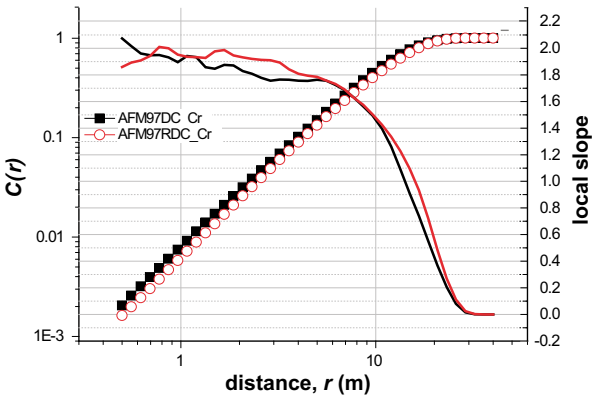

e)

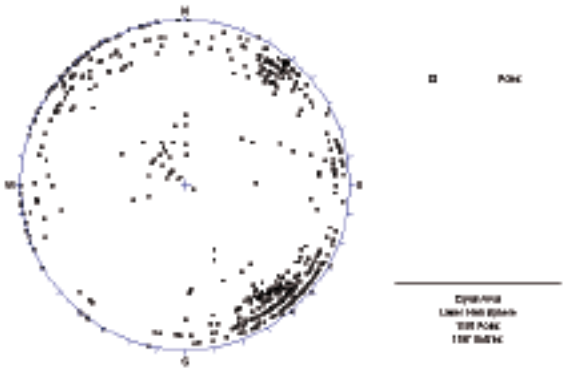

f)

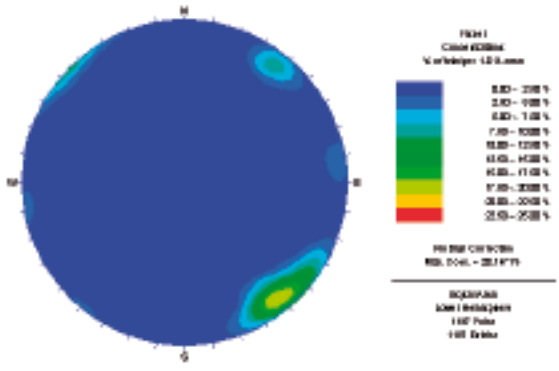

a)

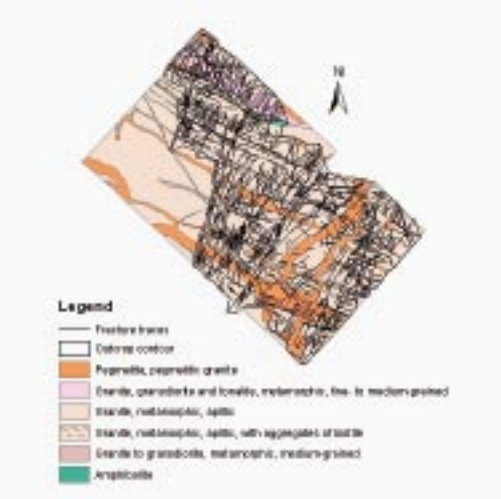
N
Legend

b)

c)

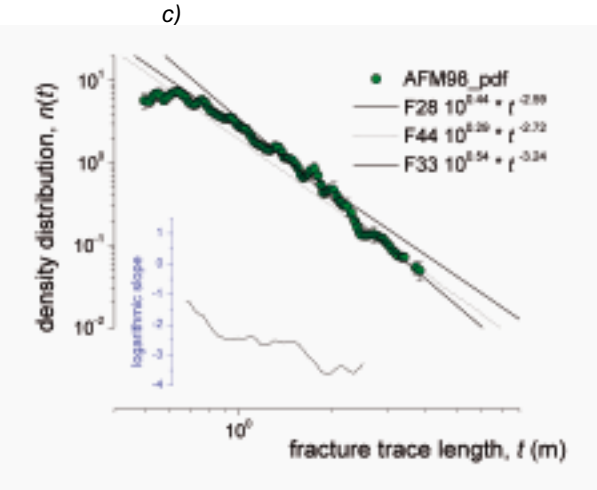
AFM98_pdf
F28 $10^{0.44} * t^{-2.89}$
F44 $10^{0.26} * t^{-2.72}$
F33 $10^{0.54} * t^{-3.24}$
density distribution, n(t)
logarithmic slope
10^0
fracture trace length, t (m)

d)

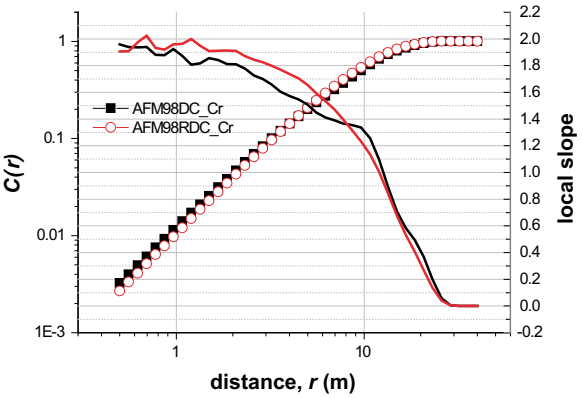
AFM98DC_Cr
AFM98RDC_Cr
C(r)
local slope
distance, r (m)

e)

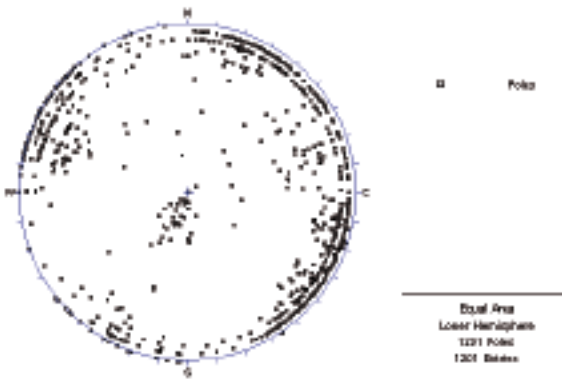

f)

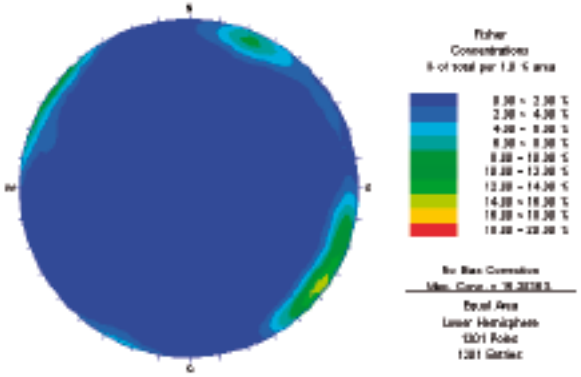

a)

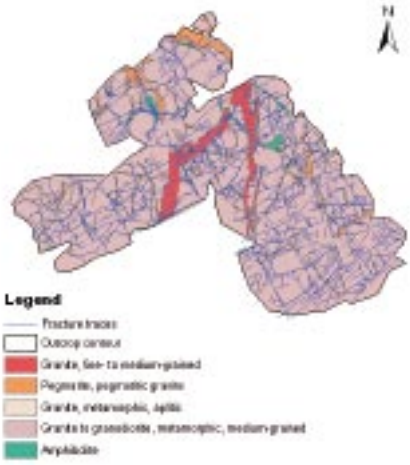
N
Legend
Fracture traces
Outcrop caveat
Granite, fine- to medium-grained
Pegmatite, pegmatitic granite
Granite, metamorphic, aplitic
Granite to granodiorite, metamorphic, medium-grained
Amphibolite

b)

c)

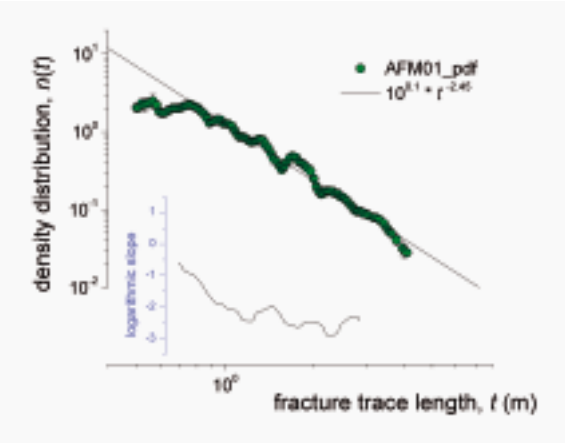
density distribution, n(f)
AFM01_pdf
$10^{3.1} * f^{-2.45}$
logarithmic slope
fracture trace length, f (m)

d)

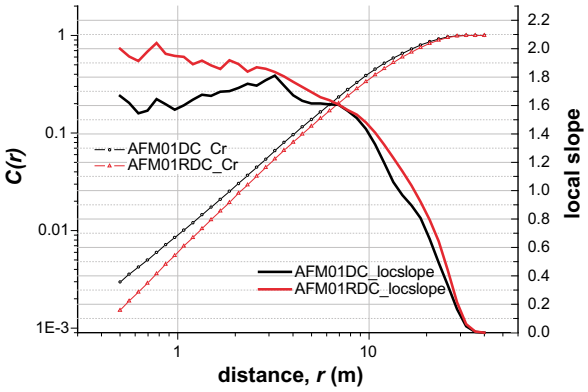
C(r)
AFM01DC_Cr
AFM01RDC_Cr
AFM01DC_locslope
AFM01RDC_locslope
local slope
distance, r (m)

e)

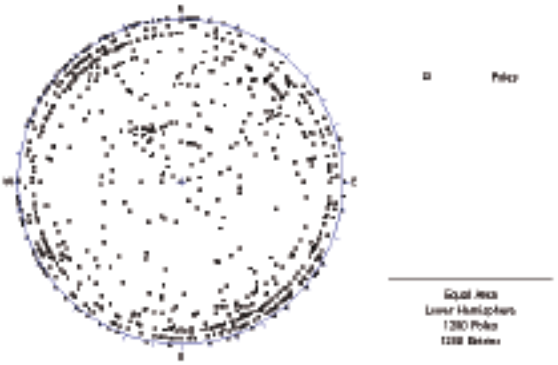

f)

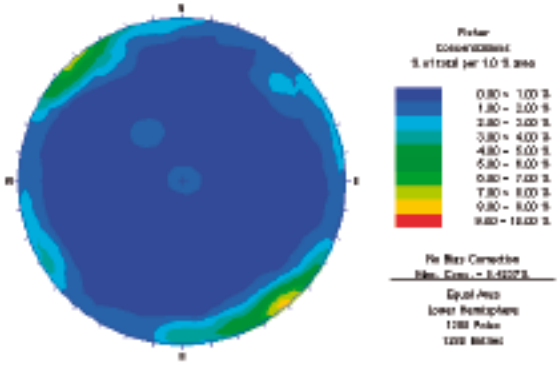

Note on the area estimate

Fracture areas (Table A1-1) are estimated from trace map contours, as illustrated in Figure A1-2. As illustrated on AFM001097, traces are mapped within a grid (violet in the figure). Next the map contour seems to have been drawn after the traces mapping, by encircling all the fracture traces. Grid areas and contoured areas can therefore differ from a few percents, leading to an uncertainty on the fracture trace map areas estimates. In these report, we have chosen to estimate the fracture trace map areas from the contoured areas.

Local “outcrop” models: orientation distribution

A table summarises the fracture set name (NW etc), orientation of the mean fracture plane (strike-dip), the Kappa value corresponding to an equivalent Fisher distribution and finally the modelled percentage of each set (corrected from orientation bias, ie directly the modelled percentage of fracture intensity belonging to the set for the bulk distribution).

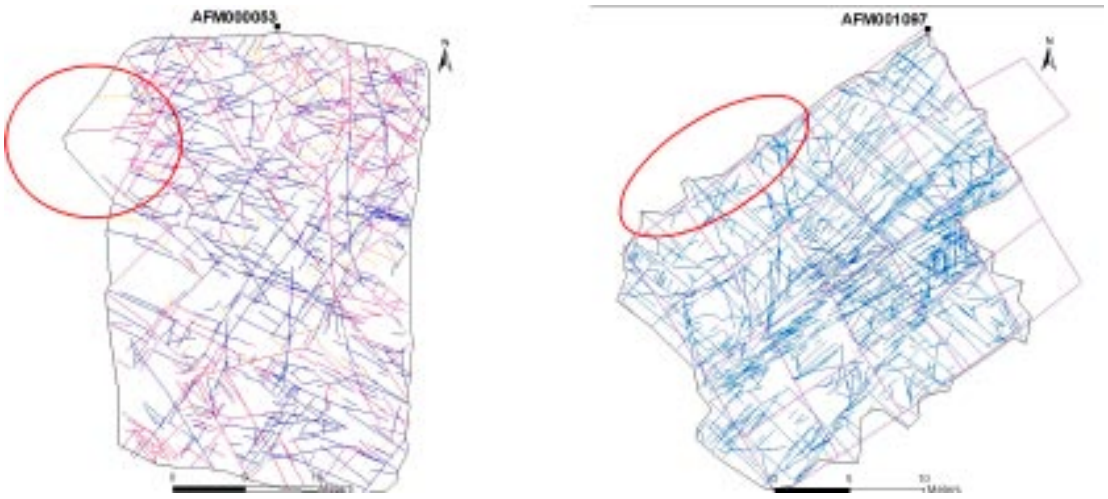

Figure A1-2. *Tracture traces (in color) and map (in black) contour for AFM000053 and AFM001097.*

Table A1-2. AFM000053, orientation distribution.

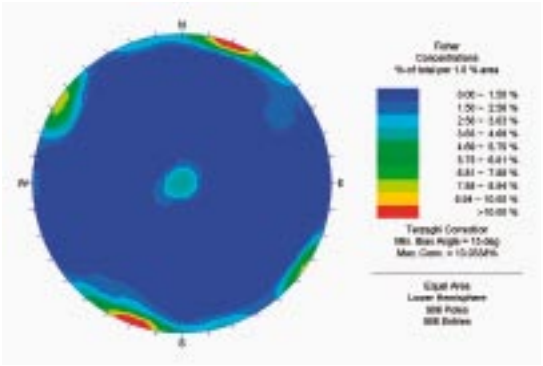

SET	mean strike	mean dip	K	Modelled Intensity (%)
SUBHZ	54	4	17	15
WNW	294	88	29	37
NNW	148	85	14	09
NS	179	89	28	04
NNE	33	88	38	23
ENE	256	88	35	12

Table A1-3. AFM000054, orientation distribution.

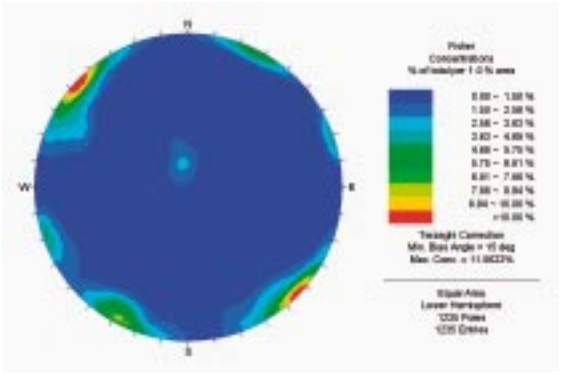

SET	mean strike	mean dip	K	Modelled Intensity (%)
SUBHZ	64	13	15	11
WNW	295	85	25	28
NNW	341	86	36	13
	43	88	17	48

Table A1-4. AFM001097 orientation distribution.

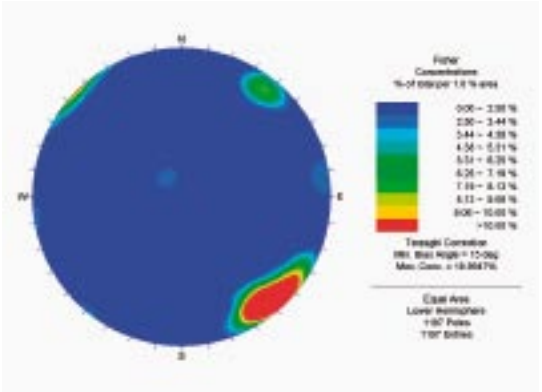

SET	mean strike	mean dip	K	Modelled Intensity (%)
SUBHZ	62	12	23	10
NW	125	81	34	18
NS	172	86	36	9
NE	229	81	27	63

Table A1-5. AFM001098, orientation distribution.

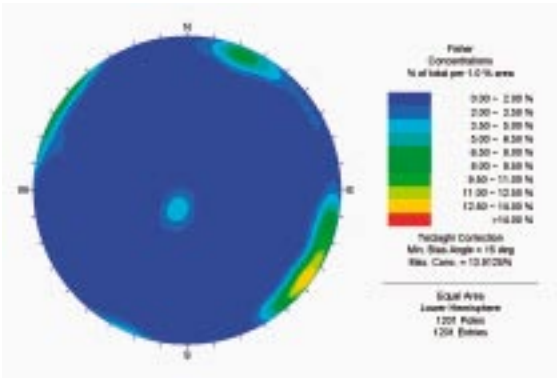

SET	mean strike	mean dip	K	Modelled Intensity (%)
SUBHZ	301	6	19	11
WNW	120	84	19	27
NNE	209	86	13	62

Table A1-6. AFM100201, orientation distribution.

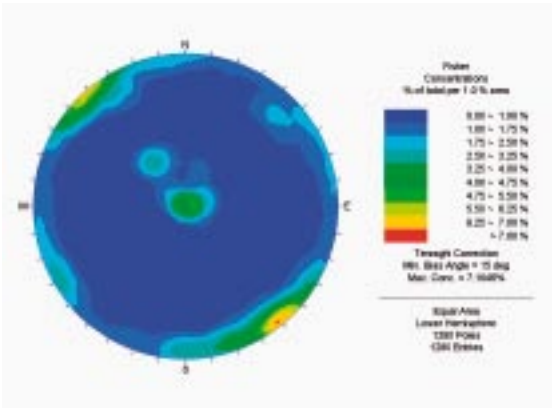

SET	mean strike	mean dip	K	Modelled Intensity (%)
SUBHZ	79	9	13	21
NNW	148	86	11	26
ENE	239	89	9	54

Appendix 2

Classical fracture distribution laws

Several kind of statistical laws are classically used to fit fracture size properties /Bonnet et al. 2001/. The most common are the power, lognormal, exponential and gamma laws. A general discussion of their relevancy for describing the frequency distribution of fracture properties can be found in /Bonnet et al. 2001/. We provide here a very short summary of Section 2 in /Bonnet et al. 2001/: a schematic plot (Figure A2-1) of these laws, illustrating in particular the absence of characteristic length scale associated only to the power law, and their mathematical expression.

The **lognormal law** is expressed by: $n(w) = \frac{A_1}{w \cdot \sigma \cdot \sqrt{2\pi}} \cdot \exp\left(-\frac{(\log(w) - <\log(w)>)^2}{2\sigma^2}\right)$

where w is the fracture length, $<log(w)>$ the logarithmic mean, σ the variance, and A_1 a constant.

The **exponential law** is expressed by: $n(w) = A_2 \cdot \exp\left(-\frac{w}{w_0}\right)$

where A_2 is a constant and w_0 a characteristic length scale.

The **power law** is expressed by: $n(w) = A_4 \cdot w^{-a}$, where A_4 is a constant and a the scaling exponent (with the correspondence in notation: $k=a-1$ from Equation 4-7 and Equation 4-8).

The gamma law is finally a power law with an exponential tail, expressed by:

$$n(w) = A_3 \cdot w^{-a} \cdot \exp\left(-\frac{w}{w_0}\right)$$

where A_3 is a constant, a the power law exponent and w_0 a characteristic scale.

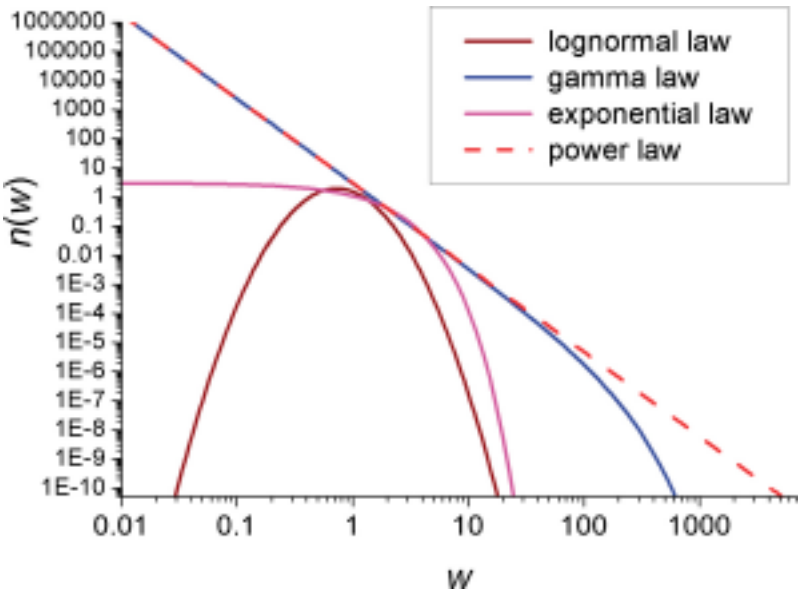

Figure A2-1. *Schematic plot illustrating the different functions classical used to fit fracture length distributions datasets.*

The power-law model shape is defined only by its scaling exponent (a), in contrast to other mentioned laws which use at least one parameter with a dimension of a length (w_0 <log(w)>). In that sense there is **no characteristic length scale in the power law** (see the schematic plot in Figure A2-1). Note finally that, in nature, power laws have to be limited by physical length scales that form the upper and lower limits to the scale range over which they are valid.

Appendix 3

Fractal objects and measures

Introduction

The **fractal dimension** associated to the DFN model defines the fracture density scaling. It is a mass dimension /Davy et al. 1990/. This dimension is equivalent to the so-called **correlation dimension** or **dimension of order two** of the **multifractal spectrum** /Bour et al. 2002/. It is measured from the spatial distribution of the discrete set of points formed by the fracture barycenters. The most appropriate method to measure the fractal dimension D (also noted $\boldsymbol{D}_c$) relies on the **integral of correlation** calculation /Bour et al. 2002/.

In practice, the **fractal dimension** D_{3d} associated to a 3d DFN model can not be measured directly. Therefore, values of D_c are inferred from measures of the fractal dimension performed over the 2d outcrops (noted D_{2d}) or along the boreholes (noted D_{1d}). In the present framework of DFN modelling, D_{3d} is linked to D_{2d} and D_{1d} /Darcel et al. 2003/. In order to better identify the **fractal dimension** considered here, we recall in the following basic definitions of fractal objects and multifractal measures.

Notations

To refer to the fractal dimension throughout the report, the notation D_c is kept to represent the correlation dimension (or equivalently the mass dimension) in general; "D_{1d}" and "D_{2d}" refer especially to measures performed on 1d and 2d supports respectively; at last, "D_{3d}" refers to the fractal dimension associated to the bulk DFN model.

Fractal object

According to Mandelbrot /Mandelbrot 1982/, a fractal object displays irregularities similar at all scales. From a general point of view, a fractal object is defined as an object having a non integer dimension and no characteristic length.

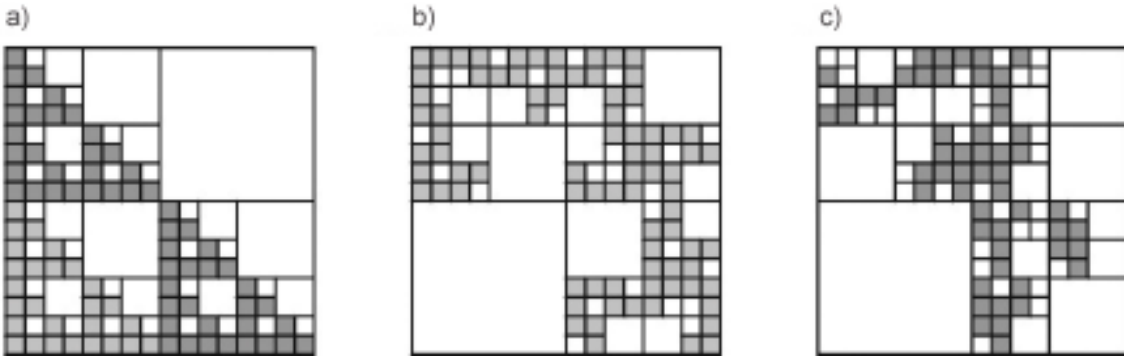

Figure A3-1. *a) deterministic fractal, Sierpinski carpet, b) statistical homogeneous fractal and c) statistical heterogeneous fractal.*

A simple way to measure the dimension consists in applying a classical paving method, by counting the number of elements necessary to cover an object as a function of the elements size. Let S be an object in $\Re^n$ and $N(\varepsilon)$ the number of hypercubes of radius ε necessary to cover S. The fractal dimension associated to S, $d_F(S)$, is defined from:

$$N(\varepsilon) \approx \varepsilon^{-d_F(S)}$$

Thus, the dimension of a straight line is 1 and the dimension of a plane is 2. In the case of the Sierpinski Carpet (Figure A3-1), at the scale $T/2^n$, if T is the linear size of the system, one needs $N_n(l_n)=3^n$ boxes of size $l_n=T/2^{-n}$ to cover the object, leading to a fractal dimension $D=\log(3)/\log(2)=1.58$. The Sierpinski carpet displayed in Figure A3-1a is deterministic: its shape is fully determined by an initiator (initial state) and a generator (recursive splitting operator). Fractals can also have a statistical nature. A statistical fractal is homogeneous if the mass ratio is conserved from a scale to the other (Figure A3-1b) and heterogeneous if this ratio can vary (Figure A3-1c). Most fractals observed in nature are statistical fractals /Korvin 1992, Viseck 1992/.

Contrary to the fractal dimension measurement over a regular (or deterministic) object, measuring the fractal dimension over an irregular (or statistical) object may lead to differents results according to the method used. Thus, several definitions of the fractal dimension are proposed in literature /Feder 1988, Gouyet 1992/. The method of the integral of correlation is found to be best suited for the charaterization of statistical fractals /Viseck 1992/. This method is based on the two-point statistic of the point set /Grassberger and Procaccia 1983/ and is defined as follows: let (x_j) be a set of points in the metric space X, one considers the counting function:

$$C(r,N) = \frac{1}{N^2} card\left\{(i,j); \left|x_i - x_j\right| \le r, i, j \le N\right\}$$

where card(A) refers to the number of pair of points whose distance is lower than r and N to the total number of points in the set. The limit

$$C(r) = \lim_{N \to \infty} C(r,N)$$

is the probability that two points of (x_j) are distant from a distance less than r. The **correlation dimension** is therefore given by:

$$D_c = \lim_{r \to 0} \frac{\log C(r)}{\log r}$$

Note that D_c is easily obtained from the slope of $C(r)$ vs r in log-log space.

Multifractals

The concept of a fractal is extended to the more complex notion of multifractal. A multifractal measure is linked to the characterization of the spatial distribution of a quantity associated to a support /Feder 1988/. One can for instance consider the density distribution of the human population over the world, or more simply over fracture density repartition within a fracture system. One defines the measure μ over its support S_μ . The multifractal formalism can be expressed through the concept of "partition function" /Feder 1988/. The partition function, for any $q \in \Re$, is written like:

$$Z(q,\varepsilon) = \sum_{i=1}^{N(\varepsilon)} \mu_i^q(\varepsilon)$$

where μ is the measure, ε the size. The partition function $Z(q, \varepsilon)$ represents the sum of the moments of order q of the measure distribution over the support. The spectrum $\tau(q)$ can be defined from the power-law behavior of $Z(q, \varepsilon)$ when $\varepsilon \to 0^+$:

$$Z(q,\varepsilon) \sim \varepsilon^{\tau(q)}$$

The spectrum of generalized dimensions, or *multifractal spectrum*, is defined as:

$$D_q = \frac{\tau(q)}{(q-1)}$$

The multifractal spectrum ($\{D_q\}$) characterizes the degree of homogeneity and regularity. The dimension D_0 (for q=0) is equal to the dimension of the physical support, which can be fractal itself, but not necessarily. If D_q=D_0 for any value of q, the measure is then uniform over the support, corresponding to the classical definition of a fractal (monofractal).

The **dimensions D_q** are linked to the **q-points correlation functions** (like the integral of correlation described above), /Grassberger and Procaccia 1983, Hentschel and Proccacia 1983/. In particular, the **correlation dimension** is equal to the dimension of order 2 (q=2) of the generalized dimensions spectrum.

Application to DFN

Independently of the multifractal or monofractal nature of a fracture system, the mass dimension (or correlation dimension, i.e. $D_{q=2}$ of the multifractal formalism) is sufficient to constrain the first order DFN model considered in the present work (Section 3).

The correlation integral method is adapted discrete fracture networks characterization /Bonnet et al. 2001, Bour et al. 2002/. We note that:

- In 2d, the points, from which the correlation function are calculated, are the fracture trace barycentre positions. However "all points of fracture plane are possible a priori candidates: we take the fracture barycenter as the most neutral position compared to fracture tips" /Bour et al. 2001/.
- For 1*d* datasets, fractures positions are non ambiguous, simply defined as the fracture intercepts.
- In the present case, measuring the fractal dimension through the classical mass dimension or integral of correlation method is almost equivalent. The difference concerns finite size effects due to finiteness of the datasets.
- In practice, the method efficiency is sensitive to the number of points in the dataset, and to the shape and size of the sampling area. To take account of possible boundary effects due to the shape of the support, an adapted method is proposed; the integral of correlation is calculated for two point sets: the original one ($C(r)$, or $C_{natural}(r) \sim r^{Dc}$) and a second one for which fracture positions have been homogeneously distributed over the support ($C_{homogeneous}(r) \sim r^d$). The ratio $C(r)_{homogeneous}/C_{natural}(r)$ varies as r^{d-Dc}, cleared from finite size effects related to the support shape.

Appendix 4

Stereological rules for random disk-shaped fractures

We aim at deriving the stereological rules for randomly distributed fractures with both fixed length and orientation distributions. This section is the extension of Piggot's work for randomly oriented fractures.

Consider a 3D distribution model for fractures, n_{3d} *(l,* θ, φ*, x, y, z)*, and the corresponding distribution of fracture traces in any plane: n_{2d} *(t,* θ, φ*, x, y)* The basic definitions are:

- θ is the fracture strike (similar in 3D and 2D if the intersection plane is horizontal).
- φ is the fracture dip.
- l is the fracture diameter.
- t is the length of the fracture trace.
- x, y, z are the coordinates of the fracture center.
- The intersection plane is defined by z=0, so that z is also the distance from the fracture center to the intersection plane.

If the fracture density is homogeneous, n_{3d} *(l,* θ, φ) is the number of fractures per unit volume whose orientations and diameter are in the intervals [l, l+dl], [θ, θ+dθ], and [φ, φ+dφ] respectively. n_{2D} is an areal density with similar definition.

The fracture trace length depends on l, φ and z, such as:

$$\sin\varphi = \frac{2z}{\sqrt{l^2 - t^2}}\text{, or conversely}$$

$$t = \sqrt{l^2 - \left(\frac{2z}{\sin\varphi}\right)^2} \qquad \text{(Equation 1)}$$

We make further equations simpler by applying the following variable change:

$$z' = \frac{2z}{\sin\varphi} \qquad \text{(Equation 2)}$$

The number of fracture trace with a length l and orientations (θ, φ) is the sum of all fractures above and below the intersection plane whose length follows:

$$n_{2d}(t,\theta,\varphi) = \int_{-\infty}^{+\infty} n_{3d}(l,\theta,\varphi)\frac{\mathrm{d}l}{\mathrm{d}t}\mathrm{d}z = 2\int_{0}^{+\infty} n_{3d}(l,\theta,\varphi)\frac{\mathrm{d}l}{\mathrm{d}t}\mathrm{d}z \qquad \text{(Equation 3)}$$

dz comes from the ratio between area and volume, which are basic to n_{2d} and n_{3d} respectively. The derivative $\frac{\mathrm{d}l}{\mathrm{d}t}$ makes the link between diameter and trace length. Its expression is derived directly from (1):

$$\frac{\mathrm{d}l}{\mathrm{d}t} = \frac{t}{\sqrt{t^2 + z'^2}}$$

By making the variable change (Equation 2), the stereological integral (Equation 3) now becomes:

$$n_{2d}(t,\theta,\varphi) = \sin\varphi \int_0^{+\infty} n_{3D}(l,\theta,\varphi,z) \frac{t}{\sqrt{t^2+z'^2}} dz' \qquad \text{(Equation 4)}$$

We now consider some basic assumptions for fracture distributions that are used when assessing a Discrete-Fracture-Network statistical model.

- The strike and dip orientations are assumed to be independent of the fracture-diameter distribution:

  $n_{3d}(l,\theta,\varphi) = \alpha_{3d}(\theta,\varphi)\, n(l)$

- The fracture-diameter distribution is assumed to be a power law:

  $n_{3d}(l,\theta,\varphi) = \alpha_{3D}(\theta,\varphi)\, l^{-a_{3d}}$

With these assumptions, (Equation 4) becomes:

$$n_{2d}(t,\theta,\varphi) = \alpha_{3d}(\theta,\varphi) \sin\varphi \int_0^{+\infty} \left(\sqrt{t^2+z'^2}\right)^{-a_{3d}} \frac{t}{\sqrt{t^2+z'^2}} dz'$$

$$n_{2d}(t,\theta,\varphi) = \alpha_{3d}(\theta,\varphi) \sin\varphi\, t \int_0^{+\infty} \left(\sqrt{t^2+z'^2}\right)^{-(a_{3d}+1)} dz'$$

By making the variable change, $u = 1 + \left(\frac{z'}{t}\right)^2$ the above equation can be written as:

$$n_{2d}(t,\theta,\varphi) = \alpha_{3d}(\theta,\varphi) \sin\varphi\, t^{-a_{3D}+1} \int_1^{+\infty} \frac{u^{-a_{3d}}}{\sqrt{u^2-1}} du$$

The integral term depends only on a_{3d}. By making an appropriate variable change with hyperbolic sine, we obtain:

$$\int_1^{+\infty} \frac{u^{-a_{3d}}}{\sqrt{u^2-1}} du = \frac{\sqrt{\pi}}{2} \frac{\Gamma(\frac{a_{3d}}{2})}{\Gamma(\frac{a_{3d}+1}{2})}$$

The final expression of n_{2d} is thus:

$$n_{2d}(t,\theta,\varphi) = \alpha_{3d}(\theta,\varphi) \sin\varphi \frac{\sqrt{\pi}}{2} \frac{\Gamma(\frac{a_{3d}}{2})}{\Gamma(\frac{a_{3d}+1}{2})} t^{-a_{3d}+1} \qquad \text{(Equation 5)}$$

For uniform dip and orientation distribution, $d(\varphi) = \frac{2}{\pi} d$ and the expression is similar to Piggott's equation:

$$n_{2d}(t) = \frac{d}{\sqrt{\pi}} \frac{\Gamma(\frac{a_{3d}}{2})}{\Gamma(\frac{a_{3d}+1}{2})} t^{-a_{3d}+1}$$

Now we make use of the 2D fitting model that have been defined for the fracture trace:

$$n_{2D}(t,\theta,\varphi) = \alpha_{2d}(\theta,\varphi)t^{-a_{2d}} \qquad \text{(Equation 6)}$$

The comparison of the previous equation with (5) implies that $a_{3d}=a_{2d}+1$, and that

$$\alpha_{2d}(\theta,\varphi) = \alpha_{3d}(\theta,\varphi)\sin\varphi\frac{\sqrt{\pi}}{2}\frac{\Gamma(\frac{a_{3d}}{2})}{\Gamma(\frac{a_{3d}+1}{2})}$$

α_{3d} can be obtained by integrating Equation 5 over the fracture trace length t:

$$\alpha_{3d}(\theta,\varphi) = \frac{2}{\sqrt{\pi}}\frac{\Gamma(\frac{a_{3d}+1}{2})}{\Gamma(\frac{a_{3d}}{2})}\frac{\int_t \frac{n_{2d}(t,\theta,\varphi)}{\sin\varphi}\,dt}{\int_t t^{-a_{3d}+1}dt}$$

The denominator integral can be obtained by integrating (Equation 6):

$$d_{2d} = \int_t n_{2D}(t,\theta,\varphi)\,dt = \alpha_{2d}(\theta,\varphi)\int_t t^{-a_{2d}}dt = \alpha_{2d}(\theta,\varphi)\int_t t^{-a_{3d}+1}dt$$

with d_{2d} the average fracture density mapped on the outcrop. Then $\alpha_{3d}(\theta, \varphi)$ writes:

$$\alpha_{3d}(\theta,\varphi) = \frac{\alpha_{2d}(\theta,\varphi)}{d_{2d}}\frac{2}{\sqrt{\pi}}\frac{\Gamma(\frac{a_{3d}+1}{2})}{\Gamma(\frac{a_{3d}}{2})}\int_t \frac{n_{2d}(t,\theta,\varphi)}{\sin\varphi}dt$$

The derivation of $\alpha_{3d}(\theta, \varphi)$ for any values of θ and φ is now straightforward since the integral consists in counting the fracture population with the specified conditions in θ and φ.

Appendix 5

Methodology – local deviations

Borehole curvature

If the borehole curvature is not negligible, then the correction from orientation bias must be based on the local borehole direction instead of the mean borehole direction. The effect of the borehole curvature is complex: it relies obviously on the local borehole orientation and on the intersected fracture orientation. For a given class of orientations it can affect the apparent fracture intensity. The only case where fracture intensity is independent of the borehole direction is for a homogeneous orientation distribution. To delimit the problem, we have calculated the local deviation from the mean direction along all the boreholes; then a local borehole direction has been associated to each fracture intersection position and the subsequent correction from orientation bias have been systematically based on the local borehole direction.

Local deviation – definition and calculation

To calculate the borehole local deviation from its mean direction, we have chosen the following procedure (see Figure A5-1). The mean direction is calculated from the extreme fracture intersection points. Locally the direction is calculated from the fracture intersection positions with a given sampling step. The local deviation is defined as the angle between local and mean borehole orientation.

Application to the data

The size of the sampling step is varied to check the procedure. If it is too large, some local high variations (Figure A5-2 left) are missed. On the contrary, if it is too short, no fracture intersections positions are available to calculate the deviation. We finally choose a step of size 4 m to calculate locally the borehole direction. Local deviations from mean direction are illustrated on the below.

All boreholes display departure from a constant direction (Figure A5-2). Variations are most of the time smooth, except for KFM04A (Figure A5-2) around depth –340 m. the variations for instance for borehole KFM04A, are comprised between 43° and 63° for the trend and 30° and 45° for the plunge.

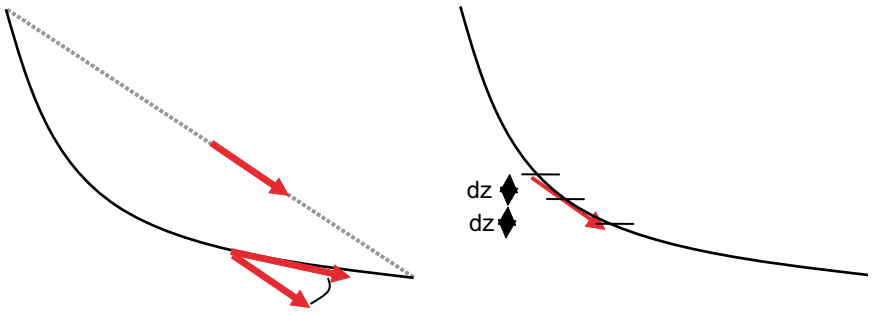

Figure A5-1. *Scheme of the local borehole deviation calculation*

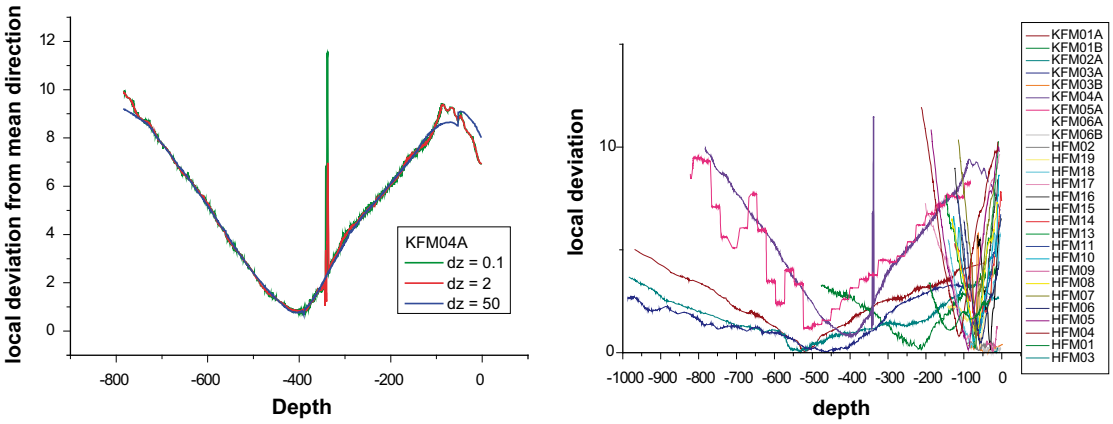

Figure A5-2. *Local deviation (left) example of KFM04A for dz equal to 0.1, 2 and 50 (right) all the boreholes (dz=± 2 m).*

Conclusion

- all boreholes must be analysed with great care: it is not possible to run automatic procedures, all the support samples are distinct,
- the local borehole direction must be taken to correct observations from orientation bias,
- numerical simulations of validation must include the special shape of borehole (finite size and local deviations).